Strong-field Dissociative Ionization as a Probe of Molecular Dynamics and Structure

A Dissertation Presented

by

Marija Kotur

to

The Graduate School

in Partial Fulfillment of the Requirements

for the Degree of

Doctor of Philosophy

in

Physics

Stony Brook University

May 2012

Stony Brook University

The Graduate School

Marija Kotur

We, the dissertation committee for the above candidate for the Doctor of Philosophy degree, hereby recommend acceptance of this dissertation.

Thomas C. Weinacht - Dissertation Advisor
Associate Professor, Department of Physics and Astronomy

Philip Allen - Committee Chair
Professor, Department of Physics and Astronomy

Xu Du
Assistant Professor, Department of Physics and Astronomy

Andreas Becker
Associate Professor, Department of Physics, University od Colorado and
Associate Fellow, JILA

This dissertation is accepted by the Graduate School

Charles Taber
Interim Dean of the Graduate School

Abstract of the Dissertation

Strong-field Dissociative Ionization as a Probe of Molecular Dynamics and Structure

by

Marija Kotur

Doctor of Philosophy

in

Physics

Stony Brook University

2012

We present work on strong-field ionization of polyatomic molecules. Strong-field ionization has been in focus of recent research efforts in ultrafast atomic, molecular and optical science, due to its role in the generation of attosecond pulses and as a probe of both nuclear and electronic dynamics, and in imaging of molecular orbitals.

Ultrafast relaxation of excited state DNA and RNA bases, instrumental to their photostability, was tracked using strong-field dissociative ionization. Relaxation through multiple pathways has been observed and interpreted in terms of the excited state wavepacket dynamics. The example of cytosine is presented in detail.

The electronic dynamics associated with the strong-field ionization process were explored, in particular the role of the symmetry of the neutral orbital from which the electron was removed. For ionization from the highest lying occupied orbital, the ionization yields are shown to reflect the symmetry of the orbital. Ionization from a deeper bound orbital is found to be more complicated. Further, we find that a detailed treatment of ion-electron interactions that take place during the ionization process is necessary to achieve a qualitative agreement between final-state-resolved calculations and experiments.

Contents

List of Figures

List of Tables

Acknowledgements

I feel very privileged that I have many people to thank, even if that makes this section read very much like a laundry list. First, I would like to thank my advisor Tom Weinacht for his support, advice, patience, numerous discussions and late nights in the lab, and above all for his unfaltering enthusiasm. I very much enjoyed every aspect of being a part of the ultrafast spectroscopy lab, from the time-consuming laser repairs to the productive discussions we had at group meetings and otherwise.

Many thanks to the current and former members of the group. To Brett Pearson, for showing me the ropes in the lab, to Carlos Trallero, for the encouragement and for introducing me to *ab initio* calculations, to Sarah Nichols, for her detailed answers to all the questions I ever asked her, to Chien-hung (Coco) Tseng, for memorable moments in the lab, to Oumarou Njoya for the time we spent in the lab together, and to Stephen Clow, Uvo Hölscher and Péter Sándor and for the camaraderie. Thanks to Martin Cohen for the helpful advice, especially with all kinds of laser issues. Special thanks to my officemate Dominik Geißler, for the help in the lab and with various codes, the endless discussions, for sharing his "crazy" ideas with me, for the coffee breaks, driving lessons, trips, and other things too numerous to list here, but above all for bearing with me all these years.

I have greatly benefited from strong collaborations with theorists. The results presented in this thesis would not be possible without prof. Spiridoula Matsika from Temple University and Michael Spanner from the National Research Council of Canada.

I very much appreciated the friendly atmosphere at the Department of Physics and Astronomy. It was great to be a part of the AMO group here, and I thank prof. Schneble, prof. Bergeman and prof. Metcalf and their students for making it such an enjoyable place to work at.

My thanks go to Sara Lutterbie and Pat Peiliker for their help with administrative matters. The lab and my exprimetns would have ran as smoothly as they did without the excellent support of the machine and electronics shop, and the advanced technology lab personnel. I am indebted to Walter Schemeling, Jeff Slechta, Mark Jablonsky, Jeff Thomas, Paul DiMatteo, Gene Shafto, Chuck Pancake, and Pete Davies for the designs and the advice. Thanks to Andrzej Lipski for his help with sample stability tests.

Thanks to the committee members, prof. Phil Allen, prof. Xu Du and prof. Adreas Becker for their detailed and helpful comments and corrections to this thesis.

Grad school years wouldn't be as enjoyable if not for the all great people I met here. Thanks to Francis Paraan, Cameron Crowe, Manas Kulkarni, Divya Bhatnagar, Sriram Ganeshan, Chee Sheng Fong, Heli Vora, Pedro Liendo, Constantinos Constantinou, Nathan Borggren, and many others.

Many thanks to my friends from Serbia, Ana Banković, Jelena Grujić, Višnja Jankov, Nataša Lazić, Ivan Jokić, Luka Nenadović, Branimir Acković, Branislav Cvetković, Jovan Vasiljević, Milovan Šuvakov, Rajna Dimitrijević, Ksenija Perišić and Milena Mitić, and to my cousin Dušan Pantelić for all the fun times on Skype, during my visits to Belgrade and where ever else we met.

Finally, thanks to my parents and to my brother Nikola, for their continuing support.

List of Publications

This thesis is based on the following publications:

1. Marija Kotur, Congyi Zhou, Spiridoula Matsika, Serguei Patchkovskii, Michael Spanner, and Thomas C. Weinacht, "Role of electronic state correlation in strong field molecular ionization", (*submitted*).

2. Marija Kotur, Thomas Weinacht, Brett Pearson and Spiridoula Matsika, "Closed-Loop Learning Control of Isomerization using Shaped Ultrafast Laser Pulses in the Deep Ultraviolet," *Journal of Physical Chemistry* **130**, 134311 (2009).

3. Marija Kotur, Thomas Weinacht, Congyi Zhou and Spiridoula Matsika, "Following Ultrafast Radiationless Relaxation Dynamics with Strong Field Dissociative Ionization: A Comparison between Adenine, Uracil and Cytosine," *Journal of Special Topics in Quantum Electronics* **99**, 1 (2011).

4. Marija Kotur, Thomas Weinacht, Congyi Zhou and Spiridoula Matsika, "Distinguishing Between Relaxation Pathways by Combining Dissociative Ionization Pump Probe Spectroscopy and *ab initio* Calculations: A Case Study of Cytosine", *Journal of Physical Chemistry* **134**, 184309 (2011).

5. Marija Kotur, Thomas Weinacht, Congyi Zhou and Spiridoula Matsika, "Strong Field Molecular Ionization from Multiple Orbitals", *Physical Review X*, **1**, 021010 (2011).

Additional work completed during the author's PhD career:

1. Pascal Krause, Marija Kotur, and Thomas C. Weinacht, and Spiridoula Matsika, "Photo-induced fragmentation and excited state topology", (*in preparation*).

2. Michael Spanner, Serguei Patchkovskii, Congyi Zhou, Spiridoula Matsika, Marija Kotur, and Thomas C. Weinacht., "Role of electronic state correlation in strong field molecular ionization", (*in preparation*).

3. Congyi Zhou, Spiridoula Matsika, Marija Kotur and Thomas Weinacht, "Fragmentation Pathways for Uracil Radical Cations", (*submitted*).

4. Spiridoula Matsika, Congyi Zhou, Marija Kotur and Thomas Weinacht, "Combining dissociative ionization pump–probe spectroscopy and *ab initio* calculations to interpret dynamics and control through conical intersections", *Faraday Discussions* **153** (1), 247 - 260 (2011).

5. Chien-hung Tseng, Péter Sándor, Marija Kotur, Thomas C. Weinacht, and Spiridoula Matsika, Two Dimensional Fourier-Transform Spectroscopy of Adenine and Uracil Using Shaped Ultrafast Laser Pulses in the Deep UV, *The Journal of Physical Chemistry A*, **116**, 2654 (2012).

Chapter 1

Introduction

The invention of the laser in 1960 [1], followed several years later by the first pulsed laser, opened up numerous new avenues for research in physics and chemistry. Solid-state gain mediums, the most widely used of which is titanium sapphire (Ti:sapphire), enabled the production of pulses with a duration in the femtosecond range [2]. Chirped pulse amplification (CPA) [3] was a major advance that allowed the increase of maximum intensity of produced pulses. Pulses shorter than about 100 fs, that are routinely produced in the infrared range of wavelengths using CPA, reach a peak intensity that is comparable to the atomic unit of electric field ($5.14\cdot 10^{11}$V/m), sufficient to ionize electrons from atoms and molecules [4]. In addition to the peak intensities they provide, ultrafast lasers enable time-resolved measurements to be performed on molecular systems, where a pump laser initiates dynamics that can subsequently be probed by another ultrafast laser pulse. This combination of field strength and time-resolution makes ultrafast lasers an essential and unique tool for studying the dynamics and structure of atoms and molecules, since they can both initiate and probe nuclear and electronic dynamics.

Laser pulses with a duration of several tens of femtoseconds are suitable for time-resolved measurements of nuclear dynamics of molecules that occur on timescales of several hundred femtoseconds or slower. The motion of electrons is faster, occurring at 100 attosecond timescales. The short (attosecond) pulses needed to access these faster timescales, are at present produced only through the process of high harmonic generation (HHG). This process was used to study attosecond electron and nuclear dynamics [5–8]. In HHG, an electron

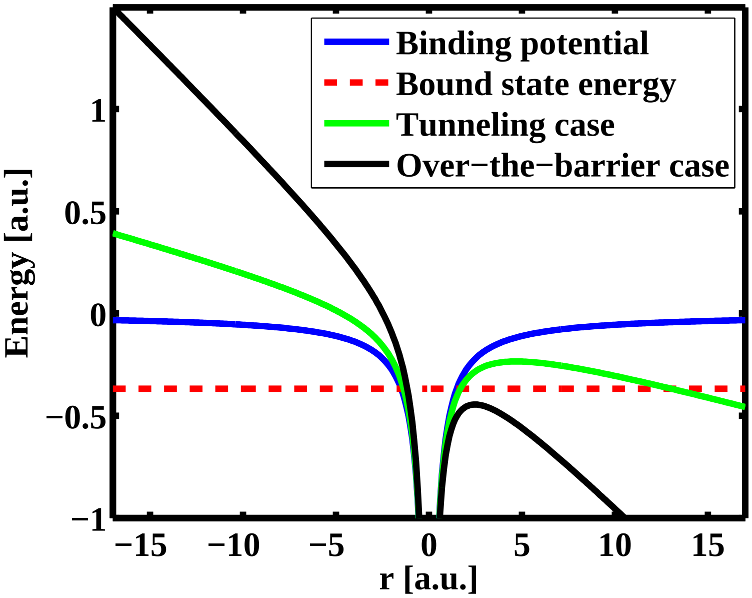

Figure 1.1: Binding potential of an atom (blue solid line), valence electron energy based on a 10 eV ionization potential (red, dashed line), laser-dressed binding potential in the tunnel ionization case (green solid line), laser-dressed binding potential in the over-the-barrier case (black solid line).

ionized into the continuum from an atom or a molecule by a strong laser field recollides with the ion, releasing an energetic photon as the electron deexcites into one of the bound states. In the case of molecules, HHG is sensitive to the details of the molecular structure and the interactions between its electrons [8–11].

The interaction between an atom or a molecule and a weak electromagnetic field can be described perturbatively, where the unperturbed Hamiltonian is the atomic or molecular Hamiltonian, while the field is treated as a small perturbation. However, when the electromagnetic field is very strong, it is not possible to treat it as a small perturbation.

The two regimes in which laser-driven strong-field ionization (SFI) can occur that are relevant for the work presented in this thesis, are the quasi-static tunneling regime and the multiphoton regime. Figure 1.1 illustrates these regimes for the Coulombic binding potential of an atom. The binding potential of a molecule is more complicated, with structure reflecting the multiple nuclei present.

If the frequency of the laser field is sufficiently small, ionization of atoms and molecules can be viewed as tunneling through a barrier arising from the shape of the laser-dressed binding potential. In the multiphoton regime, the ionization occurs through the absorption of multiple photons needed for the bound electron to gain enough energy to reach one of the continuum states. The two ionization regimes are commonly characterized by the Keldysh adiabaticity parameter [12]:

$$\gamma = \sqrt{\frac{I_P}{2U_P}},\ U_P = \frac{|E_0|^2}{4\omega_{laser}^2} \tag{1.1}$$

Here I_P is the ionization potential, U_P is the ponderomotive energy, or the average energy of electron oscillations in the laser field, ω_{laser} is the laser frequency, and $|E_0|$ the electric field amplitude. Quasi-static tunneling corresponds to $\gamma \ll 1$, while multiphoton ionization corresponds to $\gamma \gg 1$. It is useful to define the concept of tunneling time, which is the time it would take the electron to cross the barrier moving in a uniform electric field, if the process were classically allowed. For this process (setting electron mass, m_e=1, and electron charge, e=1), the velocity of the electron as a function of time is given by $v(t) = v_{max} - |E_0|t$. Here $v_{max} = \sqrt{2I_P}$, and for tunneling resulting in an electron produced in the continuum with zero energy, $v_{final} = 0$. This yields a tunneling time of $\tau_{tunnel} = v_{max}/|E_0| = \sqrt{2I_P}/|E_0|$. Expressing the Keldysh parameter in terms of the laser frequency ω_{laser}, and the tunneling frequency, defined as $\omega_{tunnel} = 1/\tau_{tunnel}$ leads to the expression:

$$\gamma = \frac{\omega_{laser}}{\omega_{tunnel}}. \tag{1.2}$$

The quasi-static tunneling regime is characterized by $\omega_{laser}/\omega_{tunnel} \ll 1$. So the shape of the barrier does not change significantly during the tunneling process [13], giving rise to the name used for this regime. It is an interplay of laser frequency, ionization potential and and field strength that leads to quasi-static tunneling being the dominant effect in an ionization process. The field strength has to be high enough to tilt the potential sufficiently to give rise to a finite barrier, while the frequency has to be low enough that the condition from equation 1.2 is satisfied for tunneling to take place on a sub-cycle timescale. It should be noted that a tunneling component is present in the multiphoton regime as well. This tunneling differs from the quasi-static one, in that the barrier shape changes during the tunneling process.

The multiphoton nature of ionization by intense, high-frequency laser fields is particularly clear in the photoelectron spectra taken at intensities high enough that more photons than required for ionization are absorbed. The photoelectron spectra show a periodic structure, where the spacing between features corresponds to the photon energy. This is known as the above threshold ionization [14] (not shown in figure 1.1).

At very high intensities, the electric field of the laser can tilt the Coulomb potential and suppress the barrier to ionization, making the electron escape classically allowed. The observed intensities of appearance of several charge species of noble gases agree well with the prediction of the simple, semi-classical model [15].

In experiments that are presented in this thesis, γ ranged from 1-3 for ionization of ground state molecules and from 0.5-2 for ionization of excited state molecules. In the case where $\gamma \approx 1$, the ionization was a mixture of tunnel- and multiphoton ionization, commonly referred to as strong-field ionization. In ionization by multicycle ultrafast laser fields the target interacts with several half-cycles, many of which have an intensity significantly lower than the peak intensity of the pulse. Furthermore, given the non-uniform, usually Gaussian spatial profile of a laser beam, the central and the outer portions of any beam correspond to very different intensities. This effect is known as the focal volume spatial intensity averaging, and often presents a challenge in comparing experimental results to theoretical predictions. The multi-cycle character of our laser pulses, and the focal volume spatial intensity averaging lead to both the multiphoton and the tunneling contributing to the ion yield measured in a strong-field ionization experiment.

Theoretical efforts in understanding the tunneling process started with the invention of quantum mechanics. A common feature of these theories is that the ionization rates depend strongly (exponentially) on the binding potential. Tunneling theory was first derived by Fowler and Nordheim [16] in 1928, for the case of electron emission from metals. Oppenheimer [17, 18] applied it to ionization of hydrogen-like atoms in strong external fields. It was later rederived by Keldysh [12] and by Perelomov, Popov and Terentev (PPT, 1967) [19], for DC tunneling from hydrogen-like atoms in a field of a strong oscillating electromagnetic field. A treatment of non-hydrogen, polyelectron atoms was presented by Ammosov, Delone and Krainov in 1986 [20], and became known as the ADK tunneling theory. A further level of sophistication was added by Faisal and Reiss [12, 21–24], in what is known as the Keldysh-Faisal-Reiss (KFR) theory. It includes several atomic centers and shows how interferences between them can lead to a suppression of ionization rates from some molecules (compared to atoms with a similar ionization potential), depending on the shape of their valence orbital. Another simple, structure-based model that addressed tunneling in multi-center potential, was the 'bucket' model offered by Levis [25]. This model was successfully used to explain the increase in ionization rate with the size of a molecule between several polyatomic molecules with similar ionization potentials. The KFR picture was further improved on by the molecular ADK theory [26], which includes the structure of the molecular wavefunction in the tunneling region.

The dependence of strong-field molecular ionization on the properties of a molecule opens up possibilities for using SFI to monitor the molecular dynamics. One example is the relaxation of excited-state molecules, which plays an important role in photochemical processes that occur in many biologically-relevant systems. Many of the relaxation processes are non-radiative and proceed through crossings between molecular potentials that occur at points of energetic degeneracy. When the potential energy surfaces are evaluated as a function of two coordinates, the surfaces in the vicinity of the crossing take on the shape of a double cone, giving rise to the name conical intersection (CI) [27]. These intersections provide a route for rapid non-radiative relaxation of excited molecules, but also points where the excited state wavepacket can bifurcate, retrieving ground state with a significantly different geometry than the starting one.

Conical intersections are known to play an important role in the relaxation dynamics of many molecules, most notably in isolated nucleic bases, the chromophores of DNA and RNA [28]. The nucleic bases are known to exhibit a rapid relaxation through conical intersections, leading to their photostability. Theoretical studies have shown the bases to have more than one accessible conical intersection that can lead to competing relaxation pathways. Dynamical studies have indicated that multiple conical intersections may play a role in relaxation, leading to a delocalization of the excited state wavepacket [29]. However, theory alone cannot determine whether one or more of these pathways are explored, or predict the relative importance of the pathways.

Ionization potential influences the strong-field molecular ionization to a great extent, but as is evident from comparisons between the ionization rates of atoms and molecules with similar ionization potentials, factors such as orbital structure play a role as well. Molecular ionization can involve removal of an electron from orbitals below the highest lying one [30], but it is not always clear which orbital was ionized, or if there are differences between ionization from a high lying and a low lying orbital.

The distribution of final states in which the molecule is left following strong-field ionization is currently an open problem in the field. Since excited states of the ion often have a hole in an orbital below the highest occupied one, the removal of lower-lying electrons may be a dominant pathway to reaching an excited ionic state. In addition, the role of multi-electron effects in determining the final state of an ionization process is currently not fully understood.

In this thesis, we use strong-field ionization to follow the excited state dynamics, but we explore some of the properties of the ionization process itself as well. The thesis is composed of seven chapters.

Chapter 2 introduces the experimental apparatus that was used. It starts with a brief overview of the laser system. It then continues to describe the pulse shaper and the beamlines used in the UV-pump, IR-probe experiments. Finally, it gives the details of the vacuum chamber, including the time-of-flight mass spectrometer and the oven with a heated nozzle used to sublimate powdered samples.

In chapter 3, we study the photochemical ring opening reaction of cyclohexadiene to form 1,4,5-hexatriene. The ring opening occurs during the relaxation of excited state cyclohexadiene, and involves a conical intersection between the ground and an excited state. The two isomers, despite having comparable ionization potentials of 8.25 and 8.32 eV, exhibit very different strong-field ionization rates and dissociation propensities. We use this fact to try and control the outcome of the relaxation through the CI. In our control scheme, excitation by an ultrafast UV pulse initiates the photochemical reaction, and a strong-field IR pulse ionizes the molecule after a variable delay. A learning algorithm is used to find a pulse shape that optimally achieves a goal formulated in terms of fragment ion yields. This chapter is based on ref. [31].

In chapter 4 we present the results of nucleic base excited state dynamics studies, which were originally published in references [32] and [33]. Employing a weak, near-resonant pump and a delayed, strong-field probe we were able to follow the excited state relaxation of the isolated nucleic bases adenine, cytosine, and uracil. The details of the relaxation pathways differ between the three bases. A common feature of the relaxation dynamics of these molecules is that it is non-local. The excited state wavepacket breaks up into many parts, and explores multiple relaxation pathways in parallel. We discuss several of the factors that contribute to the differences in dissociation patterns along separate relaxation pathways with an emphasis on the shapes of the molecular orbitals, and the electronic configurations. We present the case of cytosine in detail.

Chapter 5 is based on ref. [34]. In contrast to the previous two chapters, in this chapter we study some of the intrinsic properties of strong-field ionization, rather than using it only as a part of the detection scheme. Here, we first identify ionic fragments that are formed following the removal of an electron from a specific orbital of the molecule. Then, we examine how the angle-resolved distribution of ionization yields depends on the orbital from which an electron was removed. We find that the angular distribution for the electron removed from the lowest unoccupied molecular orbital follows the symmetry of this orbital, while ionization of the molecule by removing electrons from deeper bound orbitals is more complicated.

In chapter 6 we examine three theoretical methods of calculating final-state resolved strong-field ionization yields and compare them with our experimental results. The first method is based upon Dyson orbital amplitudes, which in the case of strong-field ionization need to be scaled by a tunneling exponent that is exponentially sensitive to the ionization potential of a given ionization channel. This method is closely related to the predictions of some of the formulations of the strong-field approximation. The second method is the molecular Ammosov-Delone-Krainov method, which uses asymptotic properties of wavefunctions to estimate ionization yields. Finally, the third method is the time-dependent resolution in ionic states method (TD-RIS), that was developed by our collaborators at the National Research Council of Canada. It solves the time-dependent Schrödinger equation numerically, taking into account the ion-electron interaction in some more detail. Comparison to our experimental results shows a better agreement with the latter method, highlighting the importance of electron-ion interactions. The results of this chapter are based on reference [35].

The notation for molecular states used in this thesis is S_0, S_1,... for the neutral singlet states and D_0, D_1,... for the doublet states of the ion. Here S_0 and D_0 are the ground states of the neutral and the ion, S_1 and D_1 are their first excited states, and so on.

Chapter 2

Experimental apparatus

In this chapter, we describe the apparatus used in experiments detailed in subsequent chapters. All the experiments presented here were performed using the same laser system, beamlines, time-of-flight mass spectrometer and acquisition hardware. However, different vacuum manifolds were used for liquid and solid phase samples. Experiments on liquid phase samples were conducted using a sample manifold based on designs from [36]. The experiments on solid (powdered) samples were done using a heated sample manifold and a heated nozzle described in subsection 2.6. The experiments described in the following chapters utilized a pump-probe scheme to study molecular dynamics. Ultraviolet (UV) laser pulses at the central wavelength of about 262 nm were used to pump the molecules. The dynamics was probed by illuminating the molecule with intense, infrared (IR) laser pulses that ionized and fragmented the molecules.

2.1 Laser system

We start from a KM Labs Kerr-lens modelocked Ti:sapphire femtosecond oscillator, pumped by a continuous wave, 4.3 W Coherent Verdi V5 laser. The pulses produced are used to seed a KM Labs HAP multipass amplifier [37], which utilizes Ti:sapphire as a gain medium, and is pumped by an 11 W Quantronix Nd:YAG nanosecond laser. The amplifier outputs 30 fs pulses at a central wavelength of 780 nm, with an energy of 1 mJ per pulse and a repetition rate of 1 kHz. The pulses are characterized by a second harmonic

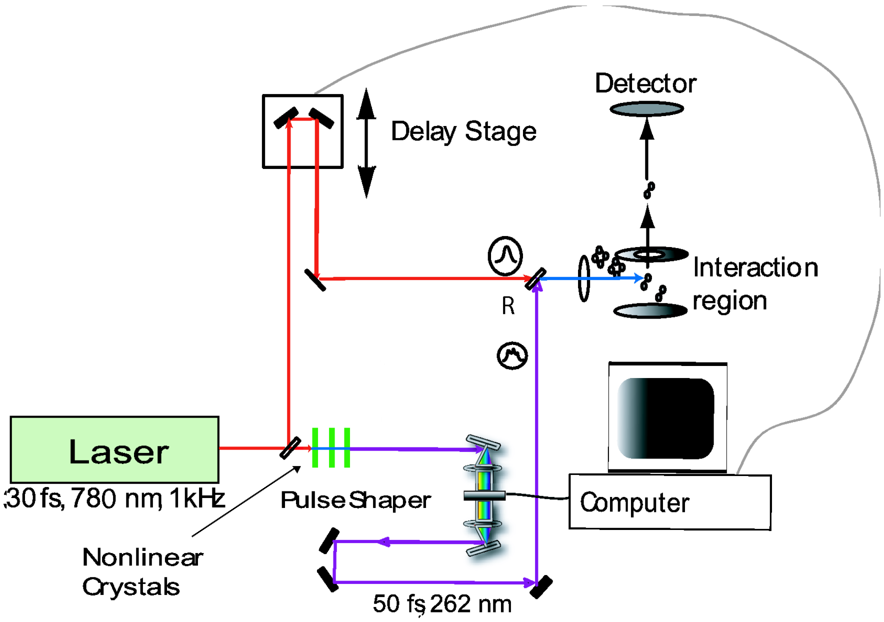

Figure 2.1: A schematic of our experimental setup (figure adapted from [39])

generation (SHG) Frequency Resolved Optical Gating (FROG) [38].

2.2 Beamlines

A schematic of the experimental apparatus is shown in figure 2.1. The amplifier output was split into two parts, each propagating along one of the arms of a Mach-Zender interferometer. About 80% was directed into a series of non-linear crystals used to generate the UV pump pulse. The crystals consist of a 250 μm beta barium borate (BBO) cut for second harmonic generation from 780 nm light, a calcite used for group velocity dispersion (GVD) compensation, and a 100 μm BBO cut for sum frequency generation (SFG) from the fundamental (780 nm) and the second harmonic (390 nm) light. In order to optimize the conversion efficiency and mode quality, the tripling setup was placed in a diverging beam after a focus. The focal region was enclosed in rough vacuum to avoid breakdown of the air. Given an input of about 800 mW of the fundamental, the tripling setup can produce up to 25 mW of ultraviolet light at $\sim$ 260 nm. The UV pulses are directed into a 4-f configuration, acousto-optic modulator based pulse shaper, capable of independently altering its phase and amplitude [40, 41]. The pulse shaper is described in more detail in section 2.5. After the pulse shaper, the UV pulses have an energy of about 2 μJ. When not shaped, the pulses are close to being transform-limited with a sub-50 fs duration. The pulses have been characterized by a self-diffraction FROG [38, 41, 42]. A typical pulse at the output of the pulse shaper is shown in figure 2.5. A half wave plate was placed in the UV beam in order to control its polarization in some of the experiments.

Approximately 20 % of the laser output is directed into the probe arm, which contains a delay stage and a variable neutral density filter used to vary the delay and energy of the IR probe pulses. The UV and IR pulses are collinearly combined at the output of the Mach-Zehnder interferometer using a dichroic mirror and focused by a 150 mm fused silica lens into an effusive molecular beam. In order to correct for the chromaticity of the common focusing lens, an additional pair of lenses was placed in the IR beam to produce a slightly converging beam before the shared lens.

2.3 Time-of-flight mass spectrometer

The core of the experimental setup is the interaction region, where the laser beams are incident on molecules inside of a weak static electric field. The interaction region was placed inside a vacuum chamber, where the pressure was on the order of $1 \cdot 10^{-6}$ Torr. The molecules were admitted into the vacuum chamber through a small nozzle as an effusive molecular beam. The weak static electric field was produced by the plates of a time-of-flight mass spectrometer (TOFMS) with a dual slope extraction configuration and a mass resolution figure of merit $\Delta m/m$ greater than 200. Here m is the mass of an ion and Δm is the full width at half maximum value of the peak in the mass spectrum associated with this fragment. A typical time-of-flight mass spectrum of uracil is shown in figure 2.7. Molecular fragment ions, produced by laser photoionization, are accelerated by the electric field, and pass through a pair of small holes in the acceleration plates and are injected into a field-free region of the mass spectrometer that provides a temporal separation of ions differing in their mass to charge ratios. Since most of the ions observed were only singly ionized species, we effectively had a mass-resolved signal. The ions were collected by a microchannel plate (MCP) based detector in the Chevron configuration,

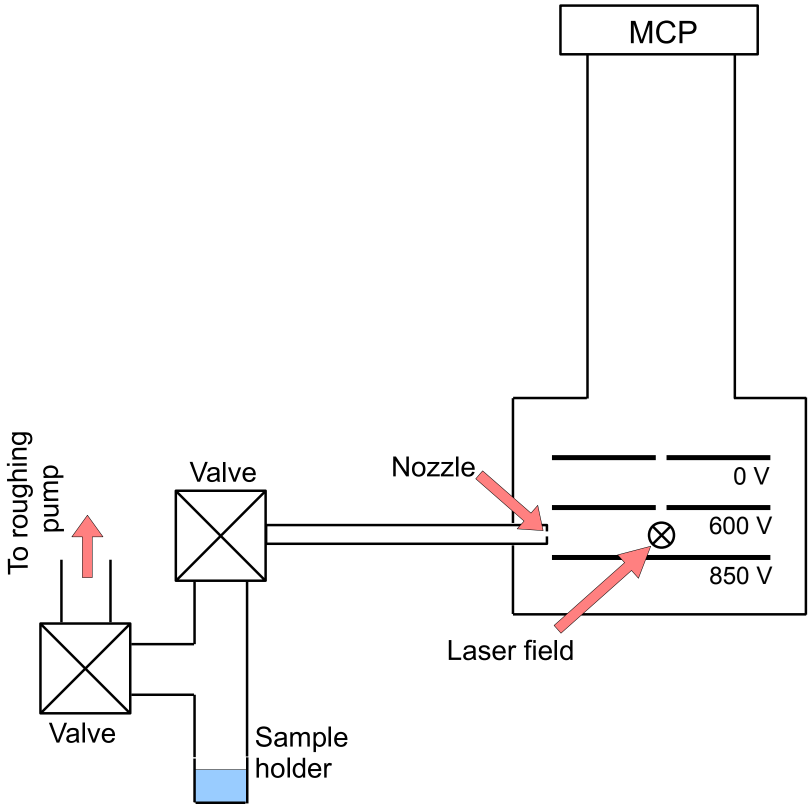

Figure 2.2: Schematic of the TOF setup and the sample manifold

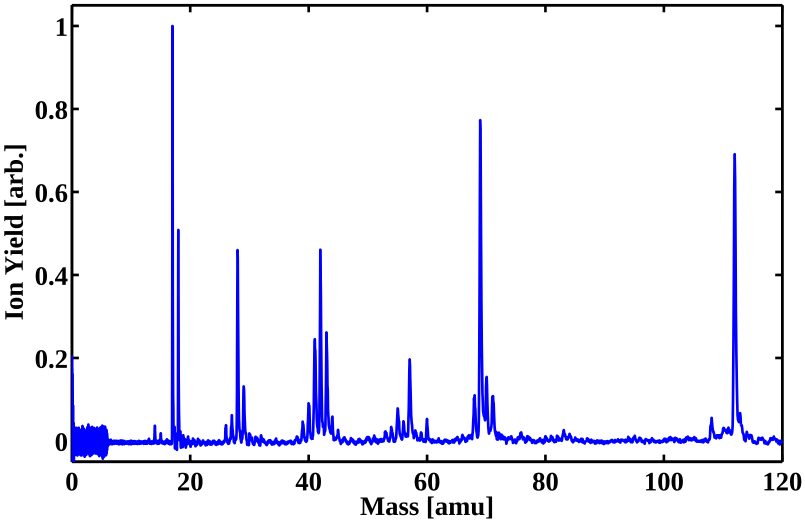

Figure 2.3: A typical time-of-flight mass spectrum of uracil

which provided a gain of about 10^6. The signal was subsequently amplified using a 350 MHz pre-amplifier (Stanford Research Systems SIM914), and the time-dependent ion current was digitized by a 500 MHz, 8-bit computer based oscilloscope (GAGE Compuscope 8500).

The digital oscilloscope was inside the computer that controlled the pulse shaper. This allowed for the implementation of closed-loop learning control, where the feedback signal is based on the molecular ionization yield. Details regarding the learning algorithm we used are given in [43].

2.4 Comparison of ionization-based methods

Experiments presented in this thesis utilize strong-field dissociative ionization of molecules as a part of the detection scheme. In this type of experiments, a ground or excited state molecule is ionized by an intense infrared laser pulse. If the energy of the cation that is produced by ionization exceeds a certain threshold, the cation can dissociate into several fragments. In the case of single ionization, only one of the fragments will carry a charge and therefore be detected. The departing electron was not detected in experiments described here.

An important complement to the time-resolved strong-field dissociative ionization is the weak-field photoelectron spectroscopy. The time resolved variation of this method is known as time-resolved photoelectron spectroscopy (TRPES) [44]. In this method, the molecules are ionized by a single-photon probe pulse, typically in the UV region of the spectrum, and an energy spectrum of the departing electrons is detected. A major disadvantage of this TRPES is that the limited photon energy available from conventional UV laser sources limits the access of this method to lower-lying ionic states.

In addition, high harmonic generation, whereby an energetic photon is emitted following strong-field ionization of an electron and its recombination with the ion, has been used to probe molecular structure and dynamics [8]. This method is technically demanding, but it can provide a 100 as time resolution when the recollision process itself is used to probe the dynamics [7], compared to the $\sim$ 10 fs resolution that can be achieved by TRPES or strong-field dissociative ionization.

The angle-resolved ion signal of the weak-field and HHG methods can readily be related to the Dyson orbital of the ionization channel [45]. The interpretation of angle strong-field ionization yields is more involved. It is the subject of chapter 5. It is possible to use strong-field ionization to study the ionization of excited state molecules using alignment through selective excitation. The exponential sensitivity of strong-field ionization to the ionization potential suppresses ionization of ground state molecules that are present in the sample when using selective excitation. In contrast, TRPES and HHG require the molecules to be non-adiabatically aligned, which is not easy asymmetric top molecules, such as uracil, that was studied in this thesis.

2.5 Pulse shaper

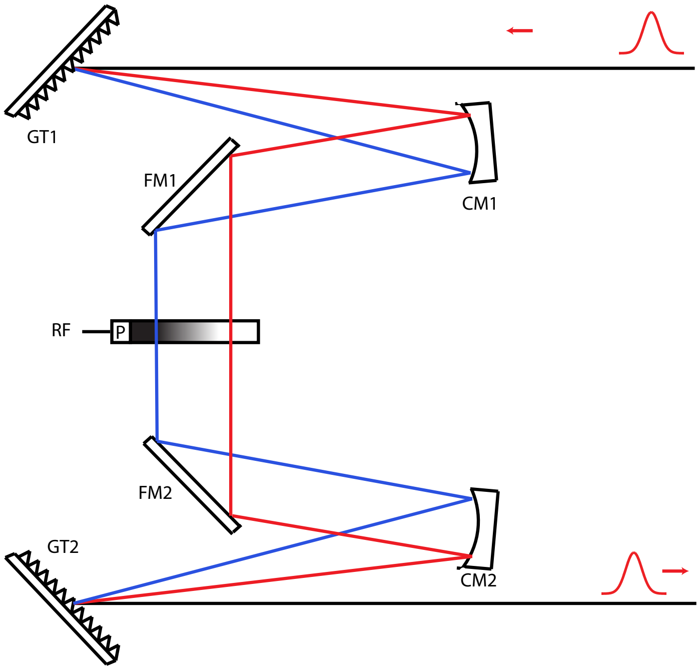

Figure 2.4: Diagram of the pulse shaper. Here GT1 and GT2 are diffraction gratings, CM1 and CM2 are curved mirrors, and FM1 and FM2 are fold mirrors (figure taken from [46]).

The pulse shaper used in the experiments is shown in figure 2.4. The shaping is done in the Fourier plane, in a scheme first proposed by Weiner [40]. The pulse shaper employs a 4-f configuration, where the beam is first spatially separated into different frequency components using a diffraction grating. The beam is then collimated by a curved mirror, placed at a focal length, f, distance from the grating, and subsequently focused another focal length f away from the curved mirror. The shaping element, in the Fourier plane, is a fused silica acousto-optic modulator (AOM). Acoustic waves propagating through the fused silica element are produced by a piezoelectric attached to it and driven by a 150 MHz radiofrequency (RF) wave of 2 W peak power. The AOM acts as a transmission grating, with the acoustic wave producing regions of varying density that are analogous to the grooves of a conventional grating.

Given the length of the fused silica element of 20 mm and compression wave acoustic velocity of 5960 m/s, it takes 3.360 μs for the acoustic wave to cross the AOM. Since the sample rate of the RF waveform generator is 1 GHz, the waveform we write is 3360 pixels long. The bandwidth of the AOM is 50 MHz, corresponding to a rise time of 20 ns, and limiting the total number of independently controllable points to about 170 across the AOM. The basic RF waveform written on the AOM has the following form:

$$f(pixel) = 4095 \cdot \frac{1}{2} \cdot (A(pixel) \cdot sin(2\pi\omega_0 \cdot pixel + \varphi(pixel)) + 1) \qquad (2.1)$$

where A is the amplitude (ranging between 0 and 1), ω_0 frequency (in GHz) and φ phase of the sine wave. The domain of $f(pixel)$ is [1, 3360] with the variable $pixel$ given in ns, while its range is [0, 4095], corresponding to a 12-bit, 1 GHz D/A board (GaGe 11G CompuGen). Functions A and φ, defined in the [1, 3360] domain, allow for independent shaping of the amplitude and the phase of the laser electric field.

A typical pulse at the output of the pulse shaper is shown in figure 2.5.

2.6 Heated nozzle setup

In order to use powdered DNA and RNA samples, which require temperatures of about 140-180^{o}C to achieve a high enough vapor pressure through sublimation, a new sample manifold with a heated injection nozzle was designed and built. The vacuum chamber, with the oven attached is shown in figure 2.6. The manifold consists of stainless steel conflat vacuum fittings. Heavy insu-

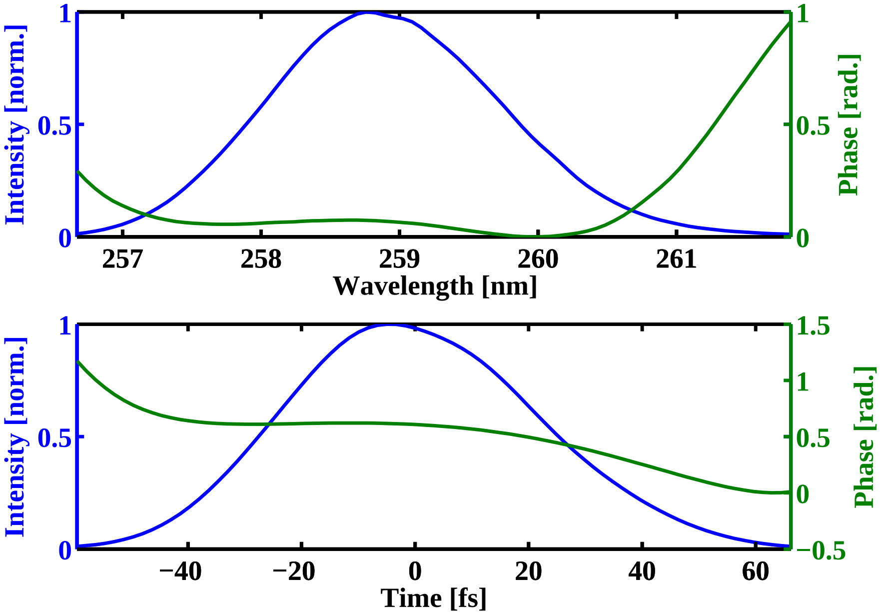

Figure 2.5: A typical pulse at the output of the pulse shaper. Top panel: Pulse intensity and phase in the spectral domain, Bottom panel: Pulse intensity and phase in the temporal domain.

lated laboratory heating tapes were used to keep the walls of the sample holder and the sample manifold at a high temperature. Several K-type thermocouple junctions were used to monitor the the temperatures of different parts of the manifold.

In order to insert the sample into the interaction region, which was kept at ultra-high vacuum pressures through a continuously open nozzle, it was necessary for the nozzle diameter to be relatively small (0.5 mm). The nozzle was mounted on a 0.25” stainless steel tube that was protruding into the ultra-high vacuum chamber and pointing towards the interaction region. The nozzle was heated using high-resistance Nickel-Chromium wire (80% Ni, 20% Cr), with a diameter of 0.81 mm and resistivity of 0.63 Ω/ft. Ceramic beads were strung around the wire, providing electrical insulation without compromising its flexibility. An additional K-type thermocouple junction was placed in vacuum close to the nozzle, in order to monitor its temperature. The heating required about 50 W of power for parts of the oven that were in air, (wrapped in 50 Ω heating tapes, with 50 V supplied to each tape by an autotransformer), and about 16 W for the nozzle that was in vacuum (8 V and 4 Ω). The vapor pres-

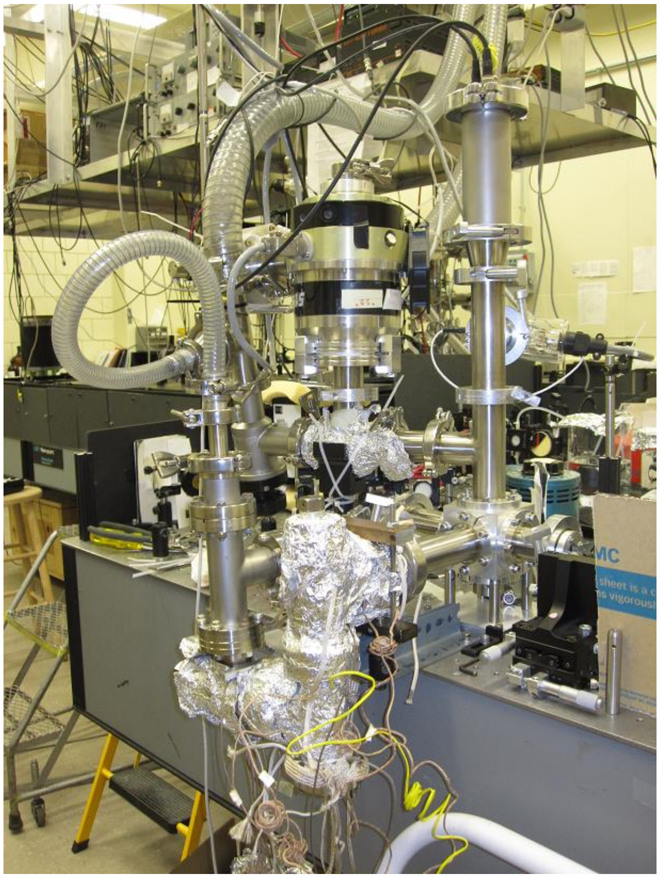

Figure 2.6: The vacuum chamber, with the powdered sample manifold attached

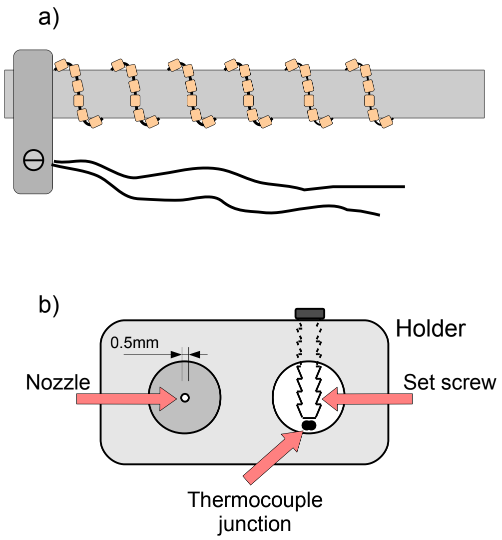

Figure 2.7: Heated nozzle setup. Panel a) Top view of the tube, the heating wire with ceramic beads, and the thermocouple junction holder; b) front view of the same (2× maginified compared to panel a))

sures in the oven were on the order of several mTorr [47–50]. The operating temperatures were 150°C, 180°C, and 145°C, for adenine, cytosine and uracil, respectively. In the case of cytosine, which also has the lowest vapor pressure of the three bases studied, there were significant issues with sample damage that forced us to limit the temperatures to up to 180°C, at the expense of low vapor pressure and poor signal to noise.

Chapter 3

Closed-loop learning control of isomerization using shaped laser pulses

3.1 Introduction

In this chapter, we present the results of closed-loop learning control of a photochemical isomerization reaction. The reaction is initiated by an absorption of a pump pulse in the deep ultraviolet, and takes place during the ultrafast relaxation of the molecule. Learning control is effected by shaping the excitation laser field, and optimal pulse shapes are found by applying a learning-control scheme based on the genetic algorithm [51, 52].

The isomerization reaction studied in this chapter is the photochemical ring opening of 1,3-cyclohexadiene (CHD). The opening of this ring molecule leads to the production of cZc-hexatriene (HT). The reaction is energetically precluded from taking place on the the ground state of the molecule, by a high barrier ($\sim$ 2.7 eV) [53]. A similar barrier ($\sim$ 1.5 eV) exists on the ionic ground state [53]. Instead, the ring opening proceeds on an excited state of the molecule.

Isomerization is a single-molecule reaction that involves a spatial rearrangement of the atoms that the molecule consists of. It can be accompanied by breaking of bonds, or by a more complex change in the way the constituent atoms are bound. Isomerization plays a role in processes such as vision and

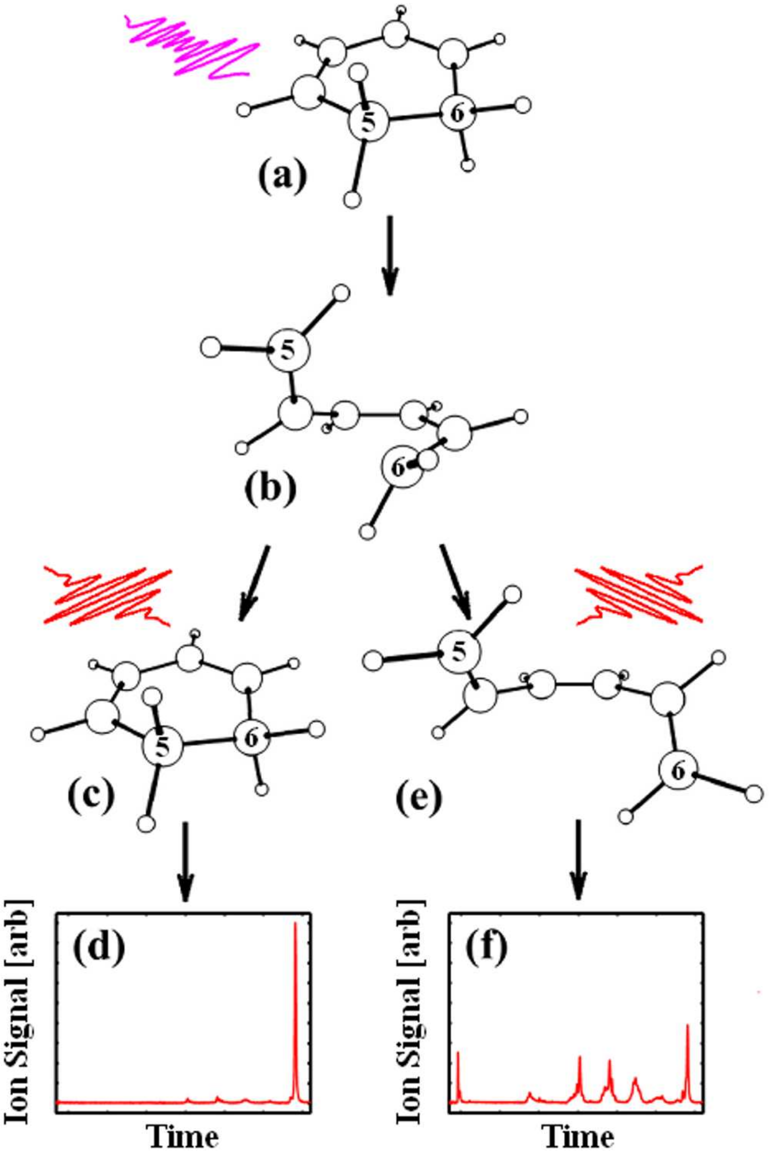

Figure 3.1: Cartoon of the experimental approach: The experiment starts with a shaped UV pulse interacting with the molecule initially in the CHD conformation (a). Following UV excitation it evolves towards a conical intersection (b) after which it can become CHD again (c) or undergo ring opening to become HT (e). Subsequent IR ionization leads to pronounced differences in the TOFMS for the two isomers (d) and (f). The geometries shown were derived by *ab initio* calculations, and the two TOFMS were measured on raw samples and presented here on the same vertical scale. Carbon atoms C^5 and C^6 are labeled in appropriate panels.

combustion [54, 55]. Controlling isomerization in molecular switches has drawn some attention in recent years [56–60]. Learning control of isomerization using ultrafast laser pulses has recently been demonstrated in the liquid phase [61–64]. Interpretation of results from liquid-phase experiments is complicated by solvent interactions and non-linear optical effects [65]. Experiments carried out in the gas phase are free of these problems and serve as an important complement to liquid phase experiments in trying to understand the underlying control mechanisms.

Experiments presented in this chapter were carried out in the gas phase, using a strong-field probe to ionize the molecules and detecting a mass-resolved signal of the produced ions. We make use of the differences in the ionization signal for the two molecules studied here, 1,3-cyclohexadiene (CHD) and its isomer 1,3,5-hexatriene (HT) following strong field ionization with infrared laser pulses [66]. These differences enable the distinguishing of the two isomers, and provide a feedback signal for the learning-control experiments.

In the accepted picture of UV-pulse initiated isomerization of CHD, a wavepacket is launched from the ground 1A state to the first excited 1B state [66–72]. The wave packet relaxes on the excited state, moving in the direction of an avoided crossing AC_{12} between the 1B and the two-electron excited state 2A, and crosses over to the 2A surface. Its evolution on this surface drives it towards a conical intersection CI_{01}, between the 2A and the ground 1A state. A sketch of the potentials, based on ref. [53] is shown in figure 3.2. Solution-phase measurements show that in passing through the CI_{01}, the wave packet bifurcates. About 40% of it relaxes to the minimum in the ground state corresponding to HT and the remaining 60% to the minimum corresponding to CHD [73]. The timescale for the relaxation process is about 200 fs [66].

Figure 3.1 provides a cartoon of our experimental approach. The CHD molecule is excited by a near-resonant UV pulse, which may or may not be shaped (a), whereby a wavepacket is created on the excited 1B state. The geometry of the conical intersection CI_{01}, is shown in (b). Carbon atoms C_5 and C_6, which form the bond that is broken to form HT, are labeled. The separation between these two atoms increases from about 1.6Å in CHD, to ~ 2.25Å at the CI_{01} geometry. Bifurcation of the wave packet after the CI_{01} conical intersection leads to either the retrieval of ground state CHD (c) or the

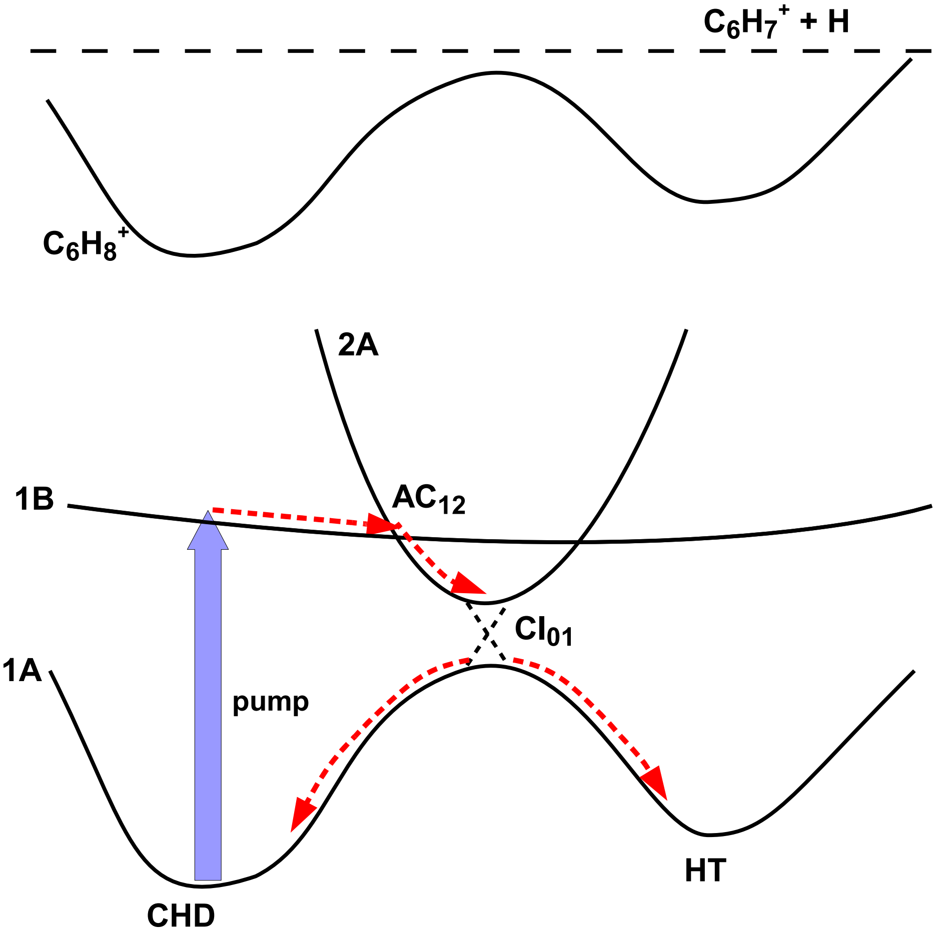

Figure 3.2: A sketch of the potential energy surfaces of CHD and HT relevant to the ring opening reaction. The realxation pathway is outlined in red dashed lines (figure based on potentials given in [53]).

production of cZc-HT, the HT conformer likely to be reached first in the ring-opening reaction, with a C_5-C_6 separation of about 3.5Å, shown in (e). Panels (d) and (f) show the time-of-flight-mass spectra of ground state CHD and HT upon illumination with intense ultrafast IR radiation. The strong IR pulse produces very different fragment yields for the two molecules. Specifically, the mass spectrum of HT shows a pronounced decrease in the parent ion yield, and an increase in fragment ion yields. We make use of this difference to distinguish whether the molecule ends up as CHD or HT after going through the CI_{01} conical intersection by illuminating the sample with an intense IR probe pulse approximately 1.8 ps after the UV pump.

While different conformers of hexatriene are accessible from the CI_{01} conical intersection, no significant differences between their fragmentation patterns or ionization yields have been found [66], allowing us to observe and quantify the ring-opening of 1,3-cyclohexadiene without considering further changes in conformation that the newly created hexatriene might undergo.

Below, we briefly introduce the control scheme used and the ab initio electronic structure methods used to optimize the geometries and calculate the energies of the two isomers. After this, the results of both calculations and experiments are presented. The experimental results are interpreted using findings of ab initio calculations.

3.2 Closed-loop learning control

The goal of laser control of quantum systems is to drive the system to a desired final state. In order to achieve this, the laser field is shaped using pulse shaping techniques similar to those described in chapter 2. Since solving the Schrödinger equation for most multi-particle systems is not possible analytically and very time-consuming numerically, the full dynamics of most systems is not known and it is in general not possible to a priori tailor the field to achieve a specific final state. One commonly used approach is that of learning control, one example of which is the genetic algorithm [52], so named for its similarity with biological evolution. In this scheme, a number of pulse shapes (i.e. field shapes) are tested for their performance in achieving a specific goal on a given system. In the case of molecular systems and ion-based detection, the goal is usually quantified in terms of yields of ionic fragments. This allows for ranking of pulses, where a numerical value is assigned to each of them. In the next iteration, the poor performers are eliminated from the population, while the high performers are kept, and allowed to mate and mutate. Details of the genetic algorithm used in experiments presented in this chapter can be found in references [74].

Ideally, pulse shapes discovered in a closed-loop learning experiment can be connected to physical process underlying the control. In order to achive this, it is helpful to bias the learning algorithm towards finding simpler pulse shapes [75]. While learning algorithms, provide a time- and resource-efficient way of finding the optimal pulses for controlling molecular dynamics, the discovered pulses do not in general lend themselves to a simple explanation of the control mechanism. In the case of molecules, a detailed knowlegde of the potential energy surfaces is often necessary, coupled with considerable interpretation efforts.

3.3 *Ab initio* electronic structure calculations

Calculations presented in this section have been done in collaboration with and under the guidance of Prof. Spiridoula Matsika of Temple University. We used *ab initio* quantum chemistry methods to calculate the properties of CHD and HT molecules, which will be detailed below, after a brief introduction to the computational methods.

Ab initio methods solve the molecular time-independent Schrödiger equation, $\widehat{H}\Psi(\vec{R},\vec{r}) = E\Psi(\vec{R},\vec{r})$ by approximating the molecular wavefunction with linear combination of atomic orbitals (LCAO). Each atomic orbital is approximated by a sum of Gaussians. The use of Gaussians is motivated by the fact that, as a consequence of the Gaussian product theorem, it allows for a quicker calculation of overlap integrals, leading to a significant reduction in the computational resources needed [76]. Each of the individual Gaussians is known as a Gaussian primitive. The general form of a Cartesian Gaussian primitive, centered on a given atom is:

$$g(x,y,z) = N\cdot(x-x_0)^l\cdot(y-y_0)^m\cdot(z-z_0)^n\cdot e^{-\zeta(\mathbf{r}-\mathbf{r_0})^2}, |\mathbf{r}|^{\mathbf{2}} = x^2+y^2+z^2, \quad (3.1)$$

where N is the normalization factor, x, y, and z are the Cartesian coordinates, (x_0, y_0, z_0) are the coordinates of the atom, ζ is the exponent used to set the spatial extent of the primitive, and l, m and n are positive integer exponents of the Cartesian coordinates. The sum L=l+m+n can be thought of as an analogue of the angular momentum. Primitives with the sum L=0 are called s-type, those with L=1 p-type, etc.

A basis function used in molecular calculations to describe an atomic orbital is typically a contraction, or weighted sum of several Gaussian primitives. Split-valence atomic basis sets, such as the one used in calculations presented here, are generally denoted as X-YZg, where X is the number of primitives used to describe each core orbital electron, while the valence electrons are described by two basis functions (with different values of ζ), one consisting of Y and the other of Z primitives. The coefficients of a basis set are optimized for each atom independently, and chosen so that they minimize the energy of a given atom.

The general form of the molecular wavefunction in the LCAO ansatz is $\Psi_{molecular} = \sum c_i \Psi_{atomic}$. Coefficients c_i are determined so as to minimize the total energy of the molecule using iterative variational methods. In this work we use the split-valence basis set with an additional polarization function, denoted 6-31G(d), which can model different bonding in different directions.

Solving the Schrödinger equation in terms of nuclear coordinates and molecular wavefunctions typically begins with the Hartree-Fock (HF) method. In this method, an electron is viewed as moving in the mean field of all the other electrons, and the wavefunction always contains just one electronic configuration. Restricted Hartree-Fock can be used when all molecular orbital are doubly occupied, and electrons of opposite spins in the same orbitals have identical energies. If there are unpaired electrons, unrestricted Hartree-Fock (UHF) method is appropriate, and electrons of opposite spins are treated separately. The HF method is variational, so the energy obtained from it is always an overestimation of the actual energy of a system.

3.4 Results of calculations

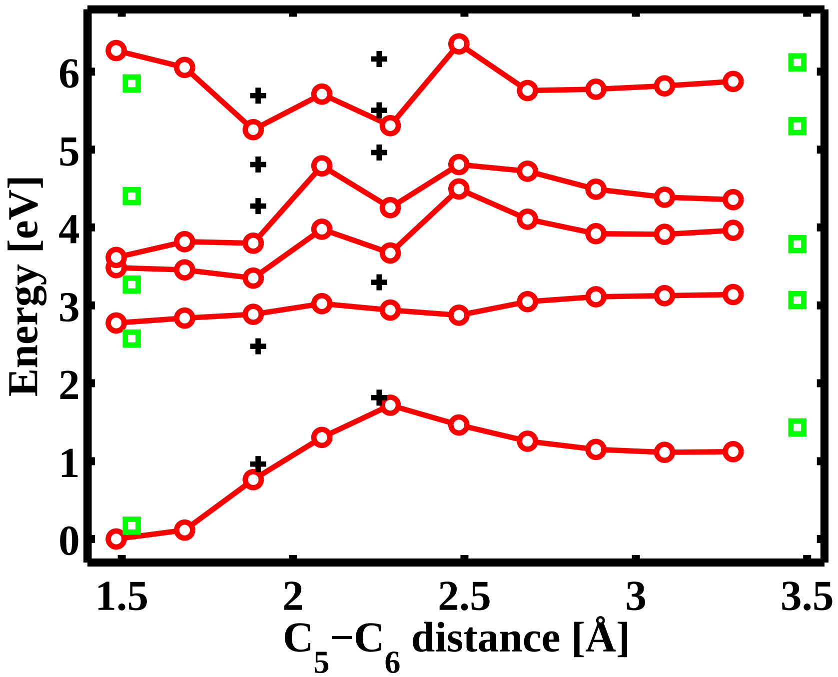

Figure 3.3: Circles and lines: MCQDPT2(8,10) calculation of the lowest 5 energy levels of CHD$^+$/ HT$^+$ for a relaxed potential energy scan along the C^5-C^6 bond length. Squares: energies of CHD$^+$ and HT$^+$ at the equilibrium geometries of the neutral CHD (left side) and HT (right side) respectively. Crosses: five lowest energy levels for the cation at the the geometries corresponding to the avoided crossing and the conical intersection in the neutral.

The ground states of both cyclohexadiene and cZc-hexatriene were optimized for the neutral and the singly ionized species. The optimizations were first done using the Hartree-Fock approach and a 6-31G(d) basis, restricted for the neutral molecules and unrestricted for the ions, and then improved on using second order Møller-Plesset perturbation theory, while keeping the same basis set.

Noting that the most significant difference between the equilibrium geometries of CHD and cZc-HT was the stretching and eventual breaking of the C^5-C^6 bond (see figure 3.1), we carried out constrained optimizations of the geometry of the neutral molecule along this bond. The optimizations were done at the UHF/6-31G(d) level. The C^5-C^6 bond was scanned in steps of 0.2 Å. In each step, this bond length was kept constant, while the other coordinates were relaxed. Energies of the ground and the first four excited states were calculated for these intermediate geometries at the multi-configurational self-consistent field (MCSCF) and second-order multiconfigurational quasi-degenerate perturbation (MCQDPT2) levels with the same basis set (shown in figure 3.3). The active space for these calculations consisted of 8 electrons in 10 orbitals (denoted (8,10)). The active space included all π and selected σ orbitals which participate in some excited states of the cation. The constrained minimizations provide ionic energies along a reaction pathway between HT and CHD.

We also calculated the energies of several excited states of the cation at selected geometries of the neutral photo-initiated reaction, corresponding to the avoided crossing AC_{12} and the CI_{01} conical intersection that have been reported before as important intermediates along the reaction path [70, 71]. A small multireference configuration interaction (MRCI) expansion with a reference space of 6 electrons in 6 orbitals (6,6) and single excitation configurations out of this active space was used to calculate the minimum energy point on the seam the conical intersection 1A/2A. The COLUMBUS software package was used for the CI optimizations [77, 78], while GAMESS [79] was used for all other calculations.

3.5 Experimental results

Figure 3.4 shows the $C_2H_2^+$ (a rough measure of the amount of HT in the sample) and parent ion yields as a function of time delay between the pump and the probe pulses. The pulse intensities were $\leq$10 TW/cm^2 for the UV pump pulse and $\sim$ 46 TW/cm^2 for the IR probe pulse. The pump-probe results demonstrate the dramatic changes in the fragmentation pattern of the molecule following irradiation with an ultrafast UV pulse. The parent yield decreases in going from negative to positive pump-probe delays, while the $C_2H_2^+$ yield increases in going from negative to positive pump-probe delays. These are consistent with formation of HT, whose mass spectrum shows a smaller parent yield and an increased smaller fragments' yield. The TOFMS for positive time delays shows a general trend of enhancing smaller molecular fragments at the expense of the parent, as one would expect with the formation of HT.

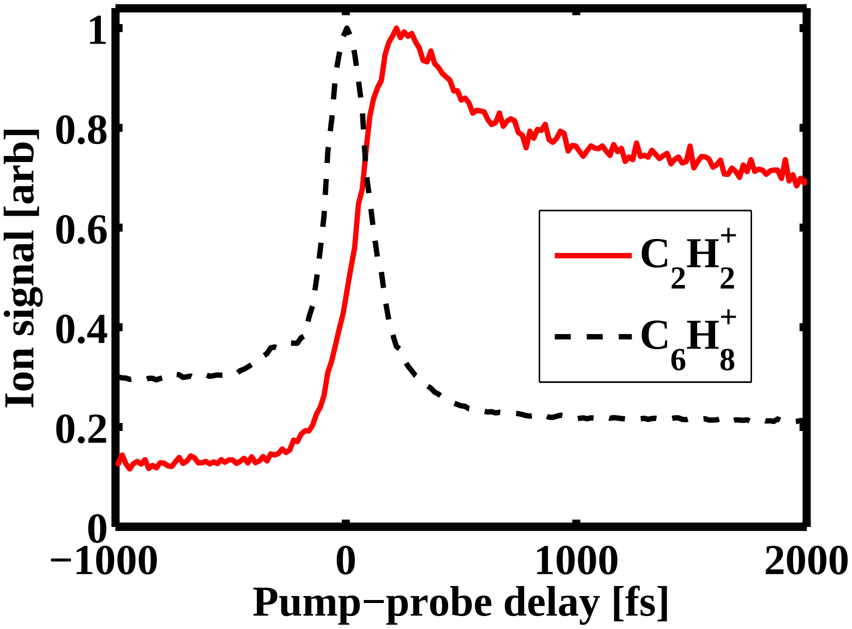

Figure 3.4: $C_2H_2^+$ and parent ion yields as a function of pump-probe delay. The signals are individually normalized to their maximum values.

The drop in the parent signal, accompanied by an increase in the $C_2H_2^+$ signal, is also consistent with the formation of vibrationally hot ground state CHD. The fragmentation pattern of vibrationally hot CHD is expected to exhibit a preference for fragment formation, similar to what is seen in the mass spectrum of HT. However, evidence in favor of the mass spectrum of hot CHD resembling that of cold CHD was reported in a recent spectral unmixing study [80]. This study suggests that the difference between spectra of vibrationally hot and cold ground state CHD are significantly smaller than the differences between the spectra of CHD and HT.

The parent ion yield peaks when the two beams are spatially and temporally overlapped. The pump-probe delay at which the $C_2H_2^+$ yield peaks is shifted towards longer delays with respect to the delay at which the parent ion peaks, consistent with the time required for isomerization to take place, and with the fragmentation pattern changing rapidly during the early stages of the relaxation process. These changes can be brought about by the excited state character changing in going through an avoided crossing, or later a conical intersection [66]. Another possible cause of the changes in the fragmentation pattern is the ionization potential increasing due to a rising ionic ground state energy (see figure 3.3) [32]. The existence of a single IR photon resonance in the ion at a geometry along the ring-opening pathway could also significantly influence the ratios of fragments produced by ionization. In the latter case, ionization when the wave packet is at this location can lead to efficient excitation of the ion and thus additional fragmentation [81].

Based on the pump-probe data, we performed control experiments at a delay of 1800 fs. This delay was chosen so that the results are not sensitive to possible optical effects that occur when the pulses are overlapped in time, or the changes in fragmentation that were observed in the early stages of the ring-opening reaction. Instead, our measured ion yields at this delay are an approximate measure of the amount of HT produced. The signal of all fragment ions increased in going from negative to positive time delays, and also when comparing the mass spectra of cold CHD and HT molecules. However, this increase was more pronounced for smaller fragments than for larger ones. The choice of fragment to feed back on in control experiments, C_2H_3, was a compromise between the differences in this fragment's signal from CHD and from HT and a favorable signal to noise ratio.

We found that control was sensitive to the intensity of our UV pulses. We needed to transfer enough population to the excited state to get sufficiently high ionization signal to be able to distinguish between performances of different shaped pulses. However, at higher UV intensities, the excitation was accompanied by two-photon ionization, enhanced by the one-photon resonance. It should be noted that ionic signal due to ionization by the pump can obscure the effects of the control by producing a larger background of small fragments in the time-of-flight mass spectrum, making the relative increase in the fragment ion signal due to control appear smaller. The ground state of the ion can be reached by absorbing two 4.75 eV UV photons, since the ionization potential of CHD is 8.25 eV. On the other hand, the lowest-lying dissociation channel ($C_6H_8 \rightarrow C_6H_7^+ + H$) lies more than two UV photons above the CHD ground state [82], and the absorption of at least three pump photons is needed to produce fragment ions by the pump alone. In contrast, in the pump-probe configuration, a molecule that has been ionized to its ground ionic state by the pump would be more likely to fragment after interacting with the probe. This is because many polyatomic ions absorb strongly in the IR due to their high density of electronic states. Thus an increase in the production of fragments compared to the parent ion is expected for molecules that have been ionized by the pump. Since shaping the pulse leads to a decrease in its intensity, this change in the parent to fragment ion signal would be more pronounced for an unshaped pulse. Thus a part of the control effect could escape detection.

We took care to isolate the contributions from both the pump and the probe pulses to the total ion signal. The vast majority (95%) of the detected ion signal with the IR probe pulse alone was the CHD parent. After excitation with the UV pump pulse, the IR probe produces a substantial amount of lighter fragment ions (35% of the total signal). In order to determine how much of this increase is due to newly created HT molecules, we subtracted the UV alone counts, since these ions come from molecules that did not undergo internal conversion from CHD to HT.

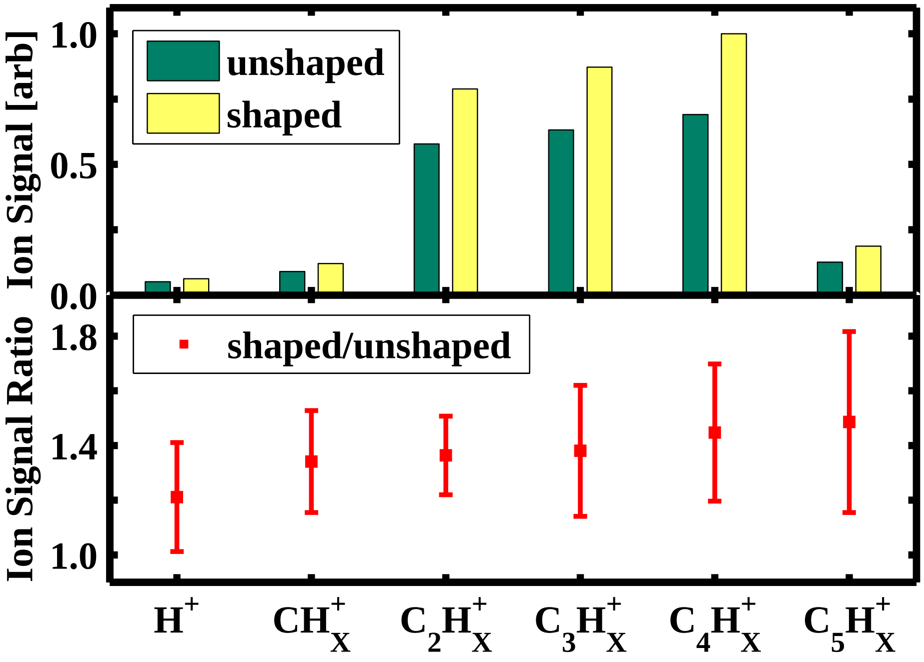

Figure 3.5: Top panel: peak integrals with the unshaped and the shaped pulse (UV background subtracted), Bottom panel: shaped/unshaped peak integral ratios.

Figure 3.5 shows results from a typical pump-probe feedback control experiment. The fragments have been grouped according to the number of carbon atoms they contain, and the UV background has been subtracted. The top panel shows the pump-probe ion signal for each of the groups of fragments obtained with the unshaped UV pulse and with the optimal pulse shape obtained in closed-loop learning control experiments. The bottom panel of the figure shows the ratios of ion signals in the top panel. The error bars in the bottom panel correspond to the standard deviation of the ratio from three different GA runs. All the fragment signals show a clear increase with shaped pump pulse, ranging between 21% and 49% relative to an unshaped pulse. The average increase relative to the unshaped pulse is $37 \pm 10\%$.

We note that, while the ionization signal increases by 37% on average in going from an unshaped pump pulse to an optimally shaped pump pulse, the ionization signal cannot provide a direct measure of the amount of each isomer in the sample of molecules that were probed. In other words, it cannot be used to determine the branching ratio with the unshaped or the shaped pump pulse.

3.6 Discussion

Figure 3.3 shows the energies of the first few ionic states of the molecule as a function of the length of the bond between atoms C^5 and C^6, whose lengthening and breaking is involved in the isomerization. The changes of these energies along the C^5-C^6 can be used to explain the different fragmentation patterns of the two isomers. The gap between the ground and first excited states is about 3 eV, in CHD^+, whereas the gap in HT^+ is about 2 eV. The calculations agree with the measured gap from photoelectron spectra in HT (1.97 eV) [83, 84], and previous calculations [85]. The smaller energy gap between the ground and first excited states of HT^+ leads to the probe pulse populating the excited ion states, whereas the larger gap in CHD^+ leads primarily to populating the ground ionic state.

As evident from figure 3.3, there are one-probe-photon resonances along the ring-opening pathway. At the geometry of the CI between the ground and first excited state, which is where the bifurcation occurs, the gap between the ground and first excited state of the cation is ~ 1.5 eV. This resonance may be causing the increase in fragment ion signal observed at short pump-probe time delays in fig. 3.4

There are several mechanisms by which the shaping of the pump pulse can influence the outcome of an isomerization reaction on an excited state. Three different possibilities which we have considered involve manipulation of the wave packet at three different times during its relaxation - the first during the wave packet launch, the second as the wave packet nears the CI, and the third as the portion of the wave packet that did not lead to isomerization reaches the CHD minimum.

The first mechanism is the control of wavepacket evolution by controlling its momentum as it is formed on the 1B potential surface with a shaped excitation pulse. Even though the excitation of CHD is a one-photon process, control should still in principle be possible since the molecule is not a closed quantum system [59, 86, 87]. Alternatively, the control could be through pump-dump-pump scheme. In both cases, control over the momentum of the wave packet as it crosses the 1B-1A CI, influences the CHD/HT branching ratio at the CI [63, 88].

A second mechanism would be the dressing of excited state potentials in the vicinity of the CI by the field of the pump. The new, dressed states would lead to changes in the evolution of the wavepacket close to the conical intersection, leading to changes in the branching ratio. The time required for the wavepacket to reach the second conical intersection is about 130 fs [66]. This is longer than the unshaped pump duration, but shaping can produce UV pulses that have a non-zero intensity at the time when the CI is reached. However, the large detuning of the UV pulse from both the 1B-2A and 1A-1B energy separations near the CI should result in weak dynamic Stark shifts and thus leads us to suspect that this mechanism is not responsible for the control.

A final mechanism we consider is wavefunction "recycling". Since it takes about 200 fs for the wavepacket to reach one of the minima, either the CHD or HT, after the molecule is excited portions of the wave packet excited by earlier parts of the pump pulse may have returned to the ground state as later parts of the pulse arrive. Thus the part of the wavefunction that relaxes back to the CHD minimum could be re-excited by the same pump pulse and have another chance of making it to the HT minimum [64]. Such repumping could

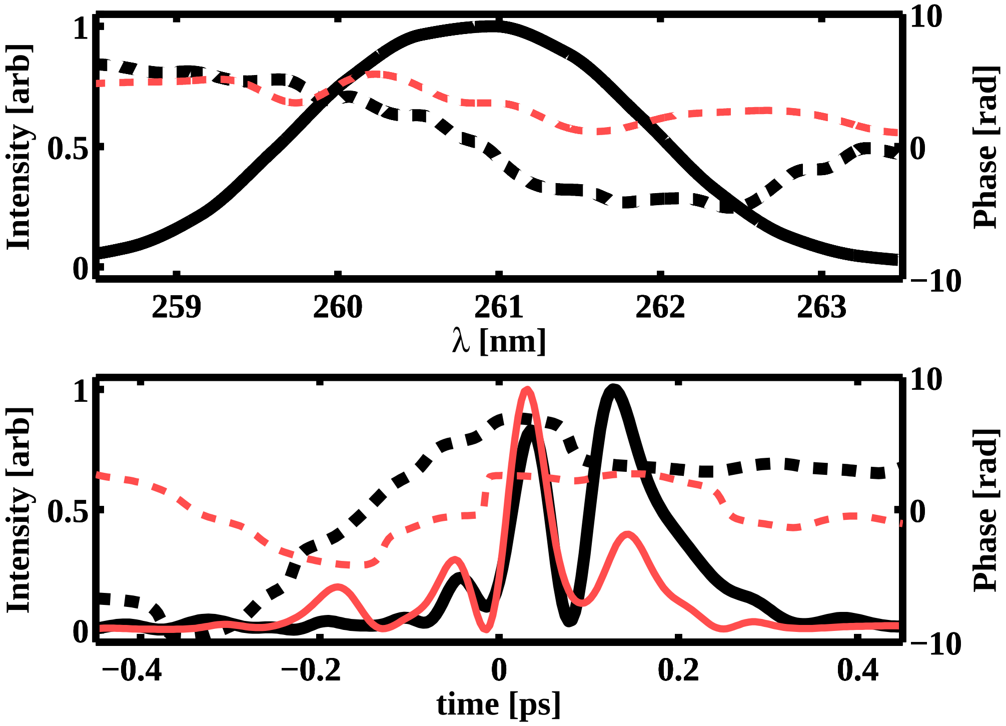

Figure 3.6: Top panel: Spectral phases and corresponding spectral intensities of two of the optimal pulses found by the GA. Bottom panel: Temporal phases and intensities for the same two pulses. Dark lines represent the results of a GA run at full intensity, while the light lines represent the results of a run at 20% of this intensity. Solid lines are used for intensities while dashed lines are used for the phases.

be repeated several times, transferring most of the population to the HT side of the barrier. This would suggest an optimal pulse shape with a duration of several hundred femtoseconds, and possibly a pulse train structure.

The optimal pulse shapes produced in closed-loop learning control experiments display features that are consistent with all three control mechanisms: they are typically over 100 fs in duration, and many optimal pulses displayed two or three sub-pulses with a spacing between 80 and 150 fs. Figure 3.6 shows two of the pulse shapes obtained in closed-loop learning control experiments. The top panel of this figure shows the pulse intensity and phase in the spectral domain, while the bottom panel shows the temporal intensity and phase.

The periodic structure of the pulse shapes found in our GA experiments might be related to other published data on the CHD/HT system. For example, coherent oscillations with a period of 109 fs were reported on the excitesd 1B state, as well as 66 fs oscillations on the ground state of CHD [89]. Our 80-150 fs features are consistent with the 1B oscillation, or the first overtone of the ground state period (due to our limited bandwidth). Pulse trains with a period of about 250 fs have previously been reported in learning-control experiments in the liquid phase [64].

Work is currenly under way aimed at testing whether the pulse sequences found by the genetic algorthm and described above correspond to a wavepacket oscillation on the 1B state. We are also investigating whether the branching ratio at the conical intersection between the 2A and 1A states can be influenced by launching multiple wavepackets and allowing them to interfere on one of the excited states' surfaces. The planned experiments will include the so called, "pump-pump-probe" scheme. In this scheme, the molecules are excited from the ground to the first excited state twice, using two pump pulses, each of which only lifts a small portion of the total population to the excited state. The probe pulses follows the two pump pulses, at a fixed delay with respect to the second pump pulse. This pump-probe delay will be kept at over 1 ps, following the reasoning for picking this time delay for the control experiments. Using a pulse shaper, it is possible to vary the time delay and the phase difference between the pulses independently, and to record the mass spectrum for each delay. If the ion signal peaks at a certain pump-pump delay, it will be interesting to see if that delay is consistent with any of the three proposed control mechanisms.

3.7 Conclusions

Our measurements and calculations demonstrate the use of strong-field dissociative ionization as a diagnostic tool for gas phase closed-loop control experiments when the different final states have identical atomic compositions but different geometries and fragmentation patterns. Our calculations show that we can understand the final state detection in terms of the geometry-dependent electronic structure of the molecular ion. We also demonstrate the use of shaped laser pulses to control a photochemical ring-opening reaction.

Chapter 4

Ultrafast excited state relaxation dynamics of isolated nucleic bases

4.1 Introduction

In this chapter, we present results of studies of excited state dynamics of nucleic bases. The bases included in this study are the building blocks of DNA and RNA, adenine, cytosine and uracil. They were studied in the gas phase, using ultrafast pump-probe methods, similar to those described in the previous chapter. We present data that support the idea that multiple pathways are being explored in parallel, i.e. that the relaxation is non-local.

Nucleic base monomer molecules absorb strongly in the ultraviolet, and this absorption leaves the molecule in an electronically excited state. The reactivity increases in going from the ground state to an excited state of a molecule, thus so does the likelihood of photo-induced damage. The photostability of DNA bases points to the existence of one or more highly-efficient relaxation mechanisms, and very little fluorescence is observed upon absorption of a UV photon [90–92]. This indicates the existence of one or more non-radiative relaxation pathways that connect the excited states of neutral bases to their ground state.

Excited state dynamics of the nucleic acid bases have been studied extensively experimentally and theoretically [90–92]. Experiments have been carried out in the gas phase, i.e. on isolated bases as well as on solvated bases. Ultrafast measurements of photoelectron yields [93], pump-probe transient ionization experiments [94, 95], and transient absorption measurements in aqueous solution have revealed picosecond and faster time scales [96].

Theoretical *ab intio* electronic structure calculations have identified multiple conical intersections (CIs) between electronic states of DNA and RNA bases [97]. The CIs enable ultrafast radiationless decay pathways for transferring excited state population back to the ground state. The details of excited and ground state potentials and the location of the CIs differ between bases. A common feature however is that there exists more than one pathway that can lead to a radiationless decay through conical intersections, but it is not clear whether one or more of them are actually explored during the ultrafast relaxation. Calculations aimed at finding the crossing point or seam of two electronic states are sensitive to the level of theory used and the quality of the wavefunction approximation (i.e. the basis set). The predicted accessibilities and relative prominences of pathways are sensitive to these parameters making it unclear which of the calculated pathways plays a central role. In order to determine which pathways and CIs play an important role in the relaxation, it is therefore necessary to establish an experimental signature of each of the relaxation pathways.

Ab initio multiple spawning (AIMS), a time-dependent formulation of quantum chemistry developed with the aim of modeling molecular dynamics involving multiple electronic states, has recently been applied to a number of organic molecules, including cytosine [29]. It has shown that a wave packet launched on the excited state of a molecule by an ultrafast pump pulse breaks up into multiple components which travel in parallel along different relaxation paths to the ground state, involving multiple CIs [29]. Recent dynamics calculations [98] give qualitatively similar results which indicate the importance of multiple relaxation pathways.

This theoretical picture of nonlocal relaxation along multiple pathways has not been directly tested in experiments. This is mainly because they either consisted of a single channel measurement (i.e. transient absorption measurements), or effectively a single channel measurement either by integrating over different photoelectron energies or ionic fragments in order to achieve a high enough signal to noise ratio for quantitative analysis [99, 100]. Extracting information regarding multiple competing relaxation pathways from a single channel time-resolved measurement (i.e. one yield for each pump-probe delay), can prove challenging. For example, in a study by Schultz et al. [99], data collected in a multichannel measurement, in this case a mass-resolved ion signal, was integrated and as a result only a single timescale was reported. In the following, we show how independent treatment of each fragment signal in the mass- and time-resolved ionization measurement can yield multiple time constants, indicating a spreading of the excited-state wavepacket. Further, we study the relaxation dynamics of cytosine from its S_1 state in detail, and demonstrate that both of the theoretically predicted disjoint pathways, each involving a different CI, are explored in the ultrafast relaxation.

While methods that utilize detection of photons associated with dipole allowed transitions between optically bright states of the neutral molecule are inherently single-channel measurements, they are well-suited for the study of relaxation dynamics in biologically relevant environments, i.e. on solvated molecules. In addition, methods that utilize detection of photons associated with dipole allowed transitions between optically bright states of the neutral molecule, such as fluorescence spectroscopy and transient absorption spectroscopy, are unable to offer insight into any excited state dynamics of DNA and RNA bases which involve optically dark states that are known to play an important role in the photophysics of nucleic base molecules [101, 102].

In order to access information about dynamics that involve optically dark states, one may turn to methods that include ionization of the molecule as a part of the detection scheme, such as time-resolved photoelectron spectroscopy (TRPES) or time-resolved ion yield measurements. In turn, extracting information from measurements using these methods may require information about ionic energies and geometries, in addition to neutral ones [103, 104].

In our approach, the dynamics were initiated by exciting gas-phase molecules from their ground neutral state, S_0, to a bright excited state. The $S_0 \rightarrow S_1$ or S_2 transition energy was close to the photon energy of our deep UV pump pulses. The ensuing relaxation was probed by strong-field dissociative ionization, effected by near IR probe pulses that interacted with the molecules after a variable time delay. We find that all three nucleic bases' ion signal rises sharply when the pump and the probe pulses are overlapped in time (time zero pump-probe delay), and subsequently decays. The ion signals of all fragments of the three bases decays rapidly, in about 100 fs, shortly after time zero pump-probe delay, and exhibits at least one longer, picosecond, decay timescale. The origins of these timescales are discussed in section 4.3.

All of the individual fragment ion yields resulting from dissociative ionization by the probe pulse were recorded. *Ab initio* electronic structure calculations were used to interpret the fragments' ion yields vs pump-probe delay. We make use of the observation that pump-probe ion yield signals differ qualitatively between fragments. We discuss how this information can yield separate timescales for individual pathways, and allow for labeling of different pathways involved in the neutral relaxation.

4.2 Tautomers of adenine, cytosine and uracil

A number of tautomers, lying low in energy, are present in some of the DNA and RNA bases that are the subject of this chapter. These tautomers can make up a significant fraction of sample after the heating and sublimation process used to obtain gas-phase molecules. Below we offer evidence in favor of the adenine and uracil samples consisting of a single tautomer at our operating temperatures. Cytosine sample, on the other hand, contains three tautomers, but only one of them contributes to the part of the dynamics we focus on in this chapter.

The lowest-lying tautomer of adenine is 9H-adenine, shown in figure 4.1a. The second lowest lying form, the 7H-adenine, shown in figure 4.1b, has a ground state that lies about 0.35 eV above the 9H-adenine ground state [105, 106]. Given this energy difference, and the temperature of the sample in the beam ($k_B T = 0.035$ eV), our sample consists almost entirely of the 9H-adenine. Uracil sample also contains only one tautomeric species, shown by core level photoabsorption spectroscopy experiments [107].

In cytosine, there exist three low energy tautomers: the keto, the enol and the keto-imino. Microwave spectroscopy measurements [108] predict the relative abundances of the three tautomers to be 1:1:0.25. The presence of these three tautomers has been confirmed by core level spectroscopy [107]. It

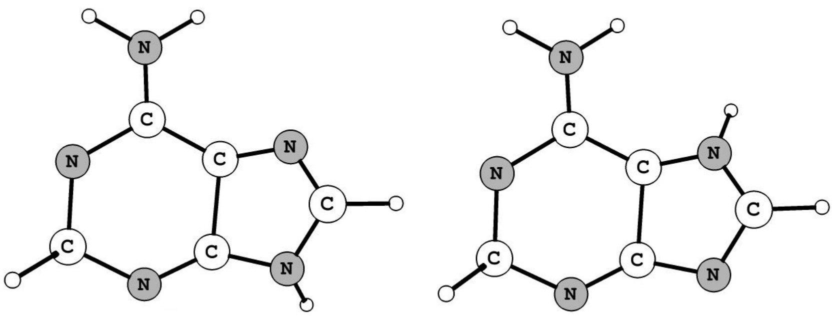

(a) 9H-adenine (b) 7H-adenine

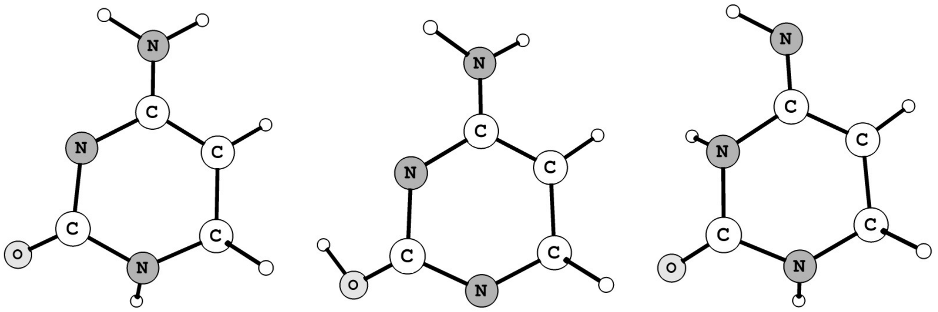

(c) keto cytosine (d) enol cytosine (e) imino cytosine

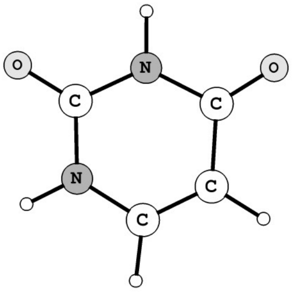

(f) uracil

Figure 4.1: Low-lying tautomers of adenine, cytosine and uracil

is in agreement with calculated ground state energies of cytosine tautomers, which show that the lowest lying is the enol cytosine, followed by the keto lying about 33 meV, and the keto-imino about 55 meV above it [99, 109].

Our pump laser at 260 nm (4.74 eV) is closest in energy to the excitation energy of the keto tautomer of 4.83 eV, with the enol and the keto-imino excitation energies being 5.19 and 5.14 eV. Based on a combination of the abundancies, Franck-Condon factors and oscillator strengths (0.08, 0.006 and 0.14 for the S_0-S_1 transitions in keto, keto-imino and enol respectively[109]), we expect that the dominant contribution to the fragments in our signal comes from the keto tautomer but we expect contributions from other tautomers as well.

The bright S_1 state in the keto-imino tautomer is an $n\pi^*$ state, and it is connected to the ground S_0 state of this tautomer by a conical intersection. The minimum on the S_1 state is separated by a 0.7 eV barrier from the CI [109]. In comparison, the barrier in the keto tautomer is <0.2 eV. Therefore, a much longer relaxation time is expected in the keto-imino tautomer than in the keto tautomer.

Calculations for the enol tautomer indicate that its bright state is the S_1 state. To date no conical intersections have been found between this state and the ground state. This prediction of a long-lived excited state population agrees with resonance enhanced multiphoton ionization (REMPI) measurements of deVries [110], which show a spectrum with many densely packed sharp lines for the enol tautomer, and few broad lines for the keto. The width of the broad features in the keto is consistent with a picosecond relaxation timescale. The lack of an accessible CI in the enol tautomer, together with its high excitation energy, leads us to discount its contribution to the picosecond timescales we discuss below.

4.3 Adenine, cytosine and uracil dynamics

In this section, we describe the generic features of ion signals of adenine, cytosine and uracil excited state dynamics. The neutral and ionic energies at several important geometries of the three molecules studied in this work are shown in figures 4.2,4.3 and 4.4. The lower portion of the figure shows the calculated neutral electronic state energies of adenine, cytosine and uracil at several geometries predicted to play a role in their relaxation dynamics. The geometries have been taken from previous studies [111–113]. The labeling of important points was chosen to be consistent with the published work on these systems. The eight lowest ionic states' electronic energies at important configurations along the relevant excited states of the three molecules are shown in the upper panels of figures 4.2,4.3 and 4.4. The energy of the lowest ionic state D_0 at the vertical excitation point has been set equal to the vertical ionization potential of cytosine, adenine and uracil (8.80, 8.40 and 9.60 eV) taken from photoelectron spectra [114–116].

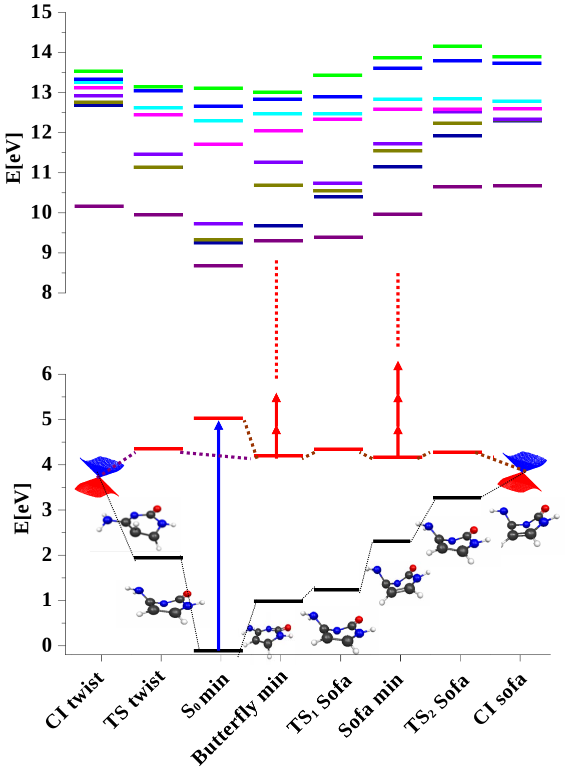

Figure 4.2: Neutral and ionic energies at some of the important points on the relaxation pathway on the S_1 PES of the neutral molecule for cytosine. Lower panel: Energies for neutral states taken from [111–113] (black: ground state, red: S_1 state). Upper panel: Energies for the eight lowest-lying ionic states. Dotted lines are used to mark predicted connections between the states.

Absorption of a UV photon at a central wavelength of 260 nm excites cytosine to the bright neutral S_1 state. Two energetically accessible CIs, and an additional one lying higher in energy have been found in theoretical studies [29, 109, 113, 117–124]. The two accessible CIs have been labeled 'sofa' and 'twist' in the original publication [113], to reflect the structure of the molecule at those points. There are therefore at least two distinct possible pathways of $S_1 \rightarrow S_0$ relaxation, each involving one of the CIs. There are two broad minima on the S_1 surface 'butterfly min' and 'sofa min', that are separated from the CIs by small barriers of similar sizes. The transition states associated with the barriers are labeled 'TS twist', 'TS_1 sofa', and 'TS_2 sofa'. It is not possible to determine which of the pathways is more prevalent than the other based on the theory only. The cytosine dynamics will be discussed in more detail in section 4.4.

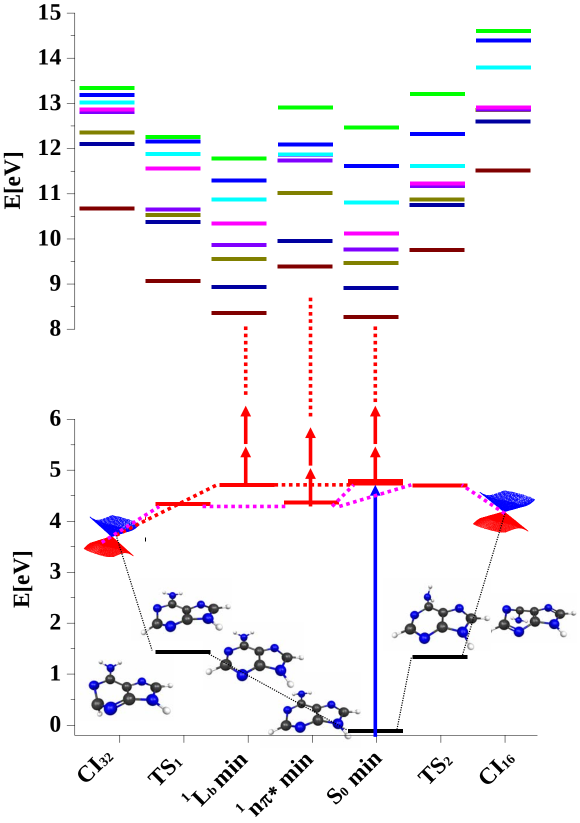

Figure 4.3: Neutral and ionic energies at some of the important points on the relaxation pathway on the S_1 PES of the neutral molecule for adenine. Lower panel: Energies for neutral states taken from [111–113] (black: ground state, red: excited states). Upper panel: Energies for the eight lowest-lying ionic states. Dotted lines are used to mark predicted connections between the states.

The case of adenine is more complicated than cytosine due to the existence of several neutral states that are close in energy at the neutral ground state equilibrium geometry. Theoretical studies predict that there are three states within 0.3 eV in the Franck Condon (FC) region, [125–134]. The brightest of these states is either the second or the third excited state of the neutral, though predictions vary with the level of theory. The two bright $\pi\pi^*$ states are labeled L_a and L_b, with the L_b initially lower in energy than L_a in the FC region, and the order switching as the molecule distorts. There also exists a dark $n\pi^*$ that is close in energy to the $\pi\pi^*$ states, and depending on the level of theory it has been predicted to be higher or lower than the two $\pi\pi^*$ states. Relaxation to the ground state can proceed through one of the two conical intersections, the CI_{32}, or the CI_{16} (shown in figure 4.3). The minima along the pathways leading to these CIs are the $n\pi^*$ min, and the L_b min. An additional relaxation channel has been suggested here where an NH bond is stretched significantly after initial absorption to a Rydberg state [125] leading to a CI between the excited and ground states. This channel is most likely accessed with shorter wavelengths than that of our pump [135].

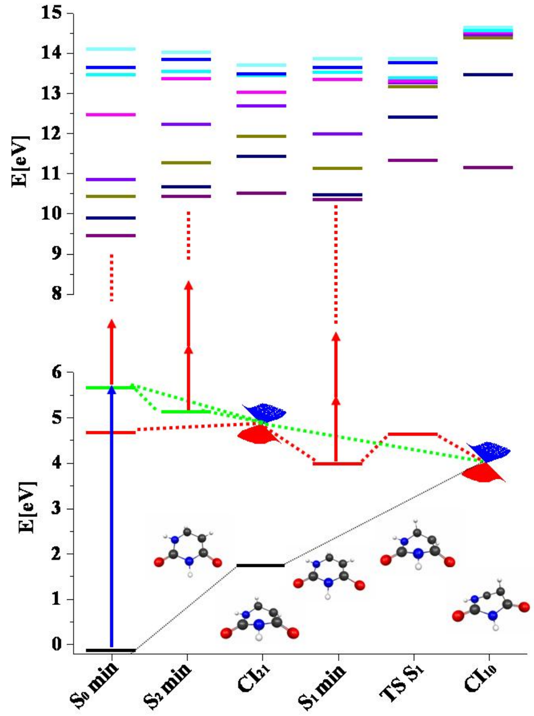

Figure 4.4: Neutral and ionic energies at some of the important points on the relaxation pathway on the S_1 PES of the neutral molecule for uracil. Lower panel: Energies for neutral states taken from [111–113] (black: ground state, red: S_1 state, green: S_2 state). Upper panel: Energies for the eight lowest-lying ionic states. Dotted lines are used to mark predicted connections between the states.

In uracil, the absorption of a UV photon at a central wavelength of 260 nm leads to the second neutral excited state, S_2. There are two conical intersections that can play a role in the non-radiative relaxation, CI_{21} and CI_{10}. There are two possible relaxation pathways. The first involves a WP on the excited state PES moving to the S_2 minimum first, then passing through the S_1/S_2 CI. The second one involves the WP moving directly towards the S_1/S_2 CI. After the S_1/S_2 CI, there is a branching leading to either a minimum in the dark S_1 state ('S_1 min'), or to another CI between S_1 and the ground state S_0 ('CI_{10}') [112, 119, 136–138].

Typical time-resolved ionization signals for the parent molecular ion and one significant fragment ion of the three nucleic bases are shown in figure 4.5. The measurements highlight similarities and differences between the three molecules' dynamics. In all three bases, both the parent and fragment ion signals show a steep rise of the yield at delays shortly after time zero, followed by a rapid drop shortly afterwards (∼100 fs), and a slower decays at longer delays (several ps). The location of time zero delay is determined by looking at the time-resolved signal of a molecule present in the chamber that lacks any dynamics. The maximum yield for different fragments occurs at different delay times, indicating that the peak in ion yield near zero time delay is not simply an optical artifact due to the combined pump and probe fields.

The steep rise in ion yields can be explained by the molecule being excited from the ground state to an excited state, whereby the IP is decreased by the pump photon energy of about 4.7 eV. This makes the molecule much easier to ionize, and accordingly the ionization yields increase sharply. The rapid decay at small positive time delays corresponds to the entire excited state wavepacket leaving the FC region. This is accompanied by an increase in IP, due to a rise in the ground state energy of the ion, and, to a smaller degree, the fall in the excited state energy in some of the molecules, as can be seen in figures 4.2,4.3 and 4.4. The signal near zero time delay decays most rapidly for uracil and the slowest for adenine, in accordance with the IP change in moving from the FC point.

The part of the excited state wavepacket that is confined by a barrier to a vicinity of a minimum on an excited state can lead to an exponential decay of the observed ion signal. Barriers separating a minimum on a PES and a CI often occur, and have been predicted by theory for nucleic bases studied here. A part of the wavepacket can pass the barrier and the conical intersection and cross over to a lower-lying electronic state with a high IP and stop contributing to the ionization signal. The total ionization signal is

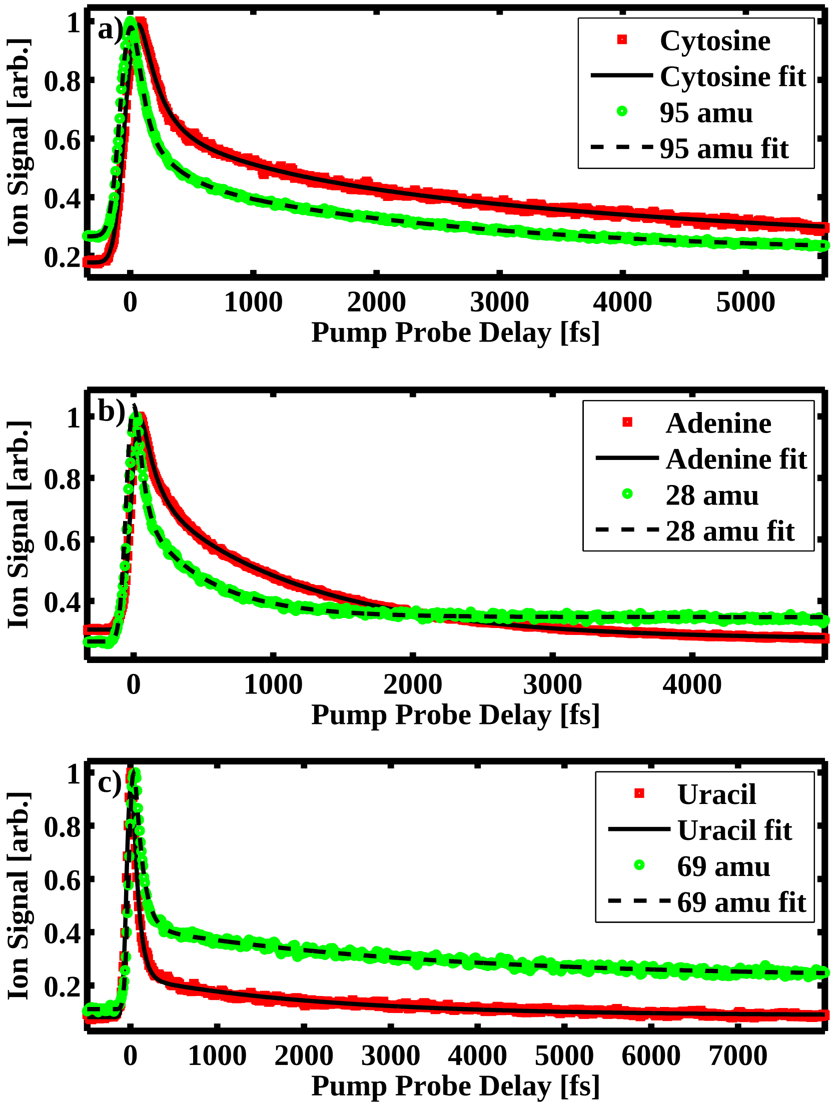

Figure 4.5: Parent and one selected fragment ion yield vs pump probe delay for cytosine, adenine and uracil.

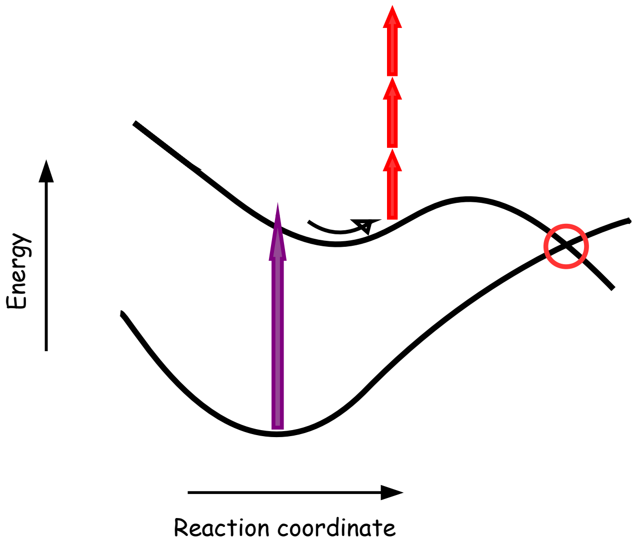

Figure 4.6: A cartoon of the excited and ground state of a molecule, with a single barrier en route to a conical intersection (CI). The existence of a barrier may lead to an exponential decay in the excited state population.

proportional to the population left in the excited state, and below we give arguments to support the exponential nature of the decay of this population.

The physical processes leading to an exponential decay in observed signals are not well understood at the moment. While tunneling leads to barrier crossing in one dimension, it may not be the dominant process in more than one dimensions. Energy pooling, where vibrational excitations need to be 'pooled' in the modes that contribute to the crossing of a barrier, has been suggested for relaxation in more than one dimension. In terms of nuclear displacements, energy pooling can be thought of as the motion along several normal modes with appropriate phases such that the displacement along a reaction coordinate extends past the point of the barrier [139].

Figure 4.6 shows a cartoon of a one-dimensional cut through molecular potential energy surfaces, with a single barrier separating a minimum on the excited state from a conical intersection connecting the excited to the ground state of a molecule.

There are multiple physical processes that can lead to a wavepacket crossing the barrier and the ionization yield before and after the barrier differing. Examples of processes enabling the wavepacket to pass a barrier are quantum tunneling and energy pooling. Energy pooling refers to the wavepacket, viewed

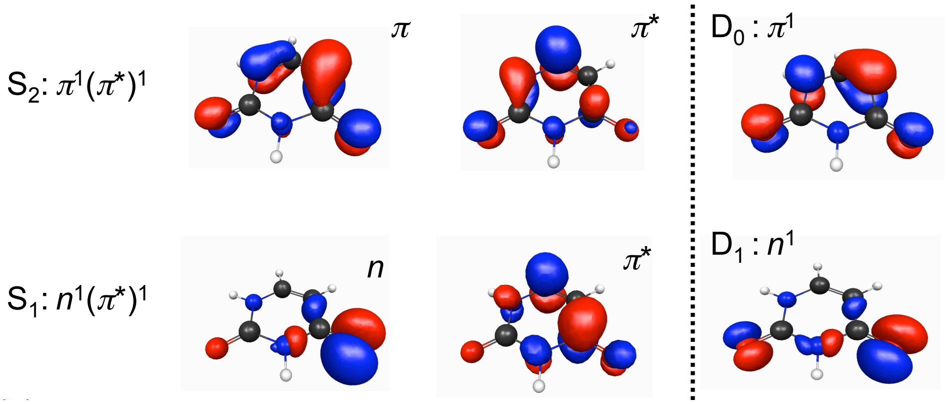

Figure 4.7: Natural orbitals of uracil, representing the excitation of the neutral states S_1 and S_2, and the natural orbitals representing the hole on D_0 are shown for one geometry (the S_0 minimum).

as excitations spread across several vibrational states, having a small but non-zero probability of enough vibrational excitation quanta being found in the mode that corresponds to movement in the direction across the barrier on the excited state. Both energy pooling and tuneling are exponentially sensitive to the height and the width of the barrier.

In addition to the changes caused by change in the ionization potential, the ionization rate depends on the shape of electronic wavefunctions of both the neutral molecule and the ion and especially on the degree of overlap between them. This dependence, and the concept of a Dyson orbital and its magnitude that is used to quantify the overlap, will be discussed in more detail in chapter 5. Passing through a CI between neutral states is usually accompanied by a change in the neutral wavefunction character, while the ionic wavefunction character may remain unchanged. A change in state character can lead to a change in the Dyson orbital magnitude and thus to a change in ionization yields.

In this picture, for example, removing an electron from an $n\pi^*$ state in uracil can lead to an n state. Natural orbitals, or one-electron wavefunctions associated with each of the orbitals of a molecule, are shown for uracil in Figure 4.7. The S_1 state has an $n\pi^*$ character and correlates with the first excited ionic state, D_1, which has a hole in an n orbital (HOMO-1). As S_2 corresponds to a removal of an electron from the π^* orbital (HOMO), it correlates with D_0. Based on the overlap of the natural orbitals for uracil, ionization from S_1 will lead to significant excited ionic state production, while ionization from the S_2 state will lead largely to D_0. This change in ionization pattern is expected in passing through CI_{12} between S_2 and S_1.

In order to quantify the observed differences in the observed pump-probe signals, we fitted the data to a convolution of a Gaussian with a sum of several exponentially decaying functions. The details of the fitting function and procedure are given in appendix A. We were able to describe the data for uracil and adenine well with bi-exponential decay although the cytosine measurements required a sum of three exponential decays for a good fit. These decay lifetimes are shown in table 4.1 and correspond to a fast signal decrease at short pump-probe delays, an exponential decay on the order of picoseconds associated with the wavepacket leaving one of the excited state minima, and a ledge at very long delays, that describes the part of the wavepacket that stays trapped in the excited state much longer than the longest pump-probe delay. The uncertainties were calculated as the standard deviation of the fit values from repeated pump probe measurements on different days. They were typically about 15%, but ranged from 9% to almost 50% for fragments whose ion signals had poor signal to noise.

Ion	A_1	τ_1 [fs]	A_2	τ_2 [fs]	A_3	τ_3 [fs]
Cytosine	0.72	50	0.17	240	0.14	2360
95^+ from cytosine	0.59	150	0.14	870	0.25	4680
Adenine	0.77	100	-	-	0.73	1140
28^+ from adenine	1.46	50	-	-	0.53	480
Uracil	1.70	70	-	-	0.16	2150
69^+ from uracil	1.28	90	-	-	0.21	3210

Table 4.1: Decay constants and their amplitudes for the ionic fragments shown in Figure 4.5.

Both the short and the long decay times differ significantly between the three molecules, as well as between the parent and fragment of the same molecule. The spread in picosecond decay times are shown in figure 4.8. Each of the panels of this figure shows a histogram of picosecond decay times of different fragments for all three molecules.

In uracil, the IP changes in going to the S_2 and S_1 minima by 1.5 and 2.5 eV, respectively, as can be seen in figure 4.4. Accordingly, the ion yields decrease

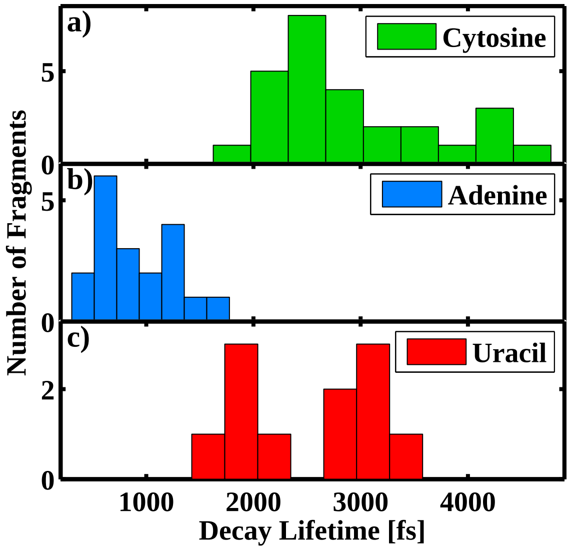

Figure 4.8: Histograms showing the spread of excited state lifetimes for cytosine, adenine and uracil.

steeply in moving away from the FC region, as evidenced by a sharp drop in both the parent and the fragment at 69 amu signals just after time zero. Uracil starts by a movement of the wavepacket from the FC region to either the S_2 minimum or directly to the S_1/S_2 CI. In the latter case, the switching from S_2 to S_1 leads to a change in the ionization pattern, as discussed in more detail in chapter 6. While S_2 is ionized primarily to D_0, S_1 ionizes mostly to D_1. The switching is consistent with the early delay at which the parent signal is maximum and a sharp drop (∼70 fs) of this ion signal. The pump-probe signal of mass 69 has a pronounced long (>10 ps) component, consistent with some of the excited state population being trapped S_1 minimum. The distribution of picosecond decay times is bimodal, with peaks at about 2 ps and about 3100 fs, as seen in 4.8c, offering support to a bifurcation on the initial excited state, and both CIs playing a role in the deexcitation.

As shown in figure 4.3, the calculated IP change in adenine, between the FC region and the L_b minimum is very small (~ 0.1 eV). The change between the FC and the $n\pi^*$ minimum is 0.5 eV. Both are much smaller than the change in IP in the initial stages of relaxation in uracil, and this difference is borne out in the fact that the time zero peak is less prominent in the adenine parent or many of its fragments, compared to uracil. However, there are fragments that exhibit a somewhat sharper time zero, for example CH_2N^+ (28 amu). This may indicate that the parent and some of the fragments are formed by ionization and subsequent fragmentation from the L_b minimum, while CH_2N^+ originates from the $n\pi^*$ minimum. In terms of the decay times for the picosecond component of decay, fitting resulted in a range of lifetimes. The lifetimes allow the rough grouping of fragments into two categories - one with lifetimes around 700 fs, and one with lifetimes around 1250 fs, as seen in Figure 4.8.

The relaxation of cytosine along two separate deexcitation pathways will be discussed in detail in the following section.

4.4 Distinguishing between pathways in cytosine

In this section, we follow the excited state dynamics of cytosine pumped to its first excited state. We focus on the picosecond timescale dynamics, which is associated with the excited state wavepacket being confined to a region close to a minimum on the excited state by a barrier that separates the minimum from a CI with the ground state. As we have argued in section 4.2, only keto cystosine, the tautomer most commonly found in DNA and RNA, contributes to the picosecond ion signal we measure. Here we first present the theoretical results on cytosine relaxation pathways, and then turn to measured pump-probe ionization signal to try and determine the relative importance of the two accessible pathways. We conclude with a picture of cytosine relaxation through multiple conical intersections.

Figure 4.2 shows the geometries that play a role in the excited state dynamics. The bright S_1 state is connected to the ground S_0 state through two energetically accessible CIs, labeled 'sofa' and 'twist' [113]. A third CI between S_1 and S_0 has also been found [29, 117] but studies that use correlated methods find this CI to be higher in energy [113, 118, 121], so it is not expected to play a role in the relaxation. Three-state CIs have also been identified in cytosine but their energies are higher than the two-state intersections mentioned above [123, 124]. It should be noted that the CIs discussed here are the minimum energy points on the seams of CIs. In a molecule with N degrees of freedom, these seams are N-2 dimensional hypersurfaces.

As shown in figure 4.2, initial absorption of a pump photon leads to the FC region of the excited state, which lies about 0.8 eV above the S_1 minimum, called the 'butterfly' minimum here. This minimum is separated from each of the CIs by at least one barrier. Only one barrier is separating this minimum from the twist CI, but there are two barriers towards the sofa CI, with the minimum closer to the sofa CI labeled as the sofa minimum. The size of barriers separating the sofa and the twist CIs from their respective minima are comparable and it is not easy to determine their relative importance in the radiationless decay based only on energetics.

In order to test whether both relaxation pathways are explored in the ultrafast relaxation of cytosine, we set out to identify fragments that can label the S_1 pathways predicted by theory. To begin with, we examine the overlaps between S_1 and low-lying ionic states. We base our analysis on the sensitivity of ionization to the IP, the dependence of the ionization rate on the position on the excited state PES from which the molecule is ionized, and the electronic configurations and orbitals of the neutral state.

Figure 4.9 shows the dominant orbitals describing the S_1 state at the three geometries of primary interest in our analysis: the initial FC geometry, the butterfly minimum, and the sofa minimum. At the S_0 minimum, as well as at the sofa minimum geometry, the S_1 configuration of cytosine corresponds to a HOMO → LUMO excitation, with a contribution of about 75%. At the butterfly minimum, the HOMO→LUMO contribution is about 50%, with the second highest contribution from HOMO-1→LUMO. The natural orbitals of D_0 and/or D_1, describing the hole left in the cation, are shown for these geometries in the rightmost column of figure 4.9.

The removal of the LUMO electron, leaving a hole in HOMO, would produce an ion in its ground D_0 state. Calculations show that the S_1 state significantly overlaps with D_0 at all geometries relevant for ultrafast relaxation. We therefore restrict our analysis to fragments that are produced from the ground D_0 state of the ion. This overlap can be visually checked by comparing the S_1 and D_0 the orbital shapes from the rightmost and the leftmost columns of figure 4.9. It can be quantified using the concept of the Dyson orbital defined in chapter 5.

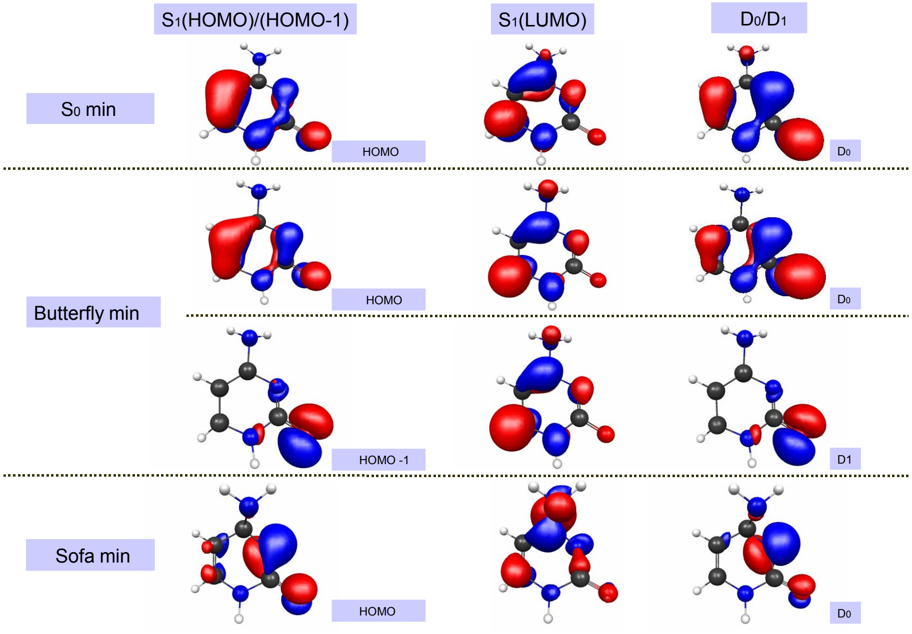

Figure 4.9: The HOMO/HOMO-1 (left column) and LUMO (middle column) orbitals of cytosine describing the S_1 state, as well as, natural orbitals describing the hole for D_0/D_1 (right column) calculated at the geometries S_0 min, butterfly min, and sofa min.

Considering that the parent ion originates from D_0, any other fragment that originates from the same state should have the same probe intensity dependence as the parent ion. Our analysis presented below reveals that the parent ion is produced predominantly at the butterfly minimum, making the parent a label for the butterfly pathway. The fragment $C_4N_2H_3O^+$ at 95 amu is found to have the same intensity dependence as the parent, but also to be produced mainly from the sofa minimum, making this fragment a label of the sofa minimum. The parent and mass 95 pump-probe signal show significantly different decay time constants of about 2200 fs for the parent and about 4300 fs for the 95 amu. The fitted decay times for pump-probe signals of all fragments of cytosine, presented in figure 4.8a and table 4.1 show a spread of picosecond decay times, confirming the delocalized relaxation picture.

Figure 4.10 shows the ratio of fragment to parent ion signals for fragments 43 and 95 at pump-probe delays of about 500 fs. This delay is long enough to exclude the cross-correlation between the pump and the probe pulses, but short enough that the wavepacket is still largely on S_1. Fragment at 43 amu, whose ratio to parent ion depends strongly on the probe intensity is shown to contrast the weak dependence of the 95 amu ratio to the parent ion.

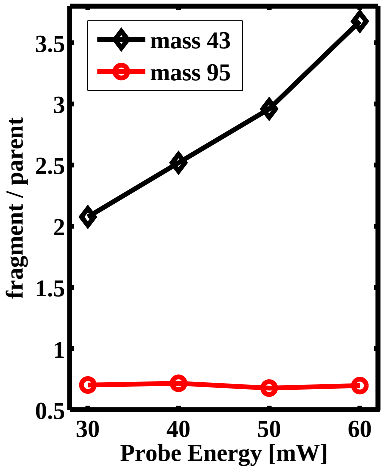

Figure 4.10: Probe intensity dependence of fragment signal divided by parent. Black line and diamonds represent the peak at 43 amu, and red line and circles the peak at 95 amu. Data shown for a pump probe delay of 500 fs

4.4.1 Fragmentation from the butterfly minimum

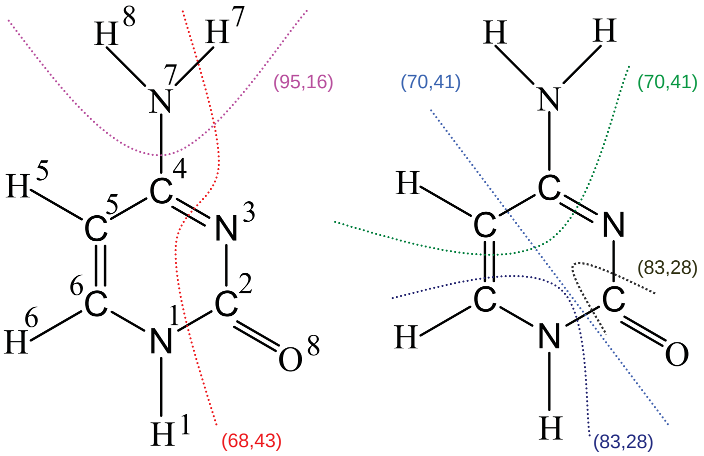

Figure 4.11: Picture of cytosine showing the atomic numbering convention used in the text along with bonds which are broken to form fragments discussed in the text.

In this subsection we discuss the choice of the parent ion as the label of the butterfly minimum n the S_1 surface in some detail. We first turn to a study of fragmentation patterns in the cytosine cation [140]. It was found that the first step towards producing fragments at 68 amu and at 83 amu, dominant in the mass spectrum, involve a common transition state TS_{ion}, and breaking of the N^1-C^2 bond (see figure 4.11). This transition state lies about 0.34 eV above the minimum of the ground ionic state in energy. Upon reaching TS_{ion}, additional steps can lead to the production of either 68^+ or 83^+. The lowest energy barrier on the ground state of the molecule, of 1.85 eV, is that to the production of 68^+, after breaking of an additional bond and accompanied by proton transfer. Therefore, a molecule with at least 1.85 eV of energy above the D_0 minimum will dissociate, while one with less than this minimum energy would not.

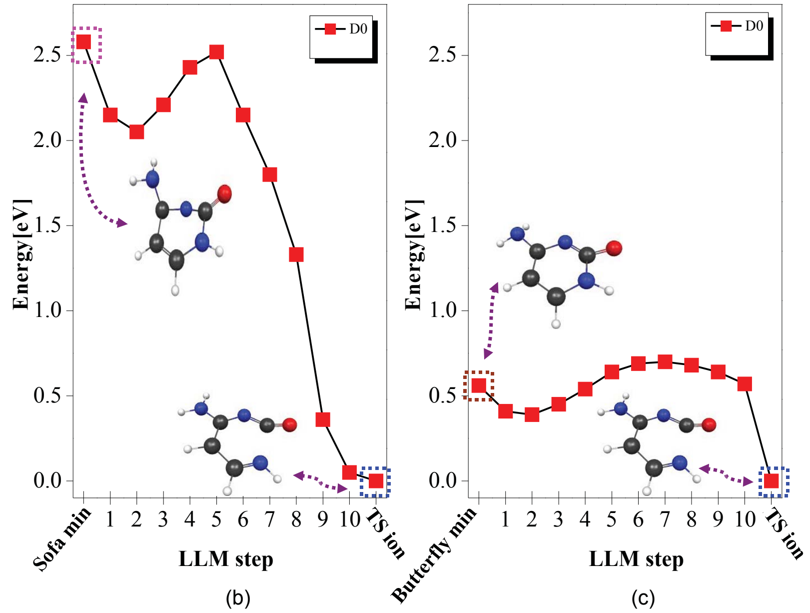

Figure 4.12: Calculated D_0 energies along the ionic LLM pathways starting at the sofa and the twist minimums and ending at the TS_{ion} point

Figure 4.12 shows ten-intermediate-step linear least motion (LLM) D_0 energy scans starting at the sofa minimum and the twist minimum and ending at the TS_{ion} geometry. The LLM scans are done by linearly interpolating the coordinates of a molecule between the start and the end point in a given number of steps. Since they include no geometry optimizations, they give the upper bound on the possible barriers existing between the start and the end point. In this case, no significant additional barriers were found on either of the pathways towards TS_{ion}. Importantly, the barriers that can be seen in figure 4.12 are not higher in energy than the initial point on each pathway. The barrier LLM calculation shows that the energy the molecule has upon reaching TS_{ion} is very different when ionized out of the sofa minimum than when ionized from the twist minimum. The D_0 energy at sofa minimum geometry is about 2.5 eV above TS_{ion}, while at the butterfly minimum the D_0 energy is only about 0.5 eV higher than TS_{ion}. Thus, the molecule does not have enough energy to dissociate from the sofa minimum, making the parent ion a marker of the butterfly pathway.

4.4.2 Fragmentation from the sofa minimum

In this subsection, we present arguments in favor of the 95^+ being a label of the sofa minimum. In order to produce this fragment, the C^4-N^7 bond need to be broken, corresponding to a loss of an NH_2 radical. Factors that lead to a weakening of this bond include pirimidalization, or placement of C^4 away from the plane of the molecule, because the amino group tends to π-overlap with C^4 when that carbon is planar, which strengthens the C^4-N^7 bond. Pyrimidalization of C^4 is very pronounced at the sofa minimum geometry, and the weakest in twist geometry. The orbitals shown in Figure 4.9 confirm that along the sofa direction, the density is localized on N^3 and there is no density along C^4-N^7.

These arguments have been confirmed by *ab initio* calculations. The calculated D_0 energies as a function of C^4-N^7 bond length, show that 3.9 eV of energy is needed for the cleavage of this bond from the sofa geometry compared to 5.6 eV for the butterfly minimum. These calculations did not include relaxation at intermediate geometries, and therefore overestimate the dissociation energy. They do provide a rough comparison of the energetic requirements between the two pathways. The C^4-N^7 cleavage energy from the D_0 minimum, obtained from a relaxed scan, is 2.6 eV. Finally, the D_0 energy is higher at the sofa minimum geometry than at the twist minimum geometry. Thus, energetic arguments indicate that 95^+ is indeed produced from the sofa minimum.

Additional support for the association of the 95^+ fragment with the sofa minimum comes from low energy electron impact ionization [141] and low energy photoionization with synchrotron radiation between 8.8 and 10.2 eV [142], which ionized ground state cytosine molecules to D_0 and D_1 (see figure 4.2), with a possible minor contribution from D_2), but produced a negligible signal at 95 amu, consistent with differences in orbital shapes that likely lead to differences in fragmentation patterns. As shown in figure 4.9, the natural orbitals for D_0 and D_1 (not shown) at the butterfly and S_0 minimum are very similar. This indicates that ionization to D_0 and D_1 from these two locations produces a similar fragmentation pattern, featuring the parent ion but not including 95^+.

4.4.3 Other fragments

The parent and 95 amu can be associated with ionization to the ground D_0 state of the ion, and with dissociation from a particular minimum on the excited state surface. However, they are rather an exception among the fragments in the mass spectrum of cytosine. In fact, many of the fragments we observe are either only produced from an excited state of the ion, or can be produced at several geometries. In addition, some of the fragments with the same mass are produced through breakage of different bonds, and therefore cannot be used to track a particular relaxation pathway. For example, the 43 amu fragment is predominantly produced from an excited state of the ion, as confirmed by figure 4.10. An example of a fragment that is produced from the D_0 state, but not exclusively at a given geometry, is the fragment at 68 amu. The presence of a peak at 68 amu in the low energy electron impact ionization spectrum [141] indicates that this fragment can be produced at the S_0 minimum and therefore likely at the butterfly minimum as well, given the similarity of the molecular orbitals at the two geometries. This fragment is expected to be produced from the sofa minimum as well, since breaking the N^1-C^2 bond (with barriers and energies shown in figure 4.12) constitutes the first step towards the production of 68 amu.

Below we examine the time dependence of the ion signal of several fragemtns of cytosine, despite the difficulties in isolating locations on S_1 which contribute uniquely to their production. The decay times and pathway association for several prominent fragments in the mass spectrum is given in table 4.2. The uncertainties listed are the standard deviation in fit values from repeated pump probe measurements on different days. Some fragments we associate with the

fragment	association	decay time (ps)	uncertainty (ps)
70 amu	twist	2.3	0.3
parent	twist	2.3	0.2
83 amu	sofa/twist	2.6	0.3
68 amu	sofa/twist	3.6	0.6
43 amu	sofa*	4.1	2
95 amu	sofa	4.3	0.5
41 amu	twist*	4.6	1.3

Table 4.2: Decay constants and associations. * labels fragments which come from excited states of the ion.

twist pathway based on changes in bond lengths in the neutral, exhibit a timescale of approximately 2.3 ps, which is close to (2300 ± 200) fs we previous obtained for the parent. Fragments associated with the sofa pathway, also based on bond lengths (95 amu, 68 amu and 43 amu) have timescales between 3 and 5 ps. The 95 amu fragment associated with the sofa pathway has a decay constant of (4.3 ± 0.5) fs. We observe a significant variation in the decay constants for different fragment ions. The middle panel of figure 4.8, shows the histogram of the picosecond decay times for significant fragments of cytosine. This spread indicates that the excited state wavepacket is delocalized, with portions of it relaxing to the ground state at different rates, via different pathways and giving rise to different fragments in the TOFMS. If the wave packet were localized, then yields of fragments that ionize to the same ionic state would decay at the same rate.

4.5 Conclusions

We show qualitative differences in the relaxation dynamics of the three molecules, as well as differences in the ion yields for different fragments from the same molecule. The differences between fragments of the same molecule indicate that the neutral dynamics of the molecule involve multiple pathways that can be taken, and a given fragment can be associated with only one of these routes. In cytosine, we have shown how a study of dissociation energetics, motivated by and consistent with a predicted fragmentation pattern based on neutral and ionic state overlaps, can give a detailed picture of relaxation dynamics that involves more than one pathway (shown in figure 4.13). In this picture, the molecule is excited from the S_0 minimum to the FC point on S_1, where it begins to evolve towards a local minimum on S_1. The wave packet becomes delocalized and explores many pathways on the S1 surface. Its de-excitation back to the ground state proceeds through at least two pathways that are traversed in parallel. The timescales shown in the figure reflect the fitted decay times for the fast (~100 fs) and the picosecond component of the pump-probe signal.

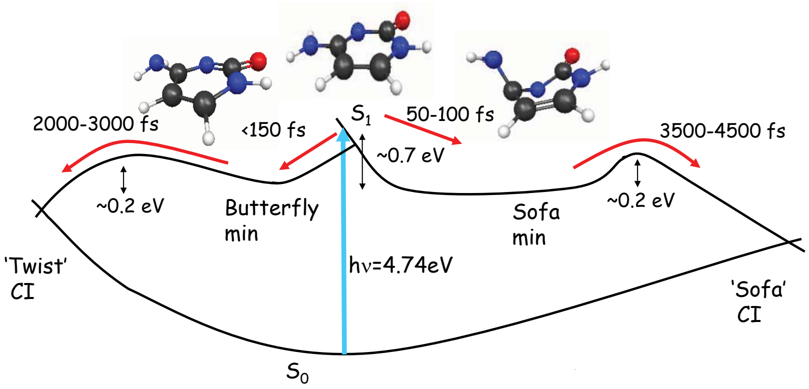

Figure 4.13: Cartoon of S_0 and S_1 PES showing important points and timescales extracted from experimental fittings.

Chapter 5

Strong field molecular ionization from multiple orbitals

5.1 Introduction

In this chapter, we study the properties of strong-field ionization from multiple orbitals of a polyatomic molecule. We examine the dependence of strong-field ionization yields on the orientation of excited state with respect to the ionizing laser field. We chose to use excited state uracil, because it has a bright state whose excitation energy is close to the energy of our UV pulses. Furthermore, theoretical results, previously obtained by our collaborators, enable the identification of the orbital from which an electron has been removed in the ionization process for a given final product of dissociation from an ionic state. The non-trivial electronic configuration, along with their being partially aligned using a simple procedure, makes excited state uracil molecules a suitable system for studying the ionization from multiple orbitals and its angular dependence.

The molecules are excited to the first bright (S_2) excited state of the neutral by a near-resonant pump. The ensemble of excited state molecules is partially aligned by the pump pulse in a process of selective excitation (which will be described in section 5.3) and subsequently ionized and dissociated by a strong-field IR probe. The time delay between the pump and the probe pulses is varied, as well as their relative polarization. We measure the ion yields of the resulting fragments as a function of the time delay and relative polarization angle. The results are interpreted using *ab initio* electronic structure calculations, performed by Congyi Zhou and Spiridoula Matsika at Temple University. We find that a prediction, based on the orbital nodal structure, for the angle-dependent distribution of ion yields matches our observation for the ionization of a LUMO (lowest unoccupied molecular orbital) electron, whereas ionization from deeper bound orbitals is more complicated.

In this chapter, we first give a brief description of our experimental approach, followed by a presentation of the experimental and theoretical results, and a discussion of the interpretion of the data. A separate section deals with multielectron wavefunctions and concept of the Dyson orbitals. Another section provides some details about the rotational dephasing of a partially aligned sample of molecules, a process that can obscure the temporal dynamics we observe. We then present and discuss our results, and end with a few concluding remarks.

The dependence of strong field ionization yields on the orientation of the laser field with respect to the molecule is still an open question. In the case of ionization of small, ground state molecules, it has been shown that the yields reflect the shape of the molecular orbital from which the electron had been removed [143–146]. In the case of a single photon ionization, or recombination leading to harmonic emission, it has been shown that the angular dependence reflects the structure of the Dyson orbital (see section 5.2) associated with the ionization [45]. It has been predicted [147] that the ionization yields will be suppressed if the laser polarization vector lies in a nodal plane of an orbital, since the contributions to the outgoing electron wave from electron density lobes of opposite phases will interfere destructively. Thus the angular dependence of the ionization yields reflects the nodal structure of the orbital, which is in turn intimately related to the symmetry of that orbital. This idea has been used to follow dissociation dynamics in a diatomic molecule [148]. In addition to orbital symmetries, Bucksbaum et al. [149] considered the spatial extents of orbitals in N_2, to identify contributions to the harmonic spectrum from electrons expunged from both HOMO and HOMO-1 orbitals of this molecule.

In our experiments, the molecules are first pumped by a near-resonant pulse in the deep ultraviolet at about 262 nm. The pumping enables the angle-resolved measurements to be performed in the lab frame by partially aligning

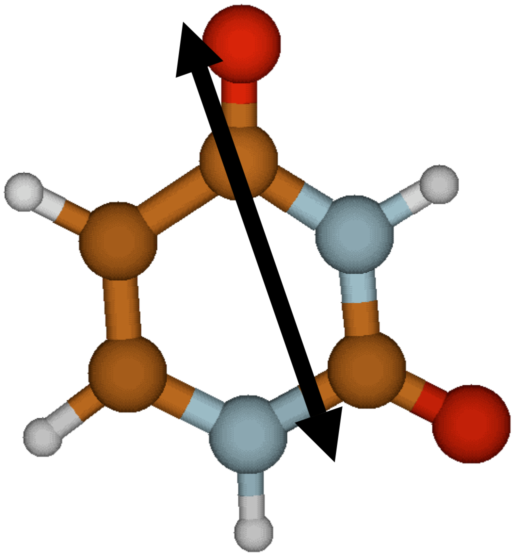

Figure 5.1: Geometry of ground state uracil and transition dipole moment for the $S_0 \rightarrow S_2$ electronic transition.

them. After a variable delay, the molecules are ionized by strong-field, near-IR pulses at about 780 nm. The molecules may undergo dissociation following ionization, depending on what final state the molecules is left in following ionization. A half-waveplate placed in the pump beam allows us to change this beam's polarization, and we detect mass-resolved ion yields as a function of the delay between the pump and the probe and the angle between their polarization vectors.

We interpret the data with the aid of *ab initio* electronic structure calculations. They are used to obtain energies and electronic configurations of the the neutral S_0 and S_2 states involved in the excitation and initial relaxation from the Frank-Condon region of the excited state as well as configurations, energies and energetic requirements for dissociation from accessible ionic states. Our calculations allow us to associate fragments in the TOFMS with final states of the cation, and to establish relations between neutral and ionic electron configurations.

5.2 Multielectron wavefunctions and Dyson orbitals

In order to describe a multi-electron molecular wavefunction, it is convenient to start from one-electron states or orbitals. The orbitals are filled with electrons in order of increasing energy, in accordance with the aufbau principle. A ground state of a neutral molecule with an even number of N electrons corresponds to the N/2 energetically lowest one-electron states (orbitals) doubly occupied by two electrons of opposite spin projections, and all the higher lying orbitals unoccupied. Acronyms HOMO and LUMO are commonly used for the highest occupied molecular orbital and lowest unoccupied molecular orbital, as well as their extensions HOMO-1, HOMO-2 etc. A wavefunction correctly accounting for exchange interaction between electrons and describing an N-electron state is a Slater determinant, obtained by fully antisymmetrizing a product of N one-electron functions. Only occupied orbitals are included in the product, and this distribution of electrons over orbitals is referred to as the electronic configuration. An eigenstate of the molecular Hamiltonian is in many cases a linear combination of several configurations. In the case of low-lying singlet (neutral) excited states, the dominant configuration often corresponds to moving an electron from the HOMO to the LUMO orbital. In the case of ionic states, the lowest ones are dominated by configurations including only one singly occupied orbital, usually HOMO, HOMO-1, etc. In this chapter, we use the HOMO/LUMO notation rather than symmetry assignments as it offers an unambiguous way of referring to different orbitals and states.

Projecting a final (N-1 electron) ionic state onto the initial (N electron) state of the neutral yields a Dyson orbital of the ionization channel: $\psi_{Dyson} = \sqrt{N}\langle\psi_m^N(r_1, r_2, ..., r_N)|\psi_n^{N-1}(r_1, ..., r_{N-1})\rangle$, where ψ_m^N and ψ_n^{N-1} are the eigenfunctions of the neutral and the ionic Hamiltonians. The magnitude of a Dyson orbital is formally related to the ionization yield to a specific state in the case of single photon, or more generally, ionization that can be described perturbatively [150]. In the case of strong-field ionization, the situation is more complicated, and this will be the subject of chapter 6.

5.3 Alignment through selective excitation and rotational dephasing

Prior to their interacting with the pump pulse, the uracil molecules in the interaction region of the vacuum chamber are randomly oriented. They are in the ground electronic state, S_0, though thermal excitations may place them in a higher vibrational or rotational state. If the pump pulse is nearly resonant with a transition (e.g. $S_0 \to S_2$ in uracil), it preferentially excites this transition in molecules whose transition dipole moment (TDM) is aligned along the laser polarization vector. In general, the probability of a molecule being excited is proportional to the cosine square of the angle θ between the TDM associated with the excitation and the laser polarization vector. This leads to a degree of alignment of ensemble of the excited state molecules. The figure of merit describing the degree of alignment is commonly given as the expectation value of square of the cosine of the angle θ between the molecular axis and the polarization vector of the laser.

$$\langle cos^2(\theta)\rangle = \int_0^{2\pi} d\phi \int_0^{\pi} cos^2(\theta) f(\theta) d\theta, \tag{5.1}$$

where $f(\theta)$ is the distribution of alignments of individual molecules. For comparison, for a perfectly aligned sample, $\langle cos^2(\theta)\rangle = 1$, while for a completely dephased sample in three dimensions $f(\theta) = 1/(4\pi)$ making $\langle cos^2(\theta)\rangle$ equal to 0.33. For molecules that have been aligned by selective excitation, the sample has a cosine square alignment distribution $f(\theta) = (3/(4\pi))cos^2(\theta)$ and the measure of the alignment quality factor $\langle cos^2(\theta)\rangle$ is 0.6. Factors of $1/(4\pi)$ and $3/(4\pi)$ ensure the proper normalization of each distribution function. An analogous alignment measure can be defined for samples constrained to one degree of freedom, where perfect alignment again corresponds to $\langle cos^2(\theta)\rangle = 1$, but the alignment factor becomes 0.5 for a completely random sample, and 0.75 for a sample with a cosine square alignment distribution around an axis.

The selective excitation scheme does not lead to a three-dimensional alignment of the molecules, since they are not constrained along one of their degrees of freedom. Instead, the partially aligned sample consists of molecules free to rotate around their TDM vector. The partially aligned sample contains molecules of two opposite orientations of the TDM with respect to the laser polarization vector at a given moment. The TDM for the $S_0 \rightarrow S_2$ transition in uracil is shown in Figure 5.1. Others have used this simple partial alignment scheme [148]. It should be noted that this alignment scheme is only effective for pump pulse intensities that do not saturate the relevant transition, and for this reason care has been taken to run the experiments at sufficiently low UV intensities.

Another commonly used alignment scheme is the dynamical alignment using a strong non-resonant laser pulse to transiently align a molecule. In rotationally cold molecules, an ultrafast laser pulse can prepare a coherent superposition of rotational states that are aligned a short time after the pulse. The system dephases with a rate proportional to the square of the width of the rotational wavepacket in the J space [151]. Since the rotational frequencies scale as J(J+1), the system can rephase, and subsequently dephases are rephases with a period proportional to the difference in energies between the J=0 and J=1 or J=2 states, depending on symmetry. The non-resonant dynamical alignment scheme is more difficult to implement experimentally than alignment through selective excitation. It requires the molecular sample to be rotationally cold, typically to 10 K or less. In the simplest implementation of this scheme, the laser field is linearly polarized, and the molecules are free to rotate around the polarization vector of the field. The field-free alignment quality factors achieved for polyatomic molecules typically reach about 0.55-0.6 in one-pulse experiments [152] and up to 0.7 in more sophisticated experiments utilizing two laser pulses [153]. The highest degree of alignment reported in any experiment to date is 0.92, achieved for iodobenzene cooled to about 1 K [154], in an adiabatic (non-field-free) alignment scheme.

In order to determine the dephasing time, or the approximate time during which a sample of molecules remains aligned to some degree after its interaction with the pump pulse, we calculate the beat period between to eigenstates of the rotational Hamiltonian. It should be noted that the dephasing corresponds to rotations around one of the axes perpendicular to the TDM of the molecules, since our sample is free to rotate around the TDM itself. We calculate the rotational energies of a molecule as those corresponding to a quantized rigid rotor. The distribution of population across rotational states, is given by the thermal Boltzman distribution. Population in excited vibrational states is neglected here, even though the low-frequency vibrational states of uracil were likely populated at the operational temperatures of about 130^{o}C.

The energies of rotational states of a molecule, E$_{rot}$ is given by:

$$E_{rot}(J) = \frac{J(J+1)\hbar^2}{2I} \tag{5.2}$$

where the rotational quantum number J takes on non-negative integer values, J=0,1,2,..., I is the moment of inertia of the molecule, and $\hbar$ is the reduced Planck's constant. The degeneracy of each of the rotational states is given by 2J+1. For a sample of molecules at a finite temperature, the population in each of the rotational states is:

$$p(J) = \frac{(2J+1)e^{E_{rot}(J)/k_BT}}{\sum_J (2J+1)e^{E_{rot}(J)/k_BT}} \tag{5.3}$$

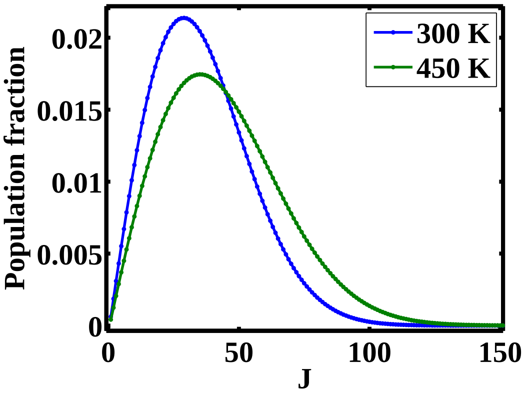

Figure 5.2: Population of rotational levels as a function of the rotational quantum number, for uracil molecules at 300 K and at 450 K

The distribution of rotational population over rotational states is shown in figure 5.2, for uracil molecules rotating around the axis perpendicular to TDM for the S$_0$ →S$_2$ transition with a smaller associated moment of inertia (or for a linear molecule with the moment of inertia equal to the smallest one for uracil), at room temperature (300 K) and at the temperature close to those at which our experiments have been conducted (450 K). Both temperatures were included to emphasize the weak dependence of rotational dephasing on the sample temperature, in the range of temperatures that were relevant to our experiment. Therefore, a possible cooling of the molecular beam during

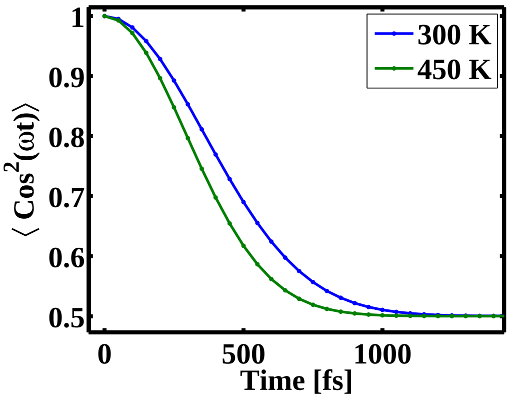

Figure 5.3: Rotational dephasing of uracil molecules at 300 K and at 450 K.

its expansion into ultrahigh vacuum is not expected to add significantly to the dephasing time.

We obtained an angular velocity, ω, by equating the rotational energy, E$_{rot}$, from equation 5.2, with the expression $E_{rot} = I\omega^2/2$. Then, assuming that all the molecules in the sample are aligned initially, we can evaluate the dependence of the alignment quality factor on time, t.

$$\langle cos^2(\omega t)\rangle = \frac{\sum_J (2J+1)cos^2(\sqrt{J(J+1)}\hbar t/I)e^{-E_{rot}/k_BT}}{\sum_J (2J+1)e^{-E_{rot}/k_BT}} \qquad (5.4)$$

This expectation value is a measure of the degree of alignment as a function of time of a sample of molecules that are free to rotate around one axis only, so it varies between 0.5 and 1.

5.4 Results

In this section, we describe the results of angle resolved pump-probe measurements. Figure 5.4 shows TOFMS of uracil at positive and negative pump probe delays. At negative delays, the probe pulse interacts with the molecules prior to the pump pulse, and effectively ionizes them from the ground neutral state, with the pump adding little to the ionization signal due to its low intensity. The sample of ground state molecules, probed before the pump had interacted with them, i.e. at negative pump-probe delays, is randomly aligned. The ionic states reached at probe intensities below saturation are mostly the low lying ones (D$_0$, D$_1$...) with configurations dominated by removal of an

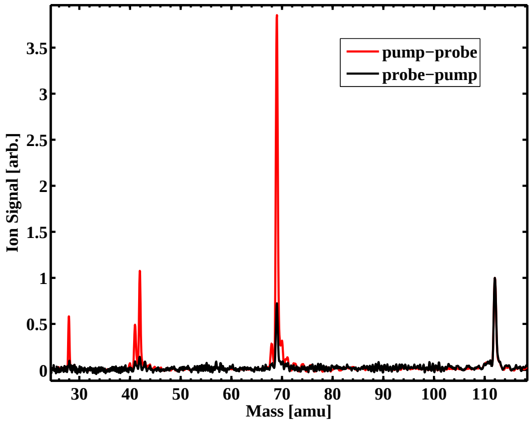

Figure 5.4: Time of flight mass spectra of uracil for negative and positive time delays (+/- 200 fs). Both spectra are normalized to the parent ion yield.

electron from a high-lying, weakly bound orbital, such as HOMO or HOMO-1 [155]. *Ab initio* calculations show that the first two states of the cation are not dissociative at the FC geometry, while the next few should lead mostly to the mass 69 fragment. Our measurements for negative pump-probe delays show that the parent ion and 69 amu dominate the TOFMS, confirming the prediction. For IR intensities even lower than that used for the measurements shown in figure 5.4 the TOFMS shows no ions other than the parent ion, consistent with ionization leading to the two lowest ionic states, D_0 and D_1.

At positive time delays, the molecule is excited to the first bright S_2 state prior to ionization by the probe. Consequently the total ionization yield increases significantly, as the IP is reduced by the $S_0 \rightarrow S_2$ energy (about 4.74 eV). This is not reflected in figure 5.4, where the ion yields are normalized to the parent ion signal both for positive and negative time delays. However, the top panel of figure 5.5 shows the total ion yield increase for positive time delays. In addition, dissociative ionization leads to an increase in the production of smaller fragments - most notably 28 (H_2CN^+), 41 ($H_3C_2N^+$), and 42 amu ($H_2C_2O^+$), as compared to the parent ion. Below we discuss the dissociation channels that can be reached from by a uracil molecule ionized to different states of the ion, and the angular dependencies of the resulting ionic signals.

The time and angle dependent yields of 28, 41 and 42 are shown in figure 5.5. The angle and time dependence of the yields for 28, 41 and 42 are very similar, although they are distinct from the yields for other fragments such as

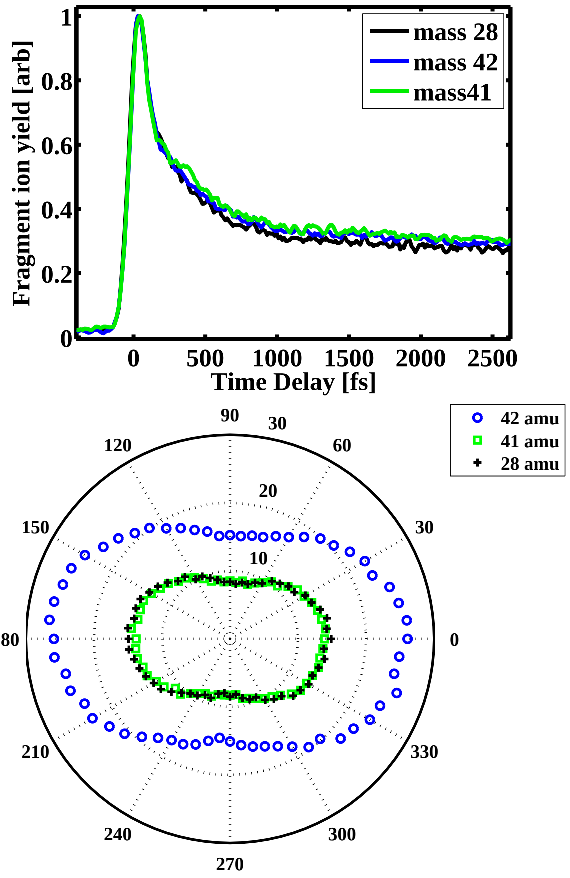

Figure 5.5: Top panel: pump probe signals from 42, 41 and 28 amu fragments. The signal for each fragment is normalized. Bottom panel: pump-probe ion yield vs pump polarization at 200 fs pump-probe delay. The azimuth angle corresponds to relative polarization between the pump and the probe beams, while the radial distance is the ion count in arbitrary units.

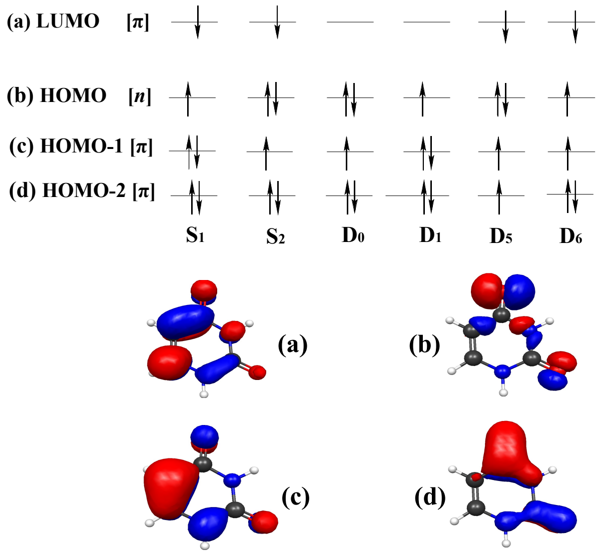

Figure 5.6: Dominant electronic configuration and characters for relevant states of the neutral and the ion. The participating orbitals are shown as well: (a) LUMO, (b) HOMO, (c) HOMO-1 and (d) HOMO-2. The orbitals are shown for the molecule in the same orientation as shown in figure 5.1.

the parent and 69. This leads us to conclude that these three fragments are produced from the same ionic state or states.

The top panel of figure 6.2 shows the configurations for the electronic states relevant to the discussion in this chapter. The bottom panel of figure 6.2 shows the shapes of the orbitals that participate in the configurations of the relevant electronic states. Dominant cofigurations are shown for each one of the states. For the ground neutral state, the dominant configuration is the one with all the electrons paired and the orbitals filled in order of increasing energy. Excitation to S_2 can be described as a HOMO-1 → LUMO excitation.

Figures 5.7 and 5.8 show the angle- and time- resolved ion yields for the parent ion and fragment at 42 amu at several pump-probe delays. Angles of 0^o and 180^o correspond to parallel relative polarization between the pump and the probe beams, while 90^o and 270^o correspond to perpendicular relative polarization between the two beams. Experiments carried out with the probe polarization along the TOFMS axis and perpendicular to it yielded the same dependence on the relative polarization between the pump and probe. About 20 polarization scans were taken in succession and averaged in order to improve the signal to noise ratio. The ion yield at each angle in the 0^o-360^o range was

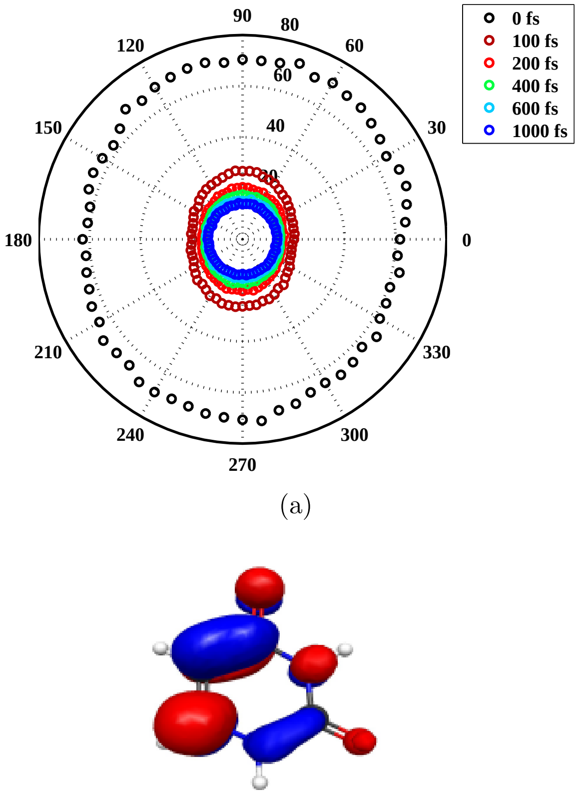

(a)

(b)

Figure 5.7: Panel (a): Pump-probe ion yield vs pump polarization and pump-probe delay for parent ion. The azimuth angle corresponds to relative polarization between the pump and the probe beams (0^o corresponds to parallel polarization). The radial distance is proportional to the ion yield in arbitrary units. Panel (b): LUMO orbital shape.

measured independently.

5.5 Discussion

We use calculated dissociation energies and barriers to dissociation on the ground cationic state to determine which cationic state(s) of the molecule are dissociative and can lead to which fragments. The use of ground state dissociation barrier is justified by a reasoning based on Kasha's rule. This rule was proposed for neutral molecules and states that even if highly excited states are accessed, fluorescence will often originate from the first excited state after a fast radiationless relaxation to it [156]. Such behavior is expected, since the

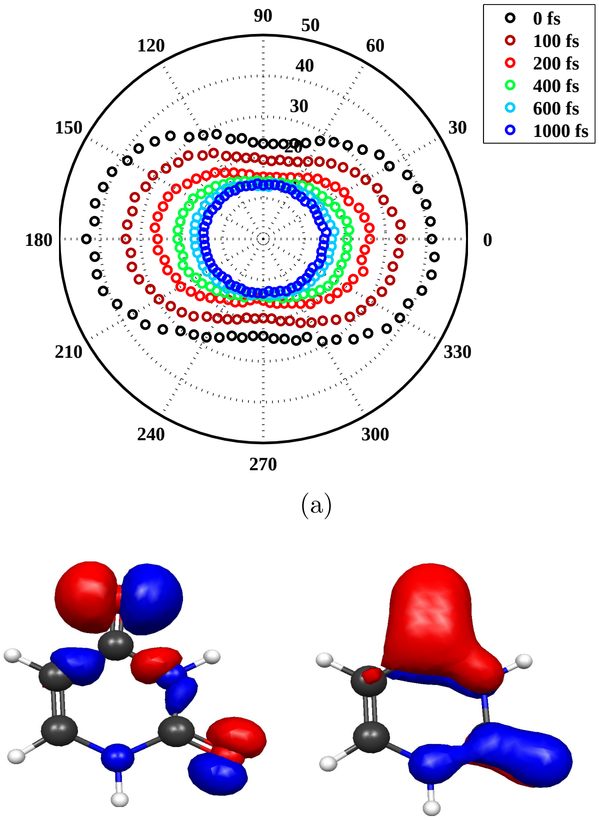

(a)

(b) (c)

Figure 5.8: Panel (a): Pump-probe ion yield vs pump polarization and pump-probe delay for 42 amu. The azimuth angle corresponds to relative polarization between the pump and the probe beams (0^o corresponds to parallel polarization). The radial distance is proportional to the ion yield in arbitrary units. Panel (b): HOMO orbital shape. Panel (c): HOMO-2 orbital shape.

density of states generally increases with their energy, and so do the chances for the existence of an easily accessible non-radiative relaxation pathway, i.e. a conical intersection. This rule can be extended to ionic states, whose density increases with energy as well. In uracil, the calculated D_0 dissociation energies are comparable with the difference in energy between the ground and the excited ionic states, making a dissociation from the excited state energetically unfavorable. Thus a molecule ionized to a higher ionic state will tend to undergo a rapid radiationless decay to D_0. The decay will convert electronic energy to vibrational energy on D_0 and dissociation will proceed from the vibrationally hot D_0 potential energy surface. Furthermore, parallel experiments that have been carried out on other molecules with a velocity map imaging apparatus show that ionization to excited states of the ion is predominantly followed by dissociation on the ground state of the cation, where fragments are ejected with the maximum possible kinetic energy [157].

According to calculations, D_0 and D_1 are not dissociative at the Franck Condon (FC) point geometry, so ionization to them leads only to the parent ion. The next several states, D_2-D_4 lie over 2 eV above the D_0 minimum, and according to calculations [158] have enough energy to dissociate to produce the $C_3NOH_3^+$ fragment (at 69 amu), as they lie higher in energy than the height of ground state barrier to producing the fragment at 69 amu. Figure 6.3 (from chapter 6) shows the energetic requirements for the production of some of the prominent fragments in the TOFMS.

As we worked at the lowest IR intensity where there was a sufficient signal to noise for the prominent fragments in the TOFMS, we argue that the fragment ion yields are dominated by the lowest ionic state which can dissociate to form them. In the case of uracil, calculations [32, 158] of the energies of the first few excited ionic states at the Frank-Condon geometry give values of 0.44, 0.98, 1.40, 3.01, 4.01, and 4.18 eV above the D_0 minimum for the D_1, D_2, D_3, D_4, D_5, and D_6 states, respectively. As discussed above, we use calculated ground state barriers to associate molecular fragments to low-lying ionic states. The barrier for creating fragments 28, 41, 42 is 3 eV [158]. It is in agreement with measured appearance energies [159], indicating that the lowest ionic state that can dissociate to produce these is D_5. In addition, the variation in yields of these three fragments with time and angle are not sensitive to the IR laser intensity around the value for the measurements in figure 5.5, so we consider both D_5 and D_6 as possible sources of these fragments since they are nearly degenerate and have electron configurations which correspond to removing an electron from a single orbital when ionizing the molecule that is initially in the S_2 state.

The S_2 configuration corresponds to the transfer of an electron from the HOMO-1 to the LUMO orbital, leaving an unpaired electron in each of these orbitals, as shown in figure 6.2. In uracil, the Dyson orbitals for ionization of S_2 to the ionic states of interest have very high overlaps with individual molecular orbitals of the neutral molecule - i.e. removal of an electron from a single orbital leads to a single predominant ionic state. It is of interest for this discussion that this is in particular true for D_0, D_5, and D_6, the three orbitals we focus on here. A removal of the LUMO electron from S_2 leads to a state with a hole in HOMO-1, which correlates well with the ground state of the ion, D_0. A removal of a HOMO or HOMO-2 electrons from the S_2 configuration leads to ionic states, D_5 or D_6, respectively, each with unpaired electrons in three different orbitals. This allows the association of an ionization channel with the removal of a single electron.

Dyson orbital magnitude is a good measure of an individual final state ionization yield only in the case of a weak-field excitation. In the case of strong-field excitation, it is in principle possible that there are contributions to the total ionization signal from other ionic states. For example, ionization could project S_2 to D_1 even though the magnitude of the Dyson orbital corresponding to this ionization channel is small. However, the largest contribution to the the parent signal will come from D_0.

The ionization angular dependence is expected to be influenced by the shape of the orbital from which an electron is removed to make a product observed in the mass spectrum. Since the largest contribution to the parent signal will come from D_0, based on configurations we expect that any angular dependence of the ionization yields will be given by the weakly bound LUMO orbital, given the low probe intensities we used and the lack of intensity dependence for the angle resolved parent ion yields. In the case of lighter fragments at 28, 41 and 42 amu, their ionization is predicted to be predominantly from the more deeply bound HOMO and HOMO-2 orbitals.

Figure 5.7a shows the dependence of the parent ion signal on the relative polarization between the pump and the probe beams. Since the uracil LUMO orbital, shown in figure 5.7b, is π-like, its major nodal plane is in the plane of the molecule. The orbital has contributions from electron density on either side of the molecular plane. Measurements of ionization of the most weakly bound electron in diatomic and linear triatomic molecules [143–145] has shown a suppression of ionization in the nodal plane.

The expected suppression of ionization in the nodal plane, translates to an prediction in terms of relative polarizations of the pump and the probe beams by noting that the TDM for the $S_0 \rightarrow S_2$ transition lies in the plane of the molecules, which is also the π nodal plane of the LUMO orbital. When the pump and the probe beams' polarization vectors are parallel, ionization of LUMO is suppressed since the probe polarization vector lies in the nodal plane of this orbital. When the pump and the probe polarization vectors are perpendicular to each other, we have to take the fact that the alignment is only constrained to one degree of freedom into account. The molecules are free to rotate around the S_0 $\rightarrow S_2$ TDM, and, in the molecular frame, the polarization vector can lie anywhere in the plane perpendicular to it. Since the plane perpendicular to the TDM intersects the nodal plane on the LUMO orbital, the ionization yield is suppressed for a part of the molecules that interact with the probe. However, some of the molecules will be aligned with the probe polarization perpendicular to their nodal plane, and their ionization will not be suppressed. Since ionization of the LUMO will be suppressed for all molecular orientations when the pump and the probe are parallel, we expect a net more suppression for this configuration. Our measurements (see figure 5.7a)agree with the prediction that ionization of the LUMO, producing the parent ion, is suppressed along the plane of the molecule (0^o and 180^o) relative to the direction perpendicular to the plane of the molecule (90^o and 270^o).

In the case of 28, 41 and 42 amu, there are two orbitals whose ionization leads to the production of these fragments the HOMO and the HOMO-2. this is because these fragments are expected when ionization leads to the higher ionic states D_5 and D_6, whose configuration in turn correspond a removal of an electron the HOMO or the HOMO-2 orbital, starting from the S_2 configuration.

In the case that these fragments arise from removal of a HOMO electron, associated with the D_6 ionic state, the nodal plane of the main lobe of this orbital contains the S_0-S_2 TDM. In this case one would expect suppression of the ionization parallel to the TDM, for reasons similar those outlined for the LUMO orbital above. In the case of ionization of an electron from HOMO-2, associated with the D_5 state, the principal nodal plane is clearly parallel to the TDM. There is a second nodal plane for HOMO-2, which is perpendicular to the TDM. Suppression in this second nodal plane could contribute to the favoring of ionization parallel to the TDM, although it is not clear why the suppression in the second nodal plane should be stronger than in the primary one parallel to the TDM. Thus, it seems that the observed ionization from

HOMO or HOMO-2 does not lend itself to a simple explanation in terms of the symmetry of the orbitals.

The limited contrast between the ionization yields for perpendicular and parallel polarizations, and the lack of detailed structure are a result of several limitations in our measurements. These include the fact that while the molecules are preferentially excited with their TDMs along the pump polarization vector, this only constrains the molecule along one angle, and does not result in three dimensional alignment [160]. Furthermore, the measurement is proportional to a convolution of the actual ionization probability vs angle with the distribution of molecules vs angle [143]. Finally, there is rotational dephasing leading to random molecular alignment on a timescale of about 1 ps for our molecular ensemble at $\sim 130°$C. This is consistent with the dephasing time for uracil derived in 5.3, and shown in figure 5.3.

A 'net' ionization of a particular orbital can be interpreted in several ways. For example, the ionization of an electron in a HOMO orbital can be accomplished through the direct removal of a HOMO electron, or indirectly, through the removal of a lower lying electron followed by a relaxation of a HOMO electron to take its place. Another way to describe this in a multi-electron picture is in terms of relaxation from a higher lying ionic state to lower ones. This relaxation, or coupling between ionic states can be due to field free terms of the molecular Hamiltonian (e.g. via a conical intersection between ionic states, or through interaction with the ionized electron, see chapter VI), or it may be driven by the laser field during ionization, particularly if the spacing between states is close to the laser frequency - i.e. near resonant interaction [161]. We argue that fragment ions, which can be produced by ionization of an electron from a given molecular orbital with multiple contributions should not necessarily have angular distributions reflecting the shape or symmetry of the orbital in which a new hole had been created at the end of the interaction, since there can be multiple contributions to the production of a given molecular orbital hole. However, the parent ion should still have the angular distribution dictated by the LUMO orbital, since the removal of a LUMO electron from the S_2 configuration is not only the most probable process, but also one that can occur without any configuration changes. Ionization of a LUMO electron from S_2 leading to D_0 is not expected to have contributions from several configurations which can complicate the angular distribution, because the final cationic state is D_0, from which no relaxation in the ion is possible as it is the lowest energy state. Furthermore, any laser driven coupling between ionic states would result in the molecule being left in a dissociative excited ionic state, and therefore not lead to parent ion production which is associated with the LUMO orbital.

In terms of timescales, it should be noted that it follows from the uncertainty principle that the movement of the hole between orbitals separated by up to 1 eV, (e.g. HOMO and HOMO-1 in uracil) takes 4 fs or more. Given the sensitivity of tunnel ionization to the laser field strength, ionization is confined to a very short ($\sim$ 100 as) interval in the vicinity of the sub-cycle field maxima. Since the uncertainty principle precludes the hole movement from occurring during a single cycle of the pulse, if hole motion is responsible for the anomalous angle dependent yield, then we must be able to see it by virtue of the ionization taking place over multiple cycles of the pulse. For the hole movement, i.e. evolution to occur following ionization by a few-cycle pulse the ionic state that is prepared would have to be a superposition of different electronic states, i.e. an electronic wavepacket.

5.6 Conclusions

Our measurements confirm that the ionization of the most weakly bound electron in a molecule to produce the parent ion is dictated by the shape of the orbital from which that electron is removed, but the ionization of electrons from more deeply bound electrons can be complicated by configuration changes during ionization, which can involve multiple orbitals in the ionization process. Configuration changes accompanying the ionization of the most weakly bound electron are not energetically allowed, whereas such changes are energetically favorable in the case of ionizing more deeply bound electrons. Therefore we expect that electronic correlation plays a more significant role in the removal of a HOMO or deeper bound electron then it does in a removal of an electron from LUMO or above. This is consistent with our measurement of the parent ion angular distribution following the symmetry of the LUMO, whereas fragments resulting from the removal of more deeply bound electrons do not simply follow the symmetry of the associated orbital.

Chapter 6

Role of state correlations in strong field molecular ionization

6.1 Introduction

In this chapter, we study of the role of correlations between the neutral and the ionic states in predicting the final state distribution in strong-field molecular ionization. The final-state resolved ionization yields presented here were calculated by Michael Spanner and Serguei Patchovskii of the Steacie Institute for Molecular Sciences at the National Research Council of Canada. The ab initio electronic structure calculations used as input for the strong-field ionization calculations were performed by Congyi Zhou and prof. Spiridoula Matsika of Temple University.

Strong-field molecular ionization is known to depend on the structure and electron density of a molecule [144, 148]. It is also sensitive to, and can therefore serve as a probe of, electron correlation [162, 163]. Introducing multi-electron effects has been shown to be necessary in describing features of the ionization of small molecules [164]. These effects are expected to be even more important in larger molecules, where the density of ionic states is higher, making ionization from deeper lying orbitals easier [145].

In this chapter, we focus on the distribution of final states in the process of strong-field ionization from a particular neutral state and on the role of correlations between the initial neutral and the final ionic states. Excited states of the ion generally have configurations that include a hole in an orbital below the highest occupied one (HOMO). This suggests that the removal of an electron from an orbital lying below the HOMO can be a dominant pathway to reaching an excited ionic state. Indeed, removing electrons from orbitals below the highest one in energy has been observed in strong-field ionization [30, 149, 165] and attributed to differences in the spatial electron density distribution between the orbitals. However, there has to date been no general way of predicting which states of the ion are populated by strong-field ionization, and with which probability.

Here we compare three methods for predicting final state ionization yields. The first method utilizes Dyson orbital amplitudes weighted by tunneling exponents [12], and can formally be derived from the strong field approximation. It is referred to as the Dyson-Keldysh method here. The second method is the molecular ADK (MO-ADK) theory [26]. The third method is the numerical calculations based on a time-dependent mixed orbital/grid-based method described in Ref. [164] and briefly in section 6.3. We find that accounting for multielectron effects, specifically the interaction of the departing electron with the core leading to rearrangement of core electrons during the ionization process, is necessary in order to achieve a qualitative agreement between the predictions and the measured ionization yields.

Ultrafast relaxation pathways of uracil are taken from previous studies [32, 112]. Briefly, a near-resonant sub-50 fs UV pulse launches a wave packet on the S_2 state, subsequent relaxation takes the wavepacket to the S_1 excited state in several tens of femtoseconds, and back down to the ground S_0 on a timescale of several picoseconds.

6.2 Correlations between molecular states

Koopmans' correlations, used in several recent studies [148, 166, 167], are a simple way of predicting the final state of an ionization process. A ground state is correlated with a cationic state corresponding to a single ionization in the Koopmans sense if the configuration resulting from the removal of a single electron from the neutral is identical to the configuration of the ion. Koopmans' correlations are based on the Hartree-Fock theory, where only one electronic configuration is considered for each of the neutral or ionic states involved. The validity of the frozen orbital approximation is assumed as well, where ionic one-electron orbitals do not differ from their neutral counterparts, so that ionization is viewed as a removal of an electron from its orbital, without any changes to the rest of the molecule. Koopmans correlations necessarily break down when the frozen orbital approximation is not valid, which is frequently true, even for weak-field ionization. In addition, the Koopmans correlations fail if ionization is accompanied by a rearrangement of electrons between orbitals.

Another approximate method of calculating ionization yields is by evaluating the magnitudes of the Dyson orbitals associated with the accessible ionization channels. Dyson orbitals, introduced in chapter 5 are one-electron wavefunctions obtained by projecting a final ionic (N-1 electron) state, ψ_n (the nth ionic state), onto the known initial (N electron) state, ψ_m: $\psi_{Dyson} = \sqrt{N}\langle\psi_m^N(r_1, r_2, ..., r_N)|\psi_n^{N-1}(r_1, ..., r_{N-1})\rangle$. Since ψ_m^N and ψ_n^{N-1} are multi-electron eigenstates of the neutral and the ionic Hamiltonians, both contributions from multiple configurations and orbital relaxation effects are taken into account.

In the limit of weak field ionization, it can be shown that the distribution of ionic state yields between ionization channels is proportional to the Dyson orbital amplitudes [150]. If the magnitude of the Dyson orbital associated with an ionization channel is significant, we consider the neutral and the ionic state correlated in the Dyson sense. In the case of strong-field ionization, the strong-field approximation also yields a probability of ionizing to a particular ionic state given by the product of the Dyson orbital magnitude and the tunneling exponent associated with the ionization channel. The tunneling exponent, or Keldysh rate [12], is given by:

$$K(I_p, F_0) = \exp\left[-\frac{2}{3}\frac{(2I_p)^{3/2}}{|F_0|}\right] \tag{6.1}$$

where I$_p$ is the ionization potential associated with the ionization channel and $|F_0|$ is the peak electric field strength.

In order to account for electron rearrangement that may happen during the ionization process, we turn to calculations of strong-field ionization yields that go beyond the standard strong field approximation. The calculations, described below, utilize a more detailed description of the outgoing electron's interaction with the remaining cation.

6.3 Calculations

The strong field ionization calculations presented in this chapter have been performed by Michael Spanner of the Steacie Institute for Molecular Sciences at the National Research Council of Canada. The method used (Time-Dependent Resolution in Ionic States - TD-RIS) has been introduced and described in Ref. [164]. In this method, the bound states are described as field-free multielectron states, and obtained by ab initio electronic structure calculations, described below. These bound state are coupled to one-electron continuum states represented by numerical grids. This method goes beyond some commonly used methods for calculating strong-field ionization (e.g. the strong-field approximation [23], and molecular ADK method [26]) in that it can account for some electron-ion interactions that are typically neglected. These include the distortion of the outgoing electron's wavefunction due to the multi-center nature of the molecular potential, and the rearrangement of core electrons due to the outgoing electron [168]. The calculations were performed by Michael Spanner of the National Research Council of Canada, for the ionization for a half-cycle of 800 nm radiation with a peak intensity of 30 TW/cm^2.

Using a half-cycle pulse to calculate quasi-static ionization rates is justified by the fact that the quasi-static approximation doesn't remember the past history of the pulse, so averaging over many cycles or just a half-cycle should give the same result. Other accepted analytical approximations used to calculate strong field ionization yields, such as the Keldysh [12] or the MO-ADK theory [26], are also based on quasi-static tunneling theory, and average over one period at the peak intensity. The TD-RIS method uses averages only over half a period due to restrictions in computational resources. The sensitivity of the this method to averaging over only half a period as opposed to averaging over a full period has been explicitly checked for the N_2O_4 molecule at several geometries [169]. It did not yield any differences in the relative yields of different ionic states. Furthermore, due to an approximately Gaussian spatial intensity profile of a laser beam, any experimental ionization measurement will have contributions from parts of the laser mode with different intensities. This focal volume spatial intensity averaging complicates any comparison between data and theoretical predictions that were confined to one intensity.

The ab initio calculations used as inputs to the strong field TD-RIS calculations have been performed by prof. Spiridoula Matsika and Congyi Zhou of Temple university. They consisted of state averaged complete active space self-consistent field (CASSCF) calculations and the Dunning aug-cc-pVDZ basis set. The active space for the neutral calculations included 14 electrons in 10 orbitals and 4 states were averaged in the CASSCF, while the ionic calculations used an active space of 13 electrons in 10 orbitals and averaged over 8 ionic states.

6.4 Results and discussion

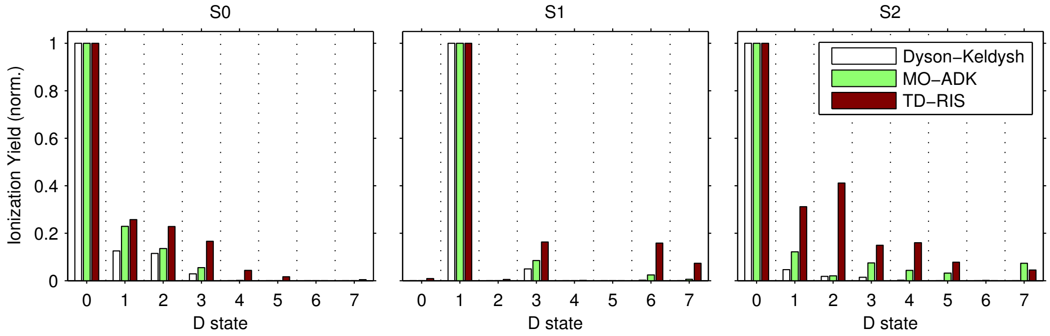

Figure 6.1: Comparison of Dyson-Keldysh, MO-ADK, and TD-RIS calculations for ionization to the various doublet cation states of uracil starting from the ground state (S_0) and first bright excited state of the neutral molecule (S_2).

Figure 6.1 shows strong field ionization yields of uracil, calculated using the three methods we compare here: the Dyson-Keldysh method, the MO-ADK method and the TD-RIS method. The eight lowest-lying states of the cation, D_0-D_7, have been included. The electronic configurations of these states are shown in figure 6.2, while their energies are shown in figure 6.3. The yields were evaluated for ionization starting out of the ground state, S_0, the bright state in our experiments, S_2, and the first excited state S_1, which is potentially populated via non-adiabatic transitions. Calculations for all three neutral states were carried out for the ground state (S_0) equilibrium geometry, with the yields averaged over all angles. Comparison of the angle averaged calculations with angle resolved calculations show only small differences. Note that neither of the methods can provide absolute ionization yields, but they can be used to compare the yields between either initial (neutral) or final (ionic) states within the same method. The results of each calculation shown in figure 6.1 have been normalized to the $S_2 \rightarrow D_0$ yield.

The S_1 state is dark, and is populated only through S_2. Simulations show that at short time delays (shorter than about 70 fs) most of the population is in S_2, so any 69 amu signal would have to have some from S_2, and not from S_1. Simulations show an offset between time delays where the S_1 and S_2 populations peak. Given time for the wavepacket to relax to this state and to pick up enough kinetic energy for the D_1 state to become dissociative, this state would be dominantly producing the 69 amu fragment. For this reason we concentrate on short time delays. Pump probe data give a lower limit for the relaxation away from the FC point of about 70 fs. This is the fitted exponential decay to the parent pump-probe signal, and corresponds to the wavepacket motion away from the FC region on S2, and its reaching a part of the PES, on either the S_1 or S_2, that is about 1 eV lower than the FC region. In addition, this motion of the wavepacket is accompanied by the D_0 energy rising by about 1 eV. This additional energy allows the molecular ion to dissociate, resulting in the reduction of the parent ion signal. At shorter pump-probe delays, any portion of the wave packet on S_1 does not have enough kinetic energy to dissociate from D_1 (see table 6.1).

The low lying states of both the neutral and the cation of uracil have a single dominant configuration. This allows us to describe the ionic states in terms of orbitals that are singly occupied. The configuration of the ground neutral state, S_0, is one in which all the orbitals up to HOMO are doubly occupied, and all the higher lying orbitals unoccupied. Due to the large (4-5 eV) HOMO-LUMO gap, and a much smaller HOMO-1–HOMO gap (both typical of polyatomic molecules) the lowest few states of the cation are 'single hole' state, i.e. they correspond to the removal of an electron from a single orbital that is doubly occupied in the neutral, i.e. in HOMO or lower, but without populating the LUMO (see figure 6.2). Ionic states with energies above the ground ionic D_0 state close to or larger than the HOMO-LUMO gap have configurations that include an electron in the LUMO. The lowest five ionic states (D_0-D_4), shown in figure 6.2, each have only one singly occupied orbital ('single hole' states). This makes the Dyson amplitude for ionization

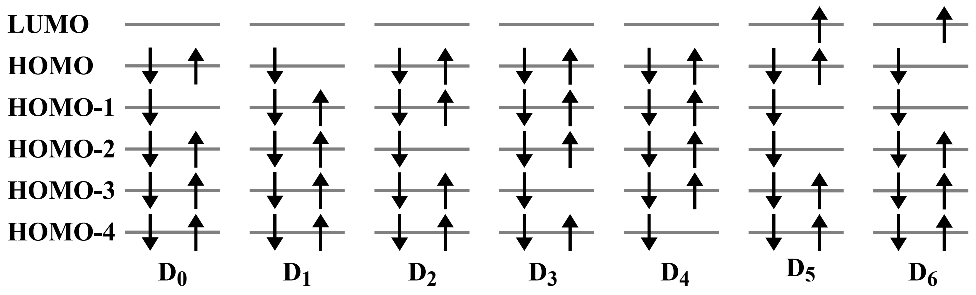

Figure 6.2: Electronic configurations of the lowest seven ionic states of uracil.

from the ground state of the neutral (S_0) to one of these states large, it is correlated with the single-hole states D_0-D_4.

In contrast to S_0, the configurations of excited states S_1 and S_2, which are accessible in our experiments, correspond to singly occupied HOMO or HOMO-1 and LUMO orbital. The one-electron orbitals that are used there have been named (HOMO, HOMO-1, LUMO, etc.) according to their ordering in the neutral molecule. When the Scrödinger equation is solved for the cation, the ordering of the orbitals can switch, and this happens in uracil. The ionic orbitals are not the 'same' as those of the neutral, and the naming is carried over from the neutral based on the one-electron orbitals' similarities in shape between the two species. This is how it is possible to have a HOMO-1 hole in the ground ionic state.

Both S_1 and S_2 are only correlated with a single ionic state that has one singly occupied orbital. In S_2, which corresponds to a HOMO→LUMO excitation, removing the LUMO electron would leave the molecule in the ground state of the ion, which has a single hole in the HOMO orbital. Removing any other electron leaves the molecule either in a state with three unpaired electrons or a highly excited state with a double hole in the HOMO. The lowest lying states that are correlated (in the Dyson sense) with S_2 are D_5 and D_6, each with three unpaired electrons (see figure 6.2).

Removing the LUMO electron from S_1, which corresponds to HOMO-1→LUMO excitation, leaves the molecule in the first excited state of the cation, which has a hole in the HOMO orbital. Thus both S_1 and S_2 are only Dyson-correlated with with one of the lowest five ionic states (D_1 in the case of S_1, and D_0 in the case of S_2). Any observation of ionization of either the S_1 to D_1 - D_4 or of the S_2 leading to cationic states D_1 - D_4 would thus consti-

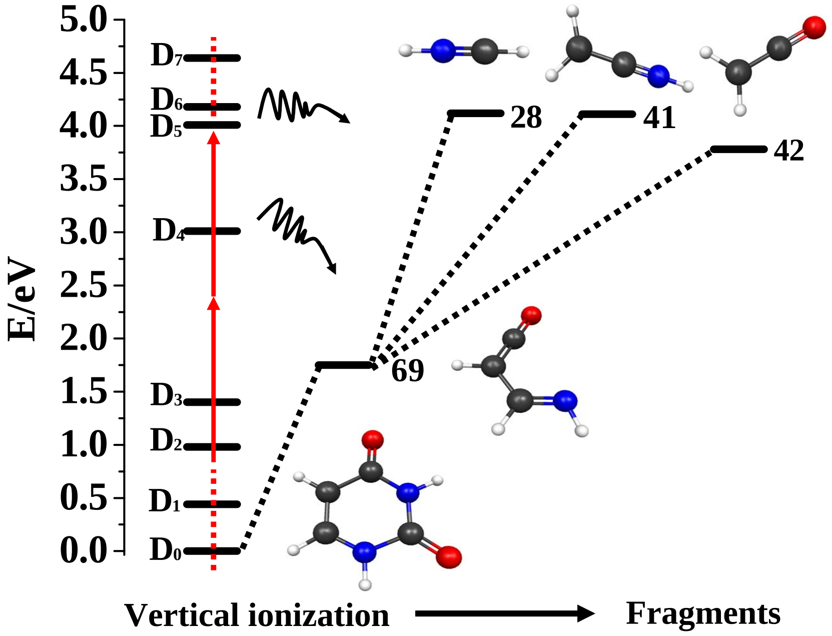

Figure 6.3: Energies of the first several ionic states along with the dissociation energies/barriers to dissociation for the formation of prominent fragments in the TOFMS, measured from the vertical ionization point.

tute a breakdown of Dyson/ADK predictions. We therefore look for ionization from S_1 or S_2 to one of these states to test for breakdown of Dyson-Keldysh predictions. In order to simplify our analysis, we focus on short pump-probe delays, for which the S_1 is not populated, and essentially all excited population is in S_2.

Figure 6.3 shows the results of our *ab initio* electronic structure calculations which allow us to associate molecules ionized to a particular cationic state with fragments in the TOFMS. The left side of the figure shows the energies, measured from the vertical ionization point, of the first several ionic states at the ground state (S_0) minimum geometry (i.e. at vertical ionization). The right side of the figure shows the energetic requirements for the production of prominent fragments in the TOFMS. The energy required is either the height of the barrier to dissociation, or the energy of the fragments, whichever one is higher. A molecule with a total energy above the dissociation threshold for a given fragment will dissociate to form the smallest fragments energetically allowed [170].

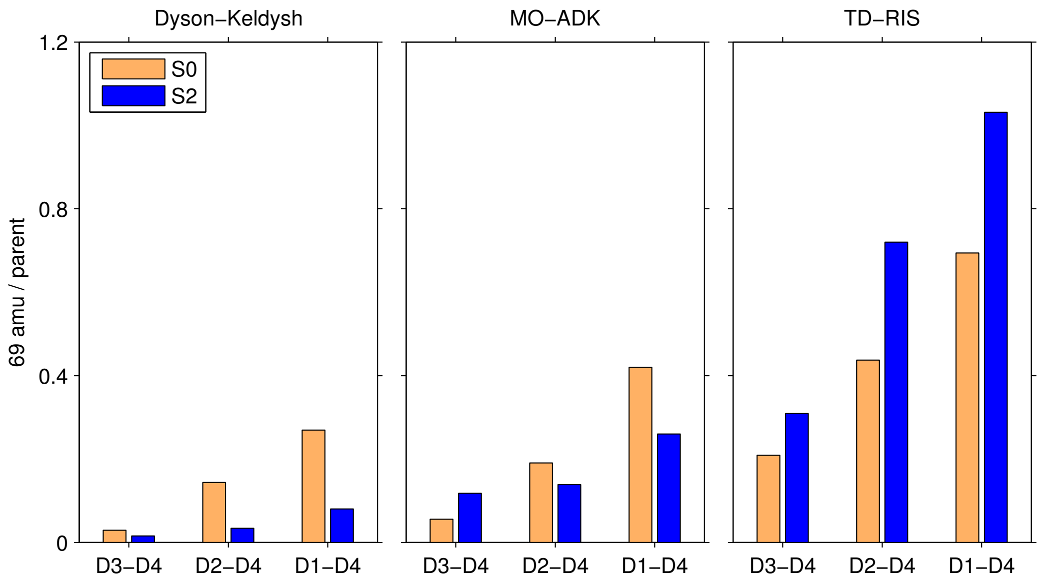

Figure 6.4: Predicted 69/112 ratios for positive (S_2) and negative (S_0) time delays for the Dyson-Keldysh, MO-ADK and TD-RIS calculations considering different combinations of ionic states leading to fragment 69.

Figure 6.3 also shows that the production of fragment at mass 69 amu indicates ionization to D_4, which lies about 2 eV above D_0, and is one of the states that are Dyson forbidden from S_2. However, a molecule with some vibrational kinetic energy can dissociate to produce this fragment even when ionized to some of the states lying below the fragment 69 dissociation threshold. The molecule can acquire the kinetic energy in moving away from the Franck Condon (FC) region on S_2, or the molecule can have some energy stored in other degrees of freedom (being at finite temperature). In order to determine which of the ionic states below D_4 can produce the 69 amu fragment, we look at the energy the molecule can acquire through relaxation on the S_2 potential and the thermal energy stored in the molecules at temperatures used in our experiments. Relaxation from the Franck-Condon region to the S_2 minimum leads to a gain of up to 0.5 eV in vibrational kinetic energy [112, 171]. As for the thermal energy that can be stored in vibrations of the molecule, we based our estimates on the results of Baer at al. [170]. They find that the energy required for dissociative ionization of room temperature halogenated methanes is about 0.15 eV below the dissociation limit. Based on the larger number of degrees of freedom of uracil (30 as opposed to 9), and the higher

Calculation (states leading to 69)	69/112 (S_0)	69/112 (S_2)
Dyson(D_3-D_4)	0.0234	0.0147
Full Calc(D_3-D_4)	0.141	0.179
Dyson(D_2-D_4)	0.128	0.0322
Full Calc(D_2-D_4)	0.348	0.547
Dyson(D_1-D_4)	0.269	0.0804
Full Calc(D_1-D_4)	0.694	1.03

Table 6.1: Predicted 69/112 ratios for positive and negative time delays for the full calculations and Dyson orbital amplitudes considering different combinations of ionic states leading to fragment 69.

temperatures at which our measurements were made (450 K as opposed to 300 K), we estimate that uracil molecules may have up to 600-700 meV of kinetic energy. Given the calculated dissociation barriers, fragment energies and the maximum internal energy stored in the molecules, fragment 69 can certainly be produced from D_4, and potentially from states D_2 and D_3. The total energy available for dissociation on a given ionic state depends on the amount of internal energy stored in rotational degrees of freedom. It also varies with time delay and involves the pooling of energy from multiple degrees of freedom. Since the total energy available for dissociation on a given ionic state may vary with time delay, and involves the pooling of energy from multiple degrees of freedom, we also consider below how sensitive our interpretation is to which ionic states can lead to dissociation.

As figure 6.4 illustrates, the three calculational methods give very different predictions for the ratio of 69/112 as a function of pump probe delay. The Dyson-Keldysh method predicts a decrease in the 69/112 ratio in going from S_0 to S_2. The MO-ADK predicts either an increase or a decrease depending on which cation states are assumed to yield 69 amu. The TD-RIS calculation results predict an increase, regardless of whether molecules can dissociate to form 69 starting from D_1, D_2 or D_3.

Cations which are created with energies greater than 4 eV above the D_0 minimum can fragment further to produce fragments at 42, 41 and 28 amu [158]. Thus depositing 4 eV or more of energy into the molecule leads to Dyson-allowed states, but with enough energy to dissociate into fragments lighter than 69, making the 69 fragment a sole marker of Dyson-forbidden

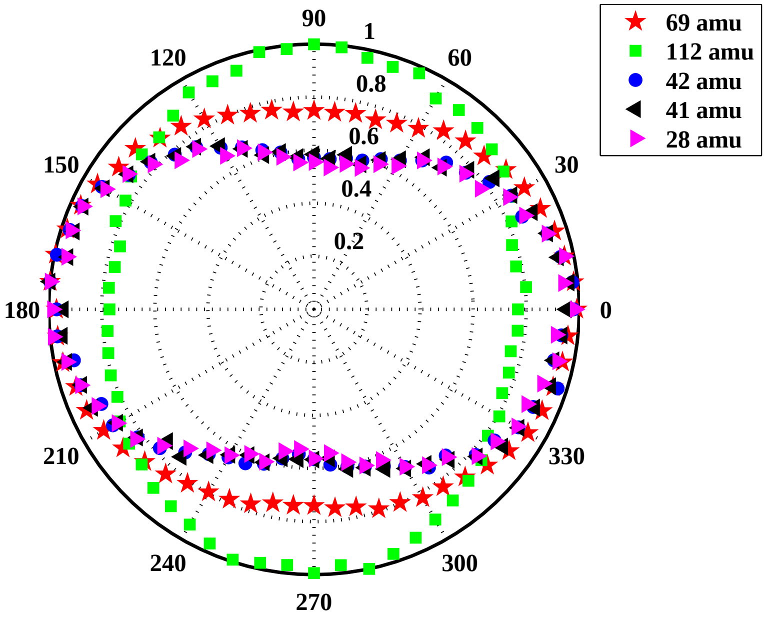

Figure 6.5: Dependence of pump probe ion signals on the relative polarization of the pump and the probe beams. Fragments originating from the same ionic state show the same angular dependence.

transitions. As the calculations only provide relative yields, the most sensitive probe of the calculations at our disposal is the change in 69/112 in going from S_0 to S_2. Thus by looking at how the ratio of the 69 to parent ion yield changes with time delay (i.e. ionizing from S_0 for negative delays and S_2 for positive delays) we can test the Dyson orbital amplitudes for ionization from S_2.

As a check of our interpretation of the *ab initio* electronic structure calculations, we measured the fragment ion yields as a function of the angle between the pump and probe polarization vectors. We expect that any fragments which originate from ionization to the same ionic state should show the same angle dependent yields, whereas fragments originating from ionization to a different ionic state should show different angle dependent yields. Therefore, we expected that fragments 28, 41 and 42 should have the same angle dependent yields if they are generated by ionizing to D_5 or D_6, but they should be different from 69 and the parent ion if these fragments originate from D_2-D_4 and D_0-D_1 respectively. As figure 6.5 shows, these expectations are borne out, corroborating our interpretation outlined above. These observations are consistent with the time dependent yields, which are the same for 28,41 and 42 but different from 69 and 112.

Figure 6.7, shows the measured ratio 69 amu/parent for ionization by the IR pulse alone, corresponding to ionization of S_0, and for ionization by the IR pulse preceded by the UV pulse, corresponding to ionization of S_2. Both are shown as a function of probe power. For ionization from S_2, the ratio of 69 to parent increases with increasing IR intensity, as the ionization of orbitals below the HOMO becomes easier, and rolls over as the ionization of HOMO becomes saturated. Ionization from S_0 starts to exhibit a similar rise in the fragment to parent ratio at much higher probe intensities. At lower probe intensities, where the ionization process is not in the tunneling regime and the ADK picture breaks down, this ratio remains constant. This is consistent with calculated ionization yields reported in [172]. At the lowest pump probe intensities, the signal to noise ratio becomes too low to measure any ion signal.

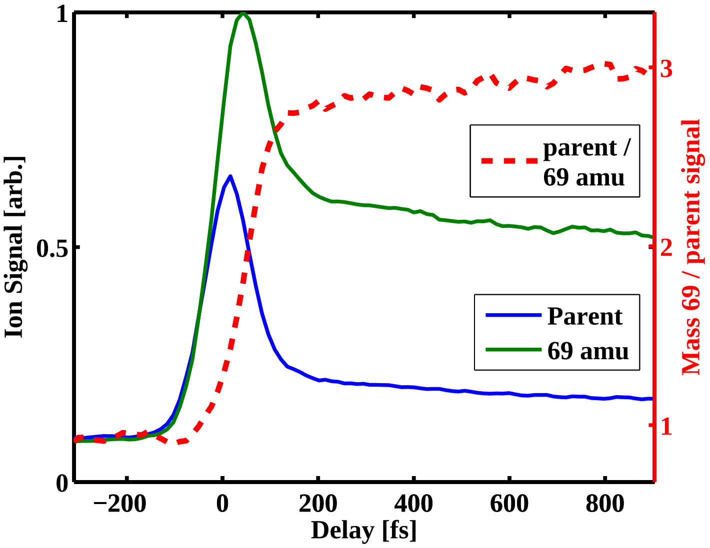

Figure 6.6: Pump-probe ion signals for the parent (blue solid line) and 69 amu (green solid line), and their ratio (red dashed line)

The dashed horizontal lines in figure 6.7, show the TD-RIS calculation results for the 69/parent ratio. The dash-dotted horizontal lines show the the 69/parent ratio obtained by evaluating the Dyson orbital overlaps weighted by the tunneling exponent. Both calculation were performed at fixed probe intensity of 30 TW/cm^2. The Dyson-Keldysh and the TD-RIS calculations give opposite predictions for how the the 69/112 ratio changes in going from S_0 to S_2

ionization. The Dyson orbital amplitudes predict a decrease, whereas the TD-RIS calculations indicate that there should be an increase in the 69/112 ratio. These predictions are not sensitive to which states lead to the measurement of fragment 69. As indicated in table 6.1 below, while the ratio does depend on which states lead to the parent and which to 69, the trends predicted by the full and the Dyson/ADK calculation remain the same, and opposite to each other. Measurements for different intensities showed some variation in the 69/112 ratio, but always the same trend of the ratio increasing in going from S_0 to S_2 as shown in the figure. The measurements are consistent with the TD-RIS calculations and demonstrate that Dyson orbital overlaps do not provide an accurate prediction for which final states are populated via strong field ionization.

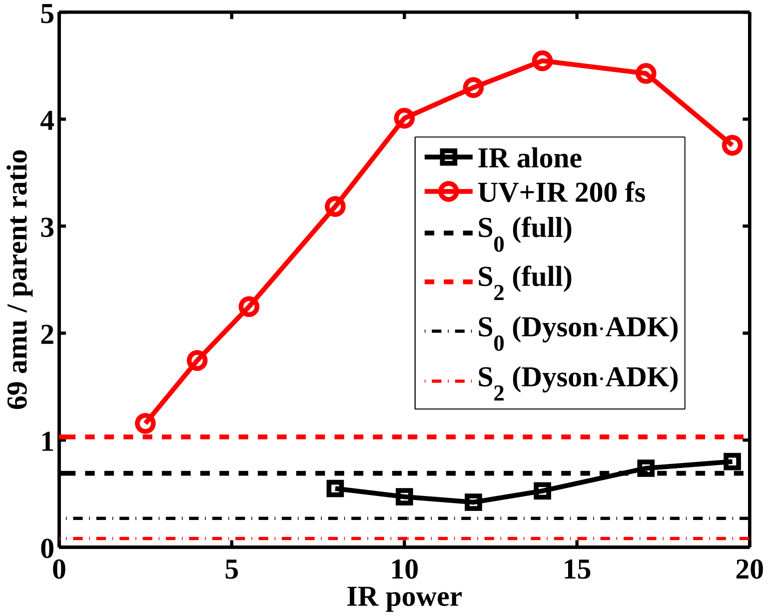

Figure 6.7: The ratio of fragment at 69 amu to the parent ion as a function of probe pulse intensity for measurements with the probe beam alone (black line and squares), measurements in pump-probe configuration at 200 fs delay (red line and circles), full calculation results for ionization from S_0 (black dashed line) and S_2 (red dashed line), Dyson orbital overlaps weighted by ADK exponents for ionization from S_0 (black dash-dotted line) and from S_0 (red dash-dotted line)

Figure 6.6, shows the measured ion yields for the fragment at 69 amu and the parent, and their ratio as a function of pump-probe time delay. The measurements were performed with a probe intensity comparable to the one used for calculations. We note that the ratio of 69 to parent starts increasing as soon as the pumping field is turned on, and rises sharply on a timescale of about 100 fs. As the molecule relaxes and its electronic energy is being converted to vibrational energy, additional ionization channels start to lead to fragmentation to 69 amu. The S_1 state starts to get populated, too. Both of these effects lead to a slow increase in the 69 to parent ratio on timescales of hundreds of femtoseconds to a few picoseconds.

While the calculations agree with the measurements in predicting an increase in the 69/112 ratio as a function of time delay, the calculations generally predict a smaller ratio for both positive and negative delays than measured. One factor that may be contributing to this discrepancy is that the calculations do not include laser driven coupling between different ionic states. These can play a role in uracil, since there is a resonance between D_0 and D_3, which is about 1.6 eV above D_0) [173].

6.5 Conclusions

We demonstrate the breakdown of Dyson orbital amplitudes in predicting final state distributions for strong field ionization of uracil. Fragment 69 becomes the dominant fragment in mass spectrum, despite being produced from the Dyson "forbidden" ionic states D_2-D_4. Multielectron calculations which utilize a more detailed treatment of the electron-ion interaction give the ionization yield to different electronic states of the cation that is qualitative agreement with our strong-field ionization measurements.

Chapter 7

Conclusions

In this thesis, we explored several aspects of molecular strong-field ionization. We began by describing the apparatus that that was used to produce, shape and characterize the UV and IR pulses needed to implement the UV-pump, IR-probe pulse sequence that was used in all the experiments. The vacuum equipment used to enable the interaction of the molecules and the pulses was described as well.

The sensitivity of strong-field to molecular conformation was utilized in experiments presented in chapter 3. It provided the basis for a learning control scheme that was devised with an aim of studying the photochemical isomerization reaction of cyclohexadiene. We were able to control the branching of an excited state wavepacket at a point of intersection of two potential energy surfaces. Controlling this branching ratio effected the control over which final product of the reaction was created.

Extending the approach to studying the molecular dynamics by monitoring the change in strong-field ionization yields with the change in molecular conformation, we turned to the excited state relaxation of nucleic bases in chapter 4. The change in the orbital shape that accompanies the relaxation proved instrumental in interpreting the data presented in this chapter. While it was known that the nucleic bases relax rapidly, it was not clear whether one or more of the accessible pathways are utilized. Our time- and mass-resolved ion yields revealed multiple timescales, and the association of molecular fragments with geometries enabled us to reveal the non-local nature of the relaxation process.

Turning to exploring the intrinsic properties of strong-field ionization, in chapter 5 we explored how this process depends on the molecular orbital from which an electron was removed. Our angle-resolved pump-probe ionization yield measurements show that this process occurs without a rearrangement of the other electrons in the molecule. In contrast, ionization through removal of a deeper-lying electron, which generally leads to an excited state of the ion, was observed to be accompanied by a relaxation of the electrons.

In chapter 6, we looked into the possibilities of predicting the final state(s) of the ionization process from a known initial molecular state. Our system of choice was uracil, and we looked at the way the predicted ionization yields change as the molecules is excited from its ground state to a bright excited state. These methods were the Dyson-Keldysh method, based on the strong-field approximation, the molecular ADK method, and the time-dependent, resolution-in-ionic-states (TD-RIS) method developed by our collaborators. The three methods are compared to our strong-field ionization measurements. The best agreement was found between the TD-RIS method and the experimental data.

The work presented in this thesis is currently being extended on several fronts. Theoretical work, performed by our collaborators at Temple University, aimed at expanding our understanding of the physical processes leading to the delocalization of an excited state wavepacket is currently underway. In addition, the influence of the shape of the molecular wavefunction on the angle resolved ionization yields is currently being used to track the dissociation of CH_2IBr. The dissociation of this molecule is accompanied by a rotation of one of its fragments in the lab frame. Consequently the position of the nodes of the molecular orbital also shifts in a fixed frame, leading to an observable effect.

Bibliography

[1] T.H. Maiman. Stimulated optical radiation in ruby. *Nature*, 1960.

[2] DE Spence, P.N. Kean, and W. Sibbett. 60-fsec pulse generation from a self-mode-locked ti: sapphire laser. *Optics letters*, 16(1):42–44, 1991.

[3] D. Strickland and G. Mourou. Compression of amplified chirped optical pulses. *Optics Communications*, 55(6):447–449, 1985.

[4] P.H. Bucksbaum. The future of attosecond spectroscopy. *Science*, 317(5839):766–769, 2007.

[5] E. Goulielmakis, Z. H. Loh, A. Wirth, R. Santra, N. Rohringer, V. S. Yakovlev, S. Zherebtsov, T. Pfeifer, A. M. Azzeer, M. F. Kling, et al. Real-time observation of valence electron motion. *Nature*, 466(7307):739–743, 2010.

[6] M. F. Kling and M. J. J. Vrakking. Attosecond Electron Dynamics. *Annu. Rev. Phys. Chem.*, 59:463–492, 2008.

[7] S. Baker, J. S. Robinson, C. A. Haworth, H. Teng, R. A. Smith, C. C. Chirilă, M. Lein, J. W. G. Tisch, and J. P. Marangos. Probing proton dynamics in molecules on an attosecond time scale. *Science*, 312(5772):424, 2006.

[8] S. Haessler, J. Caillat, W. Boutu, C. Giovanetti-Teixeira, T. Ruchon, T. Auguste, Z. Diveki, P. Breger, A. Maquet, B. Carré, R Taïeb, and P. Salières. Attosecond imaging of molecular electronic wavepackets. *Nat. Phys*, 6(3):200–206, 2010.

[9] J. Itatani, J. Levesque, D. Zeidler, Hiromichi Niikura, H. Pépin, J. C. Kieffer, P. B. Corkum, and D. M. Villeneuve. Tomographic imaging of molecular orbitals. *Nature*, 432(7019):867–871, 2004.

[10] Manfred Lein. Molecular imaging using recolliding electrons. *Journal of Physics B: Atomic, Molecular and Optical Physics*, 40(16):R135, 2007.

[11] O. Smirnova, Y. Mairesse, S. Patchkovskii, N. Dudovich, D. Villeneuve, P. Corkum, and M.Y. Ivanov. High harmonic interferometry of multi-electron dynamics in molecules. *Nature*, 460(7258):972–977, 2009.

[12] L. V. Keldysh. Ionization in the field of a strong electromagnetic wave. *Sov. Phys. JETP*, 20:1307, 1965.

[13] M.Y. Ivanov, M. Spanner, and O. Smirnova. Anatomy of strong field ionization. *Journal of Modern Optics*, 52(2-3):165–184, 2005.

[14] P. Agostini, F. Fabre, G. Mainfray, G. Petite, and NK Rahman. Free-free transitions following six-photon ionization of xenon atoms. *Physical Review Letters*, 42(17):1127–1130, 1979.

[15] S. Augst, D. Strickland, DD Meyerhofer, SL Chin, and JH Eberly. Tunneling ionization of noble gases in a high-intensity laser field. *Physical review letters*, 63(20):2212–2215, 1989.

[16] R.H. Fowler and L. Nordheim. Electron emission in intense electric fields. *Proceedings of the Royal Society of London.*, 119(781):173–181, 1928.

[17] J. R. Oppenheimer. Three notes on the quantum theory of aperiodic effects. *Phys. Rev.*, 31:66–81, Jan 1928.

[18] JR Oppenheimer. On the quantum theory of the autoelectric field currents. *Proceedings of the National Academy of Sciences of the United States of America*, 14(5):363, 1928.

[19] AM Perelomov, VS Popov, and MV Terent'ev. Ionization of atoms in an alternating electric field. *Soviet Journal of Experimental and Theoretical Physics*, 23:924, 1966.

[20] M. V. Ammosov, N. B. Delone, and V. P. Krainov. Tunnel ionization of complex atoms and of atomic ions in an alternating electromagnetic field. *Sov. Phys. JETP*, 64:1191, 1986.

[21] F. H. M. Faisal. Multiple absorption of laser photons by atoms. *J. Phys. B.*, 6:L89, 1973.

[22] H. R. Reiss. Effect of an intense electromagnetic-field on a weakly bound system. *Phys. Rev. A*, 22:1786, 1980.

[23] J. Muth-Böhm, A. Becker, and F. H. M. Faisal. Suppressed molecular ionization for a class of diatomics in intense femtosecond laser fields. *Phys. Rev. Lett.*, 85:2280–2283, Sep 2000.

[24] A. Becker and F.H.M. Faisal. Intense-field many-body s-matrix theory. *Journal of Physics B: Atomic, Molecular and Optical Physics*, 38:R1, 2005.

[25] M.J. DeWitt and R.J. Levis. Concerning the ionization of large polyatomic molecules with intense ultrafast lasers. *J. Chem. Phys.*, 110:11368, 1999.

[26] X. M. Tong, Z. X. Zhao, and C. D. Lin. Theory of molecular tunneling ionization. *Phys. Rev. A*, 66:033402, Sep 2002.

[27] M. Baer. *Beyond Born-Oppenheimer: electronic nonadiabatic coupling terms and conical intersections*. Wiley-Interscience, 2006.

[28] Bruce Alberts, Alexander Johnson, Julian Lewis, Martin Raff, Keith Roberts, and Peter Walter. *Molecular Biology of the Cell*. Garland Science, 2002.

[29] H. R. Hudock and T. J. Martinez. Excited-State Dynamics of Cytosine Reveal Multiple Intrinsic Subpicosecond Pathways. *Chem.Phys.Chem.*, 9:2486–2490, 2008.

[30] G. N. Gibson, R. R. Freeman, and T. J. McIlrath. Dynamics of the high-intensity multiphoton ionization of N_2. *Phys. Rev. Lett.*, 67(10):1230–1233, 1991.

[31] M. Kotur, T. Weinacht, B.J. Pearson, and S. Matsika. Closed-loop learning control of isomerization using shaped ultrafast laser pulses in the deep ultraviolet. *The Journal of chemical physics*, 130:134311, 2009.

[32] M. Kotur, T.C. Weinacht, C. Zhou, and S. Matsika. Following Ultrafast Radiationless Relaxation Dynamics With Strong Field Dissociative Ionization: A Comparison Between Adenine, Uracil, and Cytosine. *IEEE J. Sel. Top. Quantum Electron*, (99):1–8, 2011.

[33] M. Kotur, T.C. Weinacht, C. Zhou, K.A. Kistler, and S. Matsika. Distinguishing between relaxation pathways by combining dissociative ionization pump probe spectroscopy and ab initio calculations: A case study of cytosine. *J. Chem. Phys.*, 134:184309, 2011.

[34] Marija Kotur, Thomas C. Weinacht, Congyi Zhou, and Spiridoula Matsika. Strong-field molecular ionization from multiple orbitals. *Phys. Rev. X*, 1:021010, 2011.

[35] Marija Kotur, Thomas C. Weinacht, Congyi Zhou, Spiridoula Matsika, Serguei Patchkovskii, and Michael Spanner. Role of electronic state correlation in strong field molecular ionization. *(submitted)*, 2012.

[36] P.H. Nuernberger. Design and construction of an apparatus for the neutral dissociation and ionization of molecules in an intense laser field. Master's thesis, Stony Brook University, 2003.

[37] Sterling Backus, Charles G. Durfee, III, Margaret M. Murnane, and Henry C. Kapteyn. High power ultrafast lasers. *Rev. Sci. Inst.*, 69(3):1207–1223, 1998.

[38] Rick Trebino, Kenneth W. DeLong, David N. Fittinghoff, John N. Sweetser, Marco A. Krumbugel, Bruce A. Richman, and Daniel J. Kane. Measuring ultrashort laser pulses in the time-frequency domain using frequency-resolved optical gating. *Rev. Sci. Inst.*, 68(9):3277–3295, 1997.

[39] D. P. M. Geissler. Concerted elimination of Cl_2^+ from CCl_4 and of I_2^+ from CH_2I_2 driven by intense ultrafast laser pulses. Master's thesis, Stony Brook University, 2007.

[40] A. M. Weiner. Femtosecond optical pulse shaping and processing. *Progress in Quantum Electronics*, 19(3):161–237, 1995.

[41] Brett J. Pearson and Thomas C. Weinacht. Shaped ultrafast laser pulses in the deep ultraviolet. *Opt. Express*, 15(7):4385–4388, 2007.

[42] R. Trebino and D.J. Kane. Using phase retrieval to measure the intensity and phase of ultrashort pulses: frequency-resolved optical gating. *JOSA A*, 10(5):1101–1111, 1993.

[43] Florian Langhojer, David Cardoza, Mark Baertschy, and Thomas Weinacht. Gaining mechanistic insight from closed loop learning control: The importance of basis in searching the phase space. *J. Chem. Phys.*, 122:014102, 2005.

[44] D.M. Neumark. Time-resolved photoelectron spectroscopy of molecules and clusters. *Annual Review of Physical Chemistry*, 52(1):255–277, 2001.

[45] S. Patchkovskii, Z. Zhao, T. Brabec, and D.M. Villeneuve. High harmonic generation and molecular orbital tomography in multielectron systems: Beyond the single active electron approximation. *Phys. Rev. Lett.*, 97(12):123003, 2006.

[46] C.-H. Tseng. *Ultrafast Coherent Control Spectroscopy.* PhD thesis, Stony Brook University, 2012.

[47] W. Zielenkiewicz. Enthalpies of sublimation and vapor pressures of adenine, 1-methyladenine, 2-methyladenine, 3-methyladenine, and 8-methyladenine. *Journal of Chemical & Engineering Data*, 45(4):626–629, 2000.

[48] L.B. Clark, G.G. Peschel, and I. Tinoco Jr. Vapor spectra and heats of vaporization of some purine and pyrimidine bases1. *The Journal of Physical Chemistry*, 69(10):3615–3618, 1965.

[49] D. Ferro, L. Bencivenni, R. Teghil, and R. Mastromarino. Vapour pressures and sublimation enthalpies of thymine and cytosine. *Thermochimica Acta*, 42(1):75–83, 1980.

[50] G. Bardi, L. Bencivenni, D. Ferro, B. Martini, S. Nunziante Cesaro, and R. Teghil. Thermodynamic study of the vaporization of uracil. *Thermochimica Acta*, 40(2):275–282, 1980.

[51] Richard S. Judson and Herschel Rabitz. Teaching lasers to control molecules. *Phys. Rev. Lett.*, 68(10):1500–1503, 1992.

[52] L. Davis and M. Mitchell. *Handbook of genetic algorithms.* Van Nostrand Reinhold, 1991.

[53] S. A. Trushin, W. Fuß, T. Schikarski, W. E. Schmid, and K. L. Kompa. Femtosecond photochemical ring opening of 1,3-cyclohexadiene studied by time-resolved intense-field ionization. *J. Chem. Phys.*, 106(22):9386–9389, 1997.

[54] R. W. Schoenlein, L. A. Peteanu, R. A. Mathies, and C. V. Shank. The first step in vision: femtosecond isomerization of rhodopsin. *Science*, 254:412, 1991.

[55] M. J. Pilling and S. Robertson. Master equation models for chemical reactions of importance in combustion. *Ann. Rev. Phys. Chem.*, 54:245–275, 2003.

[56] B. G. Levine and T. J. Martinez. Isomerization through conical intersections. *Ann. Rev. Phys. Chem.*, 58:613, 2007.

[57] Wing Tsang. Progress in the development of combustion kinetics databases for liquid fuels. *Data Science Journal*, 3:1, 2004.

[58] Suhail P. Shah and Stuart A. Rice. Controlling quantum wavepacket motion in reduced-dimensional spaces: reaction path analysis in optimal control of hcn isomerization. *Faraday Discuss.*, 113:319–331, 1999.

[59] Valentyn I. Prokhorenko, Andrea M. Nagy, Stephen A. Waschuk, Leonid S. Brown, Robert R. Birge, and R. J. Dwayne Miller. Coherent control of retinal isomerization in bacteriorhodopsin. *Science*, 313:1257, 2006.

[60] Hiroyuki Tamura, Shinkoh Nanbu, Toshimasa Ishida, and Hiroki Nakamura. Laser control of reactions of photoswitching functional molecules. *J. Chem. Phys.*, 125(3):034307, 2006.

[61] G. Vogt, G. Krampert, P. Niklaus, P. Nuernberger, and G. Gerber. Optimal control of photoisomerization. *Phys. Rev. Lett.*, 94:068305, 2005.

[62] Benjamin Dietzek, Ben Bruggemann, Torbjorn Pascher, and Arkady Yartsev. Mechanisms of molecular response in the optimal control of photoisomerization. *Phys. Rev. Lett.*, 97(25):258301, 2006.

[63] Elizabeth C. Carroll, James L. White, Andrei C. Florean, Philip H. Bucksbaum, and Roseanne J. Sension. Multiphoton control of the 1,3-cyclohexadiene ring-opening reaction in the presence of competing solvent reactions. *J. Phys. Chem. A*, 112(30):6811–6822, 2008.

[64] E. C. Carroll, B. J. Pearson, A. C. Florean, P. H. Bucksbaum, and Roseanne J. Sension. Spectral phase effects on nonlinear resonant photochemistry of 1,3-cyclohexadiene in solution. *J. Chem. Phys.*, 124(11):114506, 2006.

[65] Kunihito Hoki and Paul Brumer. Mechanisms in adaptive feedback control: Photoisomerization in a liquid. *Phys. Rev. Lett.*, 95:168305, 2005.

[66] W. Fuß, W. E. Schmid, and S. A. Trushin. Time-resolved dissociative intense-laser field ionization for probing dynamics: Femtosecond photochemical ring opening of 1,3-cyclohexadiene. *J. Chem. Phys.*, 112(19):8347–8362, 2000.

[67] P. Celani, F. Bernardi, M.A. Robb, and M. Olivucci. Do photochemical ring-openings occur in the spectroscopic state? $^1B_2$ pathways for the cyclohexadiene/hexatriene photochemical interconversion. *J. Phys. Chem.*, 100(50):19364–19366, 1996.

[68] Suart H. Pullen, Neil A. Anderson, Larry A. Walker, II, and Roseanne J. Sension. The ultrafast photochemical ring-opening reaction of 1,3-cyclohexadiene in cyclohexane. *J. Chem. Phys.*, 108:556–563, 1998.

[69] Angelika Hofmann and Regina de Vivie-Riedle. Quantum dynamics of photoexcited cyclohexadiene introducing reactive coordinates. *J. Chem. Phys.*, 112(11):5054–5059, 2000.

[70] M. Garavelli, C. S. Page, P. Celani, M. Olivucci, W. E. Schmid, S. A. Trushin, and W. Fuß. Reaction path of a sub-200 fs photochemical electrocyclic reaction. *J. Phys. Chem. A*, 105:4458–4469, 2001.

[71] Hiroyuki Tamura, Shinkoh Nanbu, Toshimasa Ishida, and Hiroki Nakamura. *Ab initio* nonadiabatic quantum dynamics of cyclohexadiene/hexatriene ultrafast photoisomerization. *J. Chem. Phys.*, 124(8):084313, 2006.

[72] Narayanan Kuthirummal, Fedor M. Rudakov, Conor L. Evans, and Peter M. Weber. Spectroscopy and femtosecond dynamics of the ring opening reaction of 1,3-cyclohexadiene. *J. Chem. Phys.*, 125(13):133307, 2006.

[73] H. J. C. Jacobs and E. Havinga. Photochemistry of vitamin d and its isomers and of simple trienes. *Advan. Photochem.*, 11:305–373, 1979.

[74] D. C. Cardoza. *Understanding and Applying Learning Control to Molecular Fragmentation.* PhD thesis, Stony Brook University, 2006.

[75] JM Geremia, W. Zhu, and H. Rabitz. Incorporating physical implementation concerns into closed loop quantum control experiments. *The Journal of Chemical Physics*, 113:10841, 2000.

[76] A. Szabo and N. S. Ostlund. *Modern quantum chemistry: introduction to advanced electronic structure theory.* Dover Pubns, 1996.

[77] H. Lischka, R. Shepard, R. M. Pitzer, I. Shavitt, M. Dallos, Th. Müller, P. G. Szalay, M. Seth, G. S. Kedziora, S. Yabushita, and Z. Zhang. High-level multireference methods in the quantum-chemistry program system COLUMBUS: Analytic MR-CISD and MR-AQCC gradients and MR-AQCC-LRT for excited states, GUGA spin-orbit CI and parallel CI density. *Phys. Chem. Chem. Phys.*, 3:664, 2001.

[78] H. Lischka, R. Shepard, I. Shavitt, R. M. Pitzer, M. Dallos, Th. Müller, P. G. Szalay, F. B. Brown, R. Ahlrichs, H. J. Böhm, A. Chang, D. C. Comeau, R. Gdanitz, H. Dachsel, C. Ehrhardt, M. Ernzerhof, P. Hchtl, S. Irle, G. Kedziora, T. Kovar, V. Parasuk, M. J. M. Pepper, P. Scharf, H. Schiffer, M. Schindler, M. Schler, M. Seth, E. A. Stahlberg, J.-G. Zhao, S. Yabushita, Z. Zhang, M. Barbatti, S. Matsika, M. Schuurmann, D. R. Yarkony, S. R. Brozell, E. V. Beck, , and J.-P. Blaudeau. Columbus, an ab initio electronic structure program, release 5.9.1. 2006.

[79] M. W. Schmidt, K. K. Baldridge, J. A. Boatz, S. T. Elbert, M. S. Gordon, J. H. Jensen, S. Koseki, N. Matsunaga, K. A. Nguyen, S. Su, T. L. Windus, M. Dupuis, and J.. A. Montgomery. Computation of Conical Intersections by Using Perturbation Techniques. *J. Comput. Chem.*, 14:1347, 1993.

[80] JL White, J. Kim, VS Petrovic, and PH Bucksbaum. Ultrafast ring opening in 1, 3-cyclohexadiene investigated by simplex-based spectral unmixing. *Journal of Chemical Physics*, 136(5):54303, 2012.

[81] Brett J. Pearson, Sarah R. Nichols, and Thomas Weinacht. Molecular fragmentation driven by ultrafast dynamic ionic resonances. *J. Chem. Phys.*, 127(13):131101, 2007.

[82] S. Lochbrunner, W. Fuß, W.E. Schmid, and K. L. Kompa. Electronic relaxation and ground-state dynamics of 1,3-cyclohexadiene and cis-hexatriene in ethanol. *J. Phys. Chem. A*, 102(47):9334–9344, 1998.

[83] Robert C. Dunbar and Harry Ho-I Teng. Photodissociation spectroscopy of hexatriene cations. *J. Am. Chem. Soc.*, 100(8):2279–2283, 1978.

[84] M. Allan, J. Dannacher, and J. P. Maier. Radiative and fragmentation decay of the cations of trans- and cis-1,3,5-hexatriene and of all trans-1,3,5-heptatriene in the a-tilde(pi [sup - 1]) states, studied by emission and photoelectron–photoion coincidence spectroscopy. *J. Chem. Phys.*, 73(7):3114–3122, 1980.

[85] M. P. Fulscher, S. Matzinger, and T. Bally. Excited states in polyene rad-

ical cations. an ab initio theoretical study. *Chem. Phys. Lett.*, 236:167–176, 1995.

[86] Manuel Joffre. Comment on "Coherent control of retinal isomerization in bacteriorhodopsin". *Science*, 317(5837):453, 2007.

[87] Valentyn I. Prokhorenko, Andrea M. Nagy, Stephen A. Waschuk, Leonid S. Brown, Robert R. Birge, and R. J. Dwayne Miller. Response to comment on "Coherent control of retinal isomerization in bacteriorhodopsin". *Science*, 317(5837):453, 2007.

[88] Dorothee Geppert and Regina de Vivie-Riedle. Reaction velocity control by manipulating the momentum of a nuclear wavepacket with phase-sensitive optimal control theory. *Chem. Phys. Lett.*, 404:289–295, 2005.

[89] K. Kosma, SA Trushin, W. Fuss, and WE Schmid. Cyclohexadiene ring opening observed with 13 fs resolution: coherent oscillations confirm the reaction path. *Phys. Chem. Chem. Phys.*, 11(1):172–181, 2008.

[90] P. R. Callis. Electronic States and Luminescence of Nucleic Acid Systems. *Ann. Rev. Phys. Chem.*, 34:329, 1983.

[91] Carlos E. Crespo-Hernndez, Boiko Cohen, Patrick M. Hare, and Bern Kohler. Ultrafast excited-state dynamics in nucleic acids. *Chem. Rev.*, 104(4):1977–2020, 2004.

[92] C. T. Middleton, K. de La Harpe, C. Su, Y. K. Law, C. E. Crespo-Hernandez, and B. Kohler. DNA Excited-State Dynamics: From Single Bases to the Double Helix. *Annu. Rev. Phys. Chem.*, 60:217–239, 2009.

[93] S. Ullrich, T. Schultz, M. Z. Zgierski, and A. Stolow. Electronic Relaxation Dynamics in DNA and RNA Bases Studied by Time-resolved Photoelectron Spectroscopy. *Phys. Chem. Chem. Phys.*, 6:2796, 2004.

[94] H. Kang, K. T. Lee, B. Jung, Y. J. Ko, and S. K. Kim. intrinsic Lifetimes of the Excited State of DNA and RNA Bases. *J. Am. Chem. Soc.*, 124:12958, 2002.

[95] C. Canuel, M. Mons, F. Piuzzi, B. Tardinel, I. Dimicoli, and M. Elhanine. Excited states dynamics of DNA and RNA bases: Characterization of a stepwise deactivation pathway in the gas phase. *J. Chem. Phys.*, 122:074316, 2005.

[96] J.-M. L. Pecourt, J. Peon, and B. Kohler. Ultrafast Internal Conversion of Electronically Excited RNA and DNA Nucleosides in Water. *J. Am. Chem. Soc.*, 122:9348, 2000.

[97] K. A. Kistler and S. Matsika. *Quantum Mechanical Studies of the Photophysics of DNA and RNA Bases*, volume 7, pages 285–339. Springer Verlag, Netherlands, 2009.

[98] J. González-Vázquez and L. González. A Time-Dependent Picture of the Ultrafast Deactivation of keto-Cytosine Including Three-State Conical Intersections. *ChemPhysChem*, 11(17):3617–3624, 2010.

[99] Kyriaki Kosma, Christian Schrter, Elena Samoylova, Ingolf Volker Hertel, and Thomas Schultz. Excited-State Dynamics of Cytosine Tautomers. *J. Am. Chem. Soc.*, 131(46):16939–16943, 2009.

[100] Hyuk Kang, Kang Taek Lee, Boyong Jung, Yeon Jae Ko, and Seong Keun Kim. Intrinsic lifetimes of the excited state of DNA and RNA bases. *J. Am. Chem. Soc.*, 124(44):12958–12959, 2002.

[101] Y. He, C. Wu, and W. Kong. Decay Pathways of Thymine and Methyl-substituted Uracil and Thymine in the gas Phase. *J. Phys. Chem. A*, 107:5145, 2003.

[102] P. M. Hare, C. E. Crespo-Hernandez, and B. Kohler. Internal Conversion to the Electronic Ground State Occurs via Two Distinct Pathways for the Pyrimidine Bases in Aqueous Solution. *Proc. Natl. Acad. Sci. U.S.A.*, 104:435–440, 2007.

[103] Albert Stolow. Femtosecond time-resolved photoelectron spectroscopy of polyatomic molecules. *Annu. Rev. Phys. Chem.*, 54(1):89–119, 2003.

[104] Daniel M Neumark. Time-resolved photoelectron spectroscopy of molecules and clusters. *Annu. Rev. Phys. Chem.*, 52(1):255–277, 2001.

[105] C.F. Guerra, F.M. Bickelhaupt, S. Saha, and F. Wang. Adenine tautomers: relative stabilities, ionization energies, and mismatch with cytosine. *The Journal of Physical Chemistry A*, 110(11):4012–4020, 2006.

[106] C. Plützer and K. Kleinermanns. Tautomers and electronic states of jet-cooled adenine investigated by double resonance spectroscopy. *Phys. Chem. Chem. Phys.*, 4(20):4877–4882, 2002.

[107] Vitaliy Feyer, Oksana Plekan, Robert Richter, Marcello Coreno, Gemma Vall-llosera, Kevin C. Prince, Alexander B. Trofimov, Irina L. Zaytseva, Tatyana E. Moskovskaya, Evgeniy V. Gromov, and Jochen Schirmer. Tautomerism in cytosine and uracil: An experimental and theoretical core level spectroscopic study. *J. Phys. Chem. A*, 113(19):5736–5742, 2009.

[108] Ronald D. Brown, Peter D. Godfrey, Donald McNaughton, and Anthony P. Pierlot. A study of the major gas-phase tautomer of adenine by microwave spectroscopy. *Chem. Phys. Lett.*, 156(1):61–63, 1989.

[109] K. Tomić, T. Jörg, and C. M. Marian. Quantum chemical investigation of the electronic spectra of the keto, enol, and keto-imine tautomers of cytosine. *J. Phys. Chem. A*, 109:8410–8418, 2005.

[110] E. Nir, M. Müller, LI Grace, and MS De Vries. REMPI spectroscopy of cytosine. *Chem. Phys. Lett.*, 355(1-2):59–64, 2002.

[111] S. Perun, A. L. Sobolewski, and W. Domcke. Ab Initio Studies on the Radiationless Decay Mechanisms of the Lowest Excited Singlet States of 9H-Adenine. *J. Am. Chem. Soc.*, 127:6257–6265, 2005.

[112] S. Matsika. Radiationless Decay of Excited States of Uracil Through Conical Intersections. *J. Phys. Chem. A*, 108:7584, 2004.

[113] K. A. Kistler and S. Matsika. Radiationless Decay Mechanism of Cytosine: An Ab Initio Study with Comparisons to the Fluorescent Analogue 5-Methyl-2-pyrimidinone. *J. Phys. Chem. A*, 111:2650–2661, 2007.

[114] D. Dougherty, K. Wittel, J. Meeks, and S. P. McGlynn. Photoelectron spectroscopy of carbonyls. ureas, uracils, and thymine. *J. Am. Chem. Soc.*, 98(13):3815–3820, 1976.

[115] D. Dougherty, E. S. Younathan, R. Voll, S. Abdulnur, and S. P. McGlynn. Photoelectron spectroscopy of some biological molecules. *J. Electron. Spectrosc. Relat. Phenom.*, 13(3):379 – 393, 1978.

[116] Shigeyuki Urano, Xu Yang, and Pierre R. LeBreton. UV photoelectron and quantum mechanical characterization of DNA and RNA bases: valence electronic structures of adenine, 1,9-dimethyl-guanine, 1-methylcytosine, thymine and uracil. *J. Mol. Struct.*, 214:315 – 328, 1989.

[117] N. Ismail, L. Blancafort, M. Olivucci, B. Kohler, and M. A. Robb. Ultrafast Decay of Electronically Excited Singlet Cytosine via π,π^* to n,π^* State Switch. *J. Am. Chem. Soc.*, 124:6818, 2002.

[118] M. Merchán and L. Serrano-Andrés. Ultrafast Internal Conversion of Excited Cytosine via the Lowest $\pi\pi^*$ Electronic Singlet State. *J. Am. Chem. Soc.*, 125:8108, 2003.

[119] M. Merchán, R. Gonzalez-Luque, T. Climent, L. Serrano-Andrés, E. Rodriuguez, M. Reguero, and D. Pelaez. Unified Model for the Ultrafast Decay of Pyrimidine Nucleobases. *J. Phys. Chem. B*, 110:26471–26476, 2006.

[120] M. Z. Zgierski, S. Patchkovskii, and E. C. Lim. Ab initio study of a biradical radiationless decay channel of the lowest excited electronic state of cytosine and its derivatives. *J. Chem. Phys.*, 123:081101, 2005.

[121] L. Blancafort. Energetics of cytosine singlet excited-state decay paths - A difficult case for CASSCF and CASPT2 . *Photochem. Photobiol.*, 83:603–610, 2007.

[122] Z. Lan, E. Fabiano, and W. Thiel. Photoinduced Nonadiabatic Dynamics of Pyrimidine Nucleobases: On-the-Fly Surface-Hopping Study with Semiempirical Methods. *J. Phys. Chem. B*, 113(11):3548–3555, 2009.

[123] L. Blancafort and M. A. Robb. Key Role of a Threefold State Crossing in the Ultrafast Decay of Electronically Excited Cytosine. *J. Phys. Chem. A*, 108:10609, 2004.

[124] K. A. Kistler and S. Matsika. Three-state Conical Intersections in Cytosine and Pyrimidinone Bases. *J. Chem. Phys.*, 128:215102, 2008.

[125] A. L. Sobolewski, W. Domcke, C. Dedonder-Lardeux, and C. Jouvet. Excited-state hydrogen detachment and hydrogen transfer driven by repulsive (1)pi sigma* states: A new paradigm for nonradiative decay in aromatic biomolecules. *Phys. Chem. Chem. Phys.*, 4:1093–1100, 2002.

[126] S. Perun, A. L. Sobolewski, and W. Domcke. Photostability of 9h-adenine: mechanisms of the radiationless deactivation of the lowest excited singlet states. *Chem. Phys.*, 313:107–112, 2005.

[127] H. Chen and S. H. Li. Theoretical Study toward Understanding Ultrafast Internal Conversion of Excited 9H-Adenine. *J. Phys. Chem. A*, 109:8443–8446, 2005.

[128] C. M. Marian. A New Pathway for the Rapid Decay of Electronically Excited Adenine. *J. Chem. Phys.*, 122:104314, 2005.

[129] L. Blancafort. Excited-State Potential Energy Surface for the Photophysics of Adenine. *J. Am. Chem. Soc.*, 128:210–219, 2006.

[130] L. Serrano-Andrés, M. Merchán, and A. C. Borin. Adenine and 2-Aminopurine: Paradigms of Modern Theoretical Photochemistry. *Proc. Natl. Acad. Sci. U.S.A.*, 103:8691–8696, 2006.

[131] W. C. Chung, Z. Lan, Y. Ohtsuki, N. Shimakura, W. Domcke, and Y. Fujimura. Conical Intersections Involving the Dissociative $^1\pi\sigma^*$ State in H-Adenine: a Quantum Chemical Ab Initio Study. *Phys. Chem. Chem. Phys.*, 9:2075–2084, 2007.

[132] M. Z. Zgierski, S.Patchkovskii, and E. C. Lim. Biradical radiationless decay channel in adenine and its derivatives. *Can. J. Chem.*, 85:124, 2007.

[133] Mario Barbatti and Hans Lischka. Nonadiabatic deactivation of 9H-adenine: A comprehensive picture based on mixed quantum-classical dynamics. *J. Am. Chem. Soc.*, 130(21):6831–6839, 2008.

[134] Walid Mohamed Ibrahim Hassan, Wilfredo Credo Chung, Noriyuki Shimakura, Shiro Koseki, Hirohiko Kono, and Yuichi Fujimura. Ultrafast radiationless transition pathways through conical intersections in photo-excited 9H-adenine. *Phys. Chem. Chem. Phys.*, 12(20):5317–5328, 2010.

[135] and A. Stolow. Excited-State Dynamics of Isolated DNA Bases: A Case Study of Adenine. *Chem. Phys. Chem*, 10:101–110, 2009.

[136] M. Z. Zgierski, S. Patchkovskii, T. Fujiwara, and E. C. Lim. On the Origin of the Ultrafast Internal Conversion of Electronically Excited Pyrimidine Bases. *J. Phys. Chem. A*, 109:9384–9387, 2005.

[137] T. Gustavsson, A. Banyasz, E. Lazzarotto, D. Markovitsi, G. Scalmani, M. J. Frisch, V. Barone, and R. Improta. Singlet excited-state behavior of uracil and thymine in aqueous solution: A combined experimental and computational study of 11 uracil derivatives. *J. Am. Chem. Soc.*, 128:607–619, 2006.

[138] H. R. Hudock, B. G. Levine, A. L. Thompson, H. Satzger, D. Townsend, N. Gador, S. Ullrich, A. Stolow, and T. J. Martinez. Ab Initio Molecular Dynamics and Time-Resolved Photoelectron Spectroscopy of Electronically Excited Uracil and Thymine. *J. Phys. Chem. A*, 111:8500–8508, 2007.

[139] N.B. Slater. *Theory of unimolecular reactions.* Cornell University Press Ithaca, New York, 1959.

[140] Jill K. Wolken, Chunxiang Yao, Frantisek Turecek, Michael J. Polce, and Chrys Wesdemiotis. Cytosine neutral molecules and cation-radicals in the gas-phase: Structures, energetics, ion chemistry, and neutralization-reionization mass spectrometry. *Int. J. Mass. Spectrom.*, 267(1-3):30 – 42, 2007.

[141] Jerry M. Rice, Gerald O. Dudek, and Michael Barber. Mass spectra of nucleic acid derivatives. pyrimidines. *J. Am. Chem. Soc.*, 87(20):4569–4576, 1965.

[142] Leonid Belau, Kevin R. Wilson, Stephen R. Leone, and Musahid Ahmed. Vacuum-ultraviolet photoionization studies of the microhydration of dna bases (guanine, cytosine, adenine, and thymine). *J. Phys. Chem. A*, 111(31):7562–7568, 2007.

[143] D. Pavičić, K. F. Lee, D. M. Rayner, P. B. Corkum, and D. M. Villeneuve. Direct measurement of the angular dependence of ionization for N_2, O_2, and CO_2 in intense laser fields. *Phys. Rev. Lett.*, 98(24):243001, 2007.

[144] A.S. Alnaser, S. Voss, X.M. Tong, C.M. Maharjan, P. Ranitović, B. Ulrich, T. Osipov, B. Shan, Z. Chang, and C.L. Cocke. Effects Of Molecular Structure on Ion Disintegration Patterns In Ionization of O_2 and N_2 by Short Laser Pulses. *Phys. Rev. Lett.*, 93(11):113003, 2004.

[145] O. Smirnova, S. Patchkovskii, Y. Mairesse, N. Dudovich, and M. Y. Ivanov. Strong-field control and spectroscopy of attosecond electron-hole dynamics in molecules. *Proc. Natl. Acad. Sci. USA*, 106(39):16556, 2009.

[146] Z. X. Zhao, X. M. Tong, and C. D. Lin. Alignment-dependent ionization probability of molecules in a double-pulse laser field. *Phys. Rev. A*, 67(4):043404, Apr 2003.

[147] A. Jaroń-Becker, A. Becker, and F. H. M. Faisal. Ionization of n_2, o_2, and linear carbon clusters in a strong laser pulse. *Phys. Rev. A*, 69(2):023410, Feb 2004.

[148] W. Li, A. A. Jaroń-Becker, C. W. Hogle, V. Sharma, X. Zhou, A. Becker, H. C. Kapteyn, and M. M. Murnane. Visualizing electron rearrangement in space and time during the transition from a molecule to atoms. *Proc. Natl. Acad. Sci. USA*, 107(47):20219, 2010.

[149] B. K. McFarland, J. P. Farrell, P. H. Bucksbaum, and M. Gühr. High harmonic generation from multiple orbitals in N_2. *Science*, 322(5905):1232, 2008.

[150] B.T. Pickup. Theory of fast ionization processes. *Chemical Physics*, 19(2):193–208, 1977.

[151] H. Stapelfeldt and T. Seideman. Colloquium: Aligning molecules with strong laser pulses. *Rev. Mod. Phys.*, 75(2):543, 2003.

[152] C. Z. Bisgaard, O. J. Clarkin, G. Wu, A. Lee, O. Geßner, C. C. Hayden, and A. Stolow. Time-resolved molecular frame dynamics of fixed-in-space cs_2 molecules. *Science*, 323(5920):1464, 2009.

[153] C.Z. Bisgaard, M.D. Poulsen, E. Péronne, S.S. Viftrup, and H. Stapelfeldt. Observation of enhanced field-free molecular alignment by two laser pulses. *Physical review letters*, 92(17):173004, 2004.

[154] V. Kumarappan, C.Z. Bisgaard, S.S. Viftrup, L. Holmegaard, and H. Stapelfeldt. Role of rotational temperature in adiabatic molecular alignment. *The Journal of chemical physics*, 125:194309, 2006.

[155] I. V. Litvinyuk, Kevin F. Lee, P. W. Dooley, D. M. Rayner, D. M. Villeneuve, and P. B. Corkum. Alignment-dependent strong field ionization of molecules. *Phys. Rev. Lett.*, 90:233003, 2003.

[156] M. Kasha. Characterization of electronic transitions in complex molecules. *Discuss. Faraday Soc.*, 9:14–19, 1950.

[157] D. Geißler, T. Rozgonyi, J. González-Vázquez, L. González, P. Marquetand, and T.C. Weinacht. Pulse-Shape-Dependent Strong-Field Ionization Viewed with Velocity Map Imaging. *Physical Review A*, 84(5):053422, 2011.

[158] C. Zhou, S Matsika, M. Kotur, and T. C. Weinacht. Fragmentation Pathways in Uracil Radical Cations. *(submitted)*, 2011.

[159] H. W. Jochims, M. Schwell, H. Baumgartel, and S. Leach. Photoion mass spectrometry of adenine, thymine and uracil in the 6-22 eV photon energy range. *Chem. Phys.*, 314(1-3):263–282, 2005.

[160] Jonathan G. Underwood, Benjamin J. Sussman, and Albert Stolow. Field-Free Three Dimensional Molecular Axis Alignment. *Phys. Rev. Lett.*, 94(14):143002, Apr 2005.

[161] Hideo Harada, Seiji Shimizu, Tomoyuki Yatsuhashi, Shuji Sakabe, Yasukazu Izawa, and Nobuaki Nakashima. A key factor in parent and fragment ion formation on irradiation with an intense femtosecond laser pulse. *Chem. Phys. Lett.*, 342(5-6):563 – 570, 2001.

[162] C. Figueira de Morisson Faria and X. Liu. Electron-electron correlation in strong laser fields. *Journal of Modern Optics*, 58(13, SI):1076–1131, 2011.

[163] J. Breidbach and L. S. Cederbaum. Universal attosecond response to the removal of an electron. *Phys. Rev. Lett.*, 94:033901, Jan 2005.

[164] Michael Spanner and Serguei Patchkovskii. One-electron ionization of multielectron systems in strong nonresonant laser fields. *Phys. Rev. A*, 80(6):063411, Dec 2009.

[165] H. Akagi et al. Laser tunnel ionization from multiple orbitals in hcl. *Science*, 325(5946):1364–1367, 2009.

[166] T. Koopmans. Über die Zuordnung von Wellenfunktionen und Eigenwerten zu den Einzelnen Elektronen Eines Atoms. *Physica*, 1(1-6):104 – 113, 1934.

[167] V. Blanchet, M.Z. Zgierski, T. Seideman, and A. Stolow. Discerning vibronic molecular dynamics using time-resolved photoelectron spectroscopy. *Nature*, 401(6748):52–54, 1999.

[168] Z.B. Walters and O. Smirnova. Attosecond correlation dynamics during electron tunnelling from molecules. *J. Phys. B*, 43:161002, 2010.

[169] M Spanner. (private communication).

[170] A. F. Lago, James P. Kercher, Andrs Bdi, Blint Sztray, B. Miller, D. Wurzelmann, and Tomas Baer. Dissociative photoionization and thermochemistry of dihalomethane compounds studied by threshold photo-

electron photoion coincidence spectroscopy. *The Journal of Physical Chemistry A*, 109(9):1802–1809, 2005.

[171] Hanneli R. Hudock, Benjamin G. Levine, Alexis L. Thompson, Helmut Satzger, D. Townsend, N. Gador, S. Ullrich, Albert Stolow, and Todd J. Martinez. Ab initio molecular dynamics and time-resolved photoelectron spectroscopy of electronically excited uracil and thymine. *J. Phys. Chem A*, 111(34):8500–8508, 2007.

[172] Michael Spanner and Serguei Patchkovskii. Molecular strong field ionization and highharmonic generation: A selection of computational illustrations. *Chem. Phys.*, (0):–, 2012.

[173] David Cardoza, Brett J. Pearson, and Thomas Weinacht. Dissociative wave packets and dynamic resonances. *J. Chem. Phys.*, 126:084308, 2007.

[174] J.A. Nelder and R. Mead. A simplex method for function minimization. *The computer journal*, 7(4):308, 1965.

Appendix A

Fitting

A.1 Description of the fitting function

In order to quantify the observation that pump-probe ion signals differ between fragments of a molecule, we fitted a model function, $f(t)$, to the experimental data. This approach was used previously [93, 99]. Pump-probe signal for each of the fragments was independently fitted. The model function was a convolution of a Gaussian with a sum of two or three exponentials and constant.

$$f(t) = G(\sigma) \otimes [\theta(t - t_0) \cdot (\sum_{i=1}^{2,3} A_i \cdot e^{-t-(t_0)/\tau_i} + B)] \tag{A.1}$$

where G is a gaussian that corresponds to the width of the cross-correlation between the pump and the probe pulses. It is characterized by its variance σ^2, and given by

$$G(\sigma) = e^{-t^2/2\cdot\sigma^2} \tag{A.2}$$

so that its full width at half maximum $FWHM = 2\sqrt{2\ln 2}\sigma = 2.355 \cdot \sigma$. Here θ is the Heaviside step function (ensuring that the decay only begins after the excited state has been populated), t_0 accounts for different delay where a fragments pump-probe signal is maximum, τ_i are the decay constants and A_i are the amplitudes associated with each of the decays. The constant B can be thought of as an exponential that is too long to be captured in our pump probe scans. This can be due to population trapped in a long-living state, or due to changes in fragmentation patterns between the initial ground state sample and the final hot ground state one.

The fitting function was later modified to:

$$f(t) = A_0 \cdot G(\sigma) \otimes [\theta(t - t_0) \cdot (\sum_{i=1}^{3} A_i \cdot e^{-(t-t_0)/\tau_i} + 1 - A_1 - A_2 - A_3)]. \quad (A.3)$$

Here the A_i constants were rearranged an attempt to decouple the amplitudes from the time constants.

The data was fitted to this function using the Nelder-Mead algorithm [174] for multivariate unconstrained nonlinear optimization implemented in MATLAB.

The code used to perform the fitting is given below.

A.2 Main body of the fitting code

The fitting code `fit_gauss_biexp_conv_new_CHD`, written in MATLAB 7.1.

```
%fitting routine for a double exponential convolved with a Gaussian

close all
clear all

molecule_switch = 5;
date_switch = 55;
set_mass_peak_bins6
tz=0;

peaks = [8 9 10 13 14 18 19 20 22:26 28 29 31];%

tz=200;
x=load('xaxis.txt')'-tz;
x1 = aux_x_axis(x); % extended symmetric x axis

%initial guess, make a matrix if it differs
```

```
%from fragment to fragment

start_point = [0.77   35.2   0.11   213.07 ...
    mean(y2fit(end-10:end))  248  64.8];

for ii = 1:length(peaks)

    %load data
    fname = char([peaknamematrix{peaks(ii)} ...
        '_boxcar_lineout_smooth_3.txt'])
    y=load(fname)';
    y=y(end,:);
    y=y/max(y);

    %restrict fitting interval, if necessary
    fit_start_pt = 1;
    fit_end_pt = length(x)-1;
    x2fit = x(fit_start_pt:fit_end_pt);
    y2fit = y(fit_start_pt:fit_end_pt);
    x2fit = flipud(x2fit);

    %linear transform so that lhs ranges between 0 and 1
    k = 1/(max(y2fit)-mean(y2fit(1:15)));
    n = - mean(y2fit(1:15)) / (max(y2fit)-mean(y2fit(1:15)));
    y2fit = y2fit * k + n;

    %define the gaussian cross-correlation
    g1 = exp(-x2fit.^2/(2*start_point(7)^2));
    g1=g1/sum(g1);

    tic
    fit = fitcurvedemo_gauss_biexp_conv_with_sigma2(x2fit, ...
        y2fit,start_point);
    toc
```

```
parameters(:,ii) = fit;

%redefine Gaussian, since FWHM was a fitting parameter
g1 = exp(-x2fit.^2/(2*fit(7)^2));
g1=g1/sum(g1);

%fitted function
fitted= fit(1)*convn(g1,stepexp(x1,fit(6),1,fit(2))...
    /max(convn(g1,stepexp(x1,fit(6),1,fit(2)))),'same')+ ...
    fit(3)*convn(g1,stepexp(x1,fit(6),1,fit(4))...
    /max(convn(g1,stepexp(x1,fit(6),1,fit(4)))),'same') + ...
    fit(5)*convn(g1,stepexp(x1,fit(6),1,inf)...
    /max(convn(g1,stepexp(x1,fit(6),1,inf))),'same');

%individual components
stepexp1 = fit(1)*convn(g1,stepexp(x1,fit(6),1,fit(2))...
    /max(convn(g1,stepexp(x1,fit(6),1,fit(2)))),'same');
stepexp2 = fit(3)*convn(g1,stepexp(x1,fit(6),1,fit(4))...
    /max(convn(g1,stepexp(x1,fit(6),1,fit(4)))),'same');
stepexp3 = fit(5)*convn(g1,stepexp(x1,fit(6),1,inf)...
    /max(convn(g1,stepexp(x1,fit(6),1,inf))),'same');

% evaluate goodness of fit
tau = [parameters(2,ii) parameters(4,ii)];
tau = sort(tau);
goodness =sum((y2fit-fitted).^2) /length(y2fit);

%plot the final fit
hfig = figure;
hold on
plot(x2fit,fitted,'r','linewidth',2);
plot(x2fit,y2fit,'k','linewidth',1);
plot(x2fit,stepexp1,'g','linewidth',2);
plot(x2fit,stepexp2,'g--','linewidth',2);
```

```
    plot(x2fit,stepexp3,’g-.’,’linewidth’,2);
    axis tight;

    v = axis(gca);
    text((v(1)+2*v(2))/3,(v(3)+3*v(4))/4,...
        strvcat([num2str(tau(2),’%.0f’) ’fs’], ...
        [num2str(tau(1),’%.0f’) ’fs’]),’color’,’r’);
    title(strcat(’fit for ’, peaknamematrix(peaks(ii)),...
        ’, \chi=’, num2str(goodness,’%.5f’),...
        ’, \sigma=’, num2str(fit(7),’%.1f’)))

    %save files
    fname = char(strcat(’biexp conv fit’,...
        peaknamematrix(peaks(ii)),’initial2’));
    print(’-dpng’,strcat(fname,’.png’));
    hgsave(hfig,strcat(fname,’.fig’));
    save(strcat(fname,’.txt’),’fit’,’-ascii’);

end
```

A.3 Subroutines of the fitting code

Subroutine that performs fitting using Matlab’s built in `FMINSEARCH` function.

```
function [estimates, model] = fitcurvedemo(xdata,ydata,...
    start_param_vector,sigma)

start_point = start_param_vector;
model = @expfun;
options=optimset(’MaxFunEvals’,50000,’MaxIter’,50000,...
    ’FunValCheck’,’on’,’TolFun’,1E-7,’TolX’,1E-7);
[estimates,fval,exitflag] = fminsearch(model, start_point,options);
disp(’exiflag =’)
exitflag
```

```
    function [sse, FittedCurve] = expfun(params)
        A1 = params(1);
        tau1 = params(2);
        A2 = params(3);
        tau2 = params(4);
        B = params(5);
        offset = params(6);
        sigma = params(7);

        g=exp(-xdata.^2/(2*sigma^2));
        g=g/sum(g);
        x1 = aux_x_axis(xdata); % extended symmetric x axis
        step = 0.5*(sign(x1)+1);

        c1 = convn(g,stepexp(x1,params(6),1,params(2)),'same');
        c2 = convn(g,stepexp(x1,params(6),1,params(4)),'same');
        c3 = convn(g,stepexp(x1,params(6),1,inf),'same');
        FittedCurve= params(1) * c1/max(c1) + ...
            params(3) * c2/max(c2)+ ...
            params(5) * c3/max(c3);

        ErrorVector = FittedCurve - ydata;
        sse = sum(ErrorVector .^ 2);
    end
end
```

Subroutine `STEPEXP`.

```
%calc step.*exp(-x/tau)
%does not evaluate exp where step = 0
%by marija feb 2010

function[se] = aux(xaxis,offset,A,tau)
```

```
xl = length(xaxis);

for ii=1:xl
    if xaxis(ii)<-offset se(ii) = 0;
    else se(ii) = A*exp(-(xaxis(ii)+offset)/tau);
    end
end
```

Subroutine `AUX_X_AXIS`.

```
%create auxiliary x axis for convolutions
%if old x axis is (-a,b)
%new x axis has to be
%(-max(abs(a),abs(b))-extra,-max(abs(a),abs(b))+extra)
%the new axis has to symmetric and extend outside of the old one
% assumes x values are equidistant from each other
%by marija jan 2010

function[xx] = aux(xaxis)

xl = length(xaxis);
%extends the x axis on the positive side by 20%
xx=[xaxis  xaxis(end)+(1:round(0.2*xl))*max(diff(xaxis))];

xnew = min(xx);
while xnew > -max(xx)
    xnew = min(xx) - max(diff(xaxis));
    xx = [xnew xx];
end
```